Impacts of Energetic Electron Precipitation on the Middle Atmosphere

by

Ethan D. Peck

B.S., Cornell University, 2009

M.S., University of Colorado Boulder, 2011

A thesis submitted to the Faculty of the Graduate School of the

University of Colorado in partial fulfillment

Of the requirement for the degree of

Doctor of Philosophy

Department of Atmospheric and Oceanic Sciences

2014

This thesis entitled:
Impacts of Energetic Electron Precipitation on the Middle Atmosphere
written by Ethan D. Peck
has been approved for the Department of Atmospheric and Oceanic Sciences

_____

Cora E. Randall

_____

V. Lynn Harvey

Date_____

The final copy of this thesis has been examined by the signatories, and we
Find that both the content and the form meet acceptable presentation standards
Of scholarly work in the above mentioned discipline.

Peck, Ethan D. (Ph.D., Atmospheric and Oceanic Sciences)
Impacts of Energetic Electron Precipitation on the Middle Atmosphere
Thesis directed by Prof. Cora E. Randall

Abstract: Energetic particle precipitation (EPP) can have profound impacts on the middle atmosphere. NO_x produced by EPP in the thermosphere and mesosphere can descend into the stratosphere during polar night; after being sequestered by the polar vortex until spring, NO_x can destroy stratospheric O_3 (>25 km) in a catalytic cycle. Changes to O_3 can change local temperatures and in turn zonal wind through thermal wind balance.

This work seeks to understand the impacts of medium energy electrons (MEE) (25 keV – 2 MeV), a subset of EPP, on the middle atmosphere. Data from the Medium Energy Proton/Electron Detector (MEPED) is assimilated into the Whole Atmosphere Community Climate Model (WACCM). This is accomplished in three steps: (1) examine the response of WACCM to solar cycle; (2) improve and prepare MEPED data for use in WACCM; and (3) simulate MEE precipitation in WACCM.

WACCM is able to simulate solar cycle impacts in general agreement with observations and reanalysis. Auroral EPP (<30 keV) produced NO_x is found to destroy >10% more O_3 in solar maximum simulations than solar minimum simulations. Temperature and zonal wind results match reanalysis in the northern hemisphere (NH), but not in the southern hemisphere (SH). Disagreements are likely caused by the Antarctic "cold-pole problem."

This work removes proton contamination from MEPED electron channels and outputs spectral count flux for protons and electrons by using an inversion technique with a combination of best fit spectra. Results are in agreement with the Detection of Electro-Magnetic Emissions Transmitted from Earthquake Regions (DEMETER) Instrument for Detecting Particles (IDP).

MEE spectral flux is converted into precipitating flux and assimilated into specified dynamics WACCM (SD-WACCM). Production by MEE is large (>100 ppbv at 80 km). MEE NO_x production is too high below 80 km, and too low above 80 km. SD-WACCM is also found to have too strong winter polar descent. MEE precipitation is believed to be capable of producing NO_x to match observations, but production at the wrong altitudes and incorrect descent prevent further analysis into impacts on the middle atmosphere.

To my parents for raising me with an inquisitive mind.

To my brothers for sharpening my wits.

To my wife, Anna, for supporting me, even when I whine.

Acknowledgements

Contents

Chapter

Tables

Table

Figures

Figure

Chapter 1

EPP influences on the atmosphere

1.1 Introduction

Climate change research requires a separation of the natural and anthropogenic forcings that drive the Earth's climate system [e.g., *IPCC*, 2013]. A source of natural climate variability is the 11-year solar cycle. Ozone (O_3) is a radiatively active trace gas; thus solar cycle effects on O_3 must first be quantified in order to assess changes in climate. Energetic particle precipitation (EPP) is a source of natural variability controlled by the solar cycle that affects stratospheric O_3 concentrations. Studies have shown substantial changes to stratospheric O_3 as a result of EPP [e.g., *Randall et al.*, 2007], however not all forms of EPP have been thoroughly studied.

This work uses a global climate model to quantify the impacts of the solar cycle and of medium energy electron (MEE) precipitation (a subset of EPP) on the middle atmosphere. The middle atmosphere is defined here as the stratosphere and mesosphere. The stratosphere is a region of generally increasing temperatures with increasing altitude from ~10 − 50 km. The mesosphere is the region above the stratosphere dominated by cooling with altitude from ~50 − 100 km. The model used is the National Center for Atmospheric Research (NCAR) Whole Atmosphere Community Climate Model version 4 (WACCM4). Attempts at quantifying the amount of MEE precipitation have been conducted [*Verronen et al.*, 2011; *Andersson et al.*, 2012; 2014], however no studies of the impacts from MEE precipitation have been conducted.

This work seeks to answer the following question:

What are the impacts of MEE precipitation on the stratosphere and mesosphere?

In order to answer this question, realistic distributions of MEE using observations are assimilated into WACCM4. MEE data comes from the Space Environment Monitor version 2 (SEM-2) Medium Energy Proton/Electron Detector (MEPED) on board the Polar Operational Environmental Satellites (POES). This work will answer the question above by accomplishing the following objectives:

1. **Understand how solar cycle variation, including energetic electron precipitation (EEP) and solar spectral irradiance (SSI), impact the atmosphere as resolved in WACCM4 and how those impacts compare to previous studies.**

2. **Improve and prepare the POES SEM-2 MEPED data for use in WACCM4.**

3. **Incorporate MEE into WACCM4 and quantify the modeled impacts on the stratosphere and mesosphere.**

This thesis is divided into 5 chapters as follows. The remainder of Chapter 1 provides the background information necessary to understand known impacts of EPP on the stratosphere and mesosphere. Chapter 2 describes how auroral EPP and the solar cycle are currently represented in WACCM versions 3 and 4. Chapter 3 explains the method by which the SEM-2 MEPED MEE data is improved and prepared for use in WACCM4. This includes a thorough discussion of the methods used to first remove proton contamination from the electron data. Chapter 4 explains how MEE is incorporated into the model and explores the impacts of MEE precipitation on NO_x and O_3 distributions in the middle atmosphere. Chapter 5 summarizes the conclusions and outlines future work.

1.2 General Ozone Chemistry

O_3 absorbs ultraviolet (UV) radiation [*Brasseur and Solomon*, 2005] and produces molecular and atomic oxygen via photodissociation:

$$O_3 + h\nu \rightarrow O_2 + O \ [200 \ nm < \lambda < 350 \ nm] \tag{1.1}$$
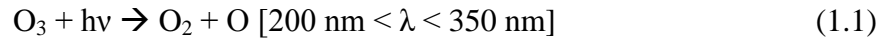
Following the reaction given in (1.1), atomic and molecular oxygen recombine in exothermal reactions, heating the surrounding atmosphere.

$$O + O + M \rightarrow O_2 + M \tag{1.2}$$

$$O + O_2 + M \rightarrow O_3 + M \tag{1.3}$$

Since atmospheric pressure and density are relatively high in the stratosphere (compared to the thermosphere), Reaction 1.1 is nearly instantaneously followed by Reactions 1.2 or 1.3. Therefore, the absorption of UV radiation by O_3 and heating from the exothermal reaction that follows occur at the same location. The total heating of the atmosphere by O_3 absorption of UV photons is often parameterized [*Schoeberl and Strobel*, 1978]. Figure 1.1 shows chemical heating rates in the stratosphere from *Mertens et al.* [1999]. Heating in the stratosphere is dominated by O_3 absorption of UV radiation.

O_3 (along with CO_2 and H_2O) also emits infrared radiation that is ultimately lost to space. This radiative cooling is an important factor in stratospheric thermodynamics. However, not all infrared radiation emitted from O_3 is lost to space; it is also absorbed in the lower stratosphere and results in a local heating [*Mlynczak et al.* 1999].

Since O_3 can impact atmospheric temperatures, it can also impact winds through thermal wind balance [e.g., *Holton*, 2004]. Therefore, changes to O_3 affect middle atmosphere dynamics [e.g., *Marsh et al.*, 2007].
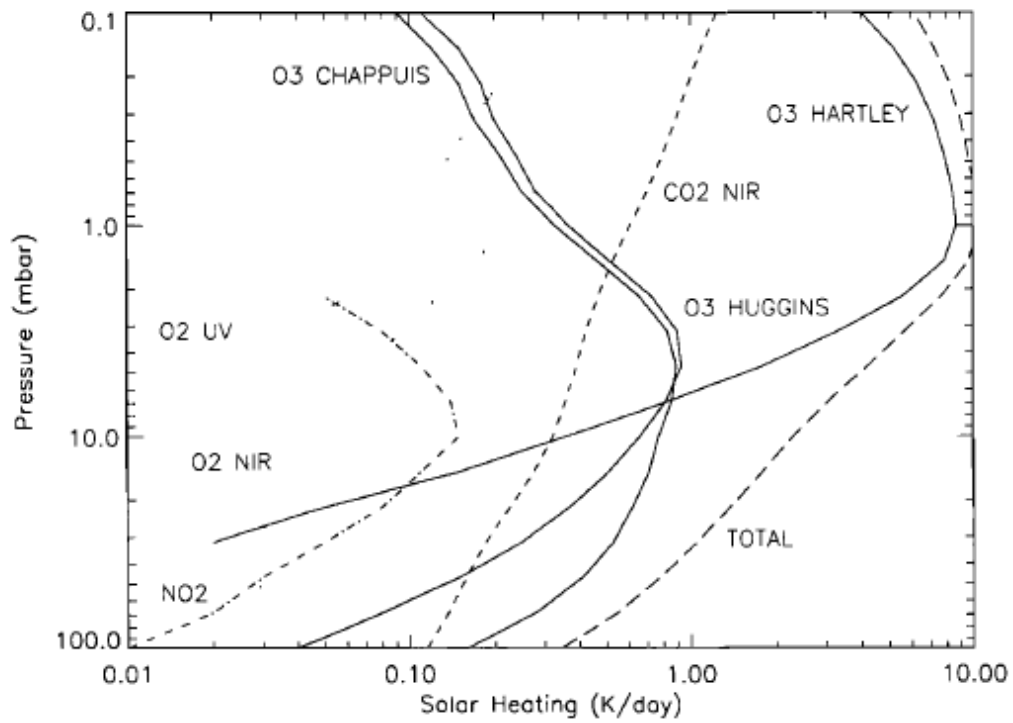
Figure 1.1: Equinox solar heating rates calculated from the zonal mean Nimbus-7 Limb Infrared Monitor of the Stratosphere (LIMS) observed profiles of temperature, O_3, and NO_2 at 44N using a radiative transfer algorithm [*Martens et al.*, 1999].

1.3 EPP Chemistry

EPP impacts middle atmosphere (stratosphere and mesosphere) O_3 via the production of NO_x (NO_x = N + NO + NO_2) and HO_x (HO_x = H + OH + HO_2). The following discussion outlines the chemistry involved in the production of NO_x and HO_x by EPP, hereafter referred to as EPP-NO_x and EPP-HO_x, respectively, and their effects on O_3.

EPP-NO_x production reactions below were presented by *Rusch et al.* [1981]. Upon entering the atmosphere secondary electrons from EPP, e*, participate in the following reactions:

$$e^* + N_2 \rightarrow N_2^+ + 2e \tag{1.1}$$

$$e^* + N_2 \rightarrow N + N^+ + 2e \tag{1.2}$$

$$e^* + N_2 \rightarrow N + N + e \tag{1.3}$$

$$e^* + O_2 \rightarrow O_2^+ + 2e \tag{1.4}$$

$$e^* + O_2 \rightarrow O + O^+ + 2e \tag{1.5}$$

Reactions 1.1-1.5 result in ion production and are followed by:

$$N_2^+ + O \rightarrow NO^+ + N \tag{1.6}$$

$$N_2^+ + e \rightarrow N + N \tag{1.7}$$

$$O^+ + N_2 \rightarrow NO^+ + N \tag{1.8}$$

$$N^+ + O_2 \rightarrow O^+ + NO \rightarrow NO^+ + O \rightarrow O_2^+ + N \tag{1.9}$$
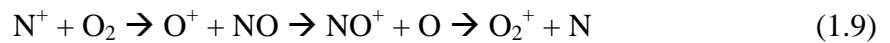
by which the interchange and recombination reactions result in NO_x production. Production of NO^+ then leads to:

$$NO^+ + e \rightarrow N + O \tag{1.10}$$

where the resulting atomic nitrogen is in either the ground (^{4}S) or excited (^{2}D) state. Atomic nitrogen can then react as follows to produce NO:

$$N(^4S) + O_2 \rightarrow NO + O \tag{1.11}$$

$$N(^2D) + O_2 \rightarrow NO + O \tag{1.12}$$

Reaction 1.12 is much faster than reaction 1.11 at temperatures found in the mesosphere and stratosphere. The same atomic nitrogen from reaction 1.10 also reacts as follows to destroy NO:

$$N(^4S) + NO \rightarrow N_2 + O \tag{1.13}$$

$$N(^2D) + NO \rightarrow N_2 + O \tag{1.14}$$
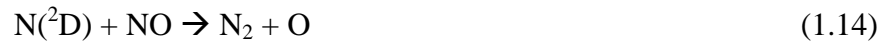
In laboratory experiments, the normal path for $N(^2D)$ is reaction 1.12 while $N(^4S)$ follows reaction 1.13. As such, a branching ratio of atomic nitrogen from reaction 1.10 for ground versus excited state must not surpass 50%, else NO loss will surpass NO production. *Garcia* [1992] found the branching ratio to be ~20% for ground state atomic nitrogen production, thus supporting production of NO by reaction 1.12 over loss of NO by reaction 1.13.

The process to create HO_x after the production of ions from reactions 1.1 through 1.5 is as follows [*Solomon et al.*, 1981]:

$$O_2^+ + O_2 + M \rightarrow O_4^+ + M \tag{1.15}$$

$$O_4^+ + H_2O \rightarrow O_2^+ \cdot H_2O + O_2 \tag{1.16}$$

$$O_2^+ \cdot H_2O + H_2O \rightarrow H_3O^+ \cdot OH + O_2 \tag{1.17}$$
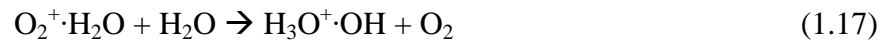
Three possible paths follow and all result in the same net product. Path one starts from reaction 1.17 as follows:

$$H_3O^+ \cdot OH + e^- \rightarrow H + OH + H_2O \tag{1.18}$$

Path two also begins from reaction 1.17 followed by:

$$H_3O^+ \cdot OH + H_2O \rightarrow H_3O^+ \cdot H_2O + OH \tag{1.19}$$

$$H_3O^+ \cdot H_2O + nH_2O \rightarrow H_3O^+(H_2O)_{n+1} \tag{1.20}$$

$$H_3O^+(H_2O)_{n+1} + e^- \rightarrow H + (n+2)H_2O \tag{1.21}$$
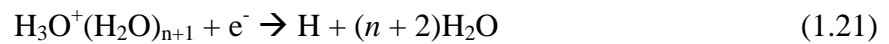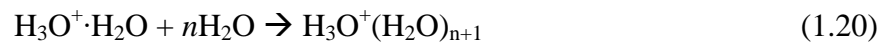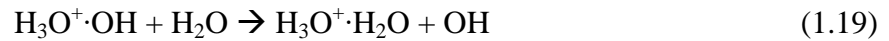
and path three continues from reaction 1.16 with:

$$O_2^+ \cdot H_2O + H_2O \rightarrow H^+ \cdot H_2O + OH + O_2 \quad (1.22)$$

$$H^+ \cdot H_2O + n(H_2O) \rightarrow H_3O^+(H_2O)_n \quad (1.23)$$

$$H_3O^+(H_2O)_n + e^- \rightarrow H + (n+1)H_2O \quad (1.24)$$
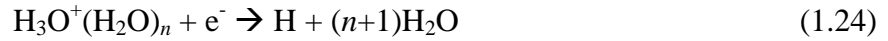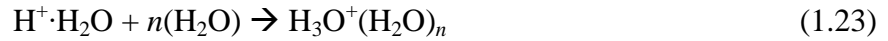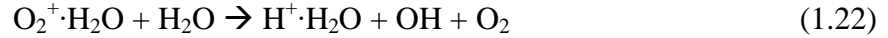
The net effect from all three paths is:

$$H_2O \rightarrow H + OH \quad (1.25)$$

Production of EPP-HO_x via the above reactions is important below 80 km, since HO_x produced above 80 km rapidly recombines [*Solomon et al.*, 1981; 1983]. HO_x has a short (~hours) photochemical lifetime between 50 and 85 km. Therefore, EPP-HO_x quickly dissipates following EPP-induced production [*Solomon et al.*, 1983].

Both EPP-HO_x and EPP-NO_x participate in catalytic O_3 destruction. The EPP-HO_x cycle is primarily effects the mesosphere and takes the following forms [*Jackman et al.,* 2008]:

$$OH + O_3 \rightarrow HO_2 + O_2 \quad (1.26)$$

$$HO_2 + O \rightarrow OH + O_2 \quad (1.27)$$

$$\overline{}$$

$$O + O_3 \rightarrow 2O_2$$

and

$$H + O_3 \rightarrow OH + O_2 \quad (1.28)$$

$$OH + O \rightarrow H + O_2 \quad (1.29)$$

$$\overline{}$$

$$O + O_3 \rightarrow 2O_2$$
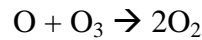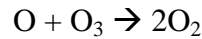
This catalytic cycle between EPP-HO_x and O_3 continues until the EPP source producing OH ends and HO_x is photochemically destroyed.

Chapman [1930] put forth the theory that stratospheric O_3 is photochemically destroyed via the following reactions:

$$O_3 + h\nu \rightarrow O + O_2 \tag{1.30}$$

$$O + O_3 \rightarrow 2O_2 \tag{1.31}$$

———————————

$$2O_3 \rightarrow 3O_2$$
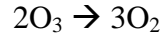
However, this mechanism for O_3 loss is not supported by observed O_3 distributions [e.g., *Crutzen*, 1969; *Hunt*, 1966]. *Crutzen* [1970] proposed the following additional NO_x-driven catalytic cycle:

$$NO + O_3 \rightarrow NO_2 + O_2 \tag{1.32}$$

$$NO_2 + O \rightarrow NO + O_2 \tag{1.33}$$

———————————

$$O_3 + O \rightarrow 2O_2$$
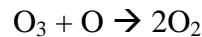
This photochemically-driven NO_x catalytic cycle is now accepted to be the primary O_3 loss cycle for altitudes between ~25 and 40 km [e.g., *Crutzen*, 1979; *Garcia and Solomon*, 1994; *Johnston*, 1972; *McElroy et al.*, 1974; *Nicolet*, 1972; *Watson*, 1986; *Wofsy and McElroy*, 1974]. Sunlight is necessary for reaction 1.33 as a source of atomic oxygen by reaction 1.30.

While EPP-NO_x accounts for up to 40% of polar O_3 loss in the upper stratosphere [*Randall et al.*, 2005], another source of stratospheric NO_x is tropospheric N_2O that is transported into the stratosphere and reacts as follows to create NO [*Bates and Hays*, 1967; *Crutzen*, 1974; *McElroy and McConnell*, 1971; *McElroy et al.*, 1976; *Nicolet*, 1971]:

$$N_2O + O(^1D) \rightarrow 2NO \tag{1.34}$$

Jackman [1980] compared all known NO sources and found N_2O to be the largest contributor to the stratospheric NO_x reservoir. Current maximum estimates of EPP-NO_x contribution to total hemispheric NO_x in the stratosphere is ~10% [*Funke et al.*, 2005; *Holt et al.*, 2012; *Randall et al.*, 2007].

1.4 EPP impact mechanisms

EPP-HO_x and EPP-NO_x impact O_3 through two accepted mechanisms: the EPP direct effect (EPP-DE) and EPP indirect effect (EPP-IE) [*Randall et al.*2006; 2007]. These mechanisms are described below.

1.4.1 EPP-DE

The EPP-DE occurs when EPP creates ions (Reactions 1.1 through 1.5) that result in HO_x or NO_x. The EPP-HO_x and EPP-NO_x can then enter a catalytic cycle at the same location as they were produced. Higher energy particles penetrate and produce ion pairs deeper in the atmosphere [*Roble and Ridley*, 1987, and references therein]. Thus, stratospheric O_3 loss due to the EPP-DE is attributed to high energy galactic cosmic rays (GCRs), solar proton events (SPEs), relativistic electron precipitation (REP), and MEE precipitation. Particles that do not penetrate deep into the atmosphere, such as auroral electrons, follow the EPP-DE in that they produce EPP-NO_x in the thermosphere and upper mesosphere; however this does not immediately result in O_3 destruction. Since EPP-HO_x is short lived, O_3 loss by EPP-HO_x is due to the EPP-DE.

1.4.2 EPP-IE

The EPP-IE occurs when EPP-NO_x is created in the thermosphere or mesosphere and is then transported to the stratosphere where catalytic O_3 destruction can occur. Auroral electrons and MEEs are associated with the EPP-IE since they create NO_x in the thermosphere and mesosphere. Mechanisms responsible for descent of thermospheric NO_x into the mesosphere are

a combination of eddy diffusion, molecular diffusion, and the global mean circulation. Transport timescales of thermospheric EPP-NO_x to 95 km can range from hours to days [*Banks and Kockarts*, 1973; *Siskind et al.*, 1989; *Cleary*, 1985; *Siskind*, 1994; *Yonker and Bailey*, 2008; *Richards*, 2004]. Once NO_x reaches (or is produced in) the mesosphere, the winter upper branch of the residual circulation (described in Section 1.5.1) transports air into the polar vortex in the lower mesosphere and stratosphere on timescales of weeks and months.

NO_x is photolyzed in the presence of sunlight within days in the mesosphere and weeks to months in the stratosphere [*Frederick et al.*, 1983; *Minschwaner and Siskind*, 1993; *Siskind et al.*, 1997]. Therefore the EPP-IE is only effective in the polar winter when there is little sunlight and the lifetime of NO_x is long. EPP-NO_x is sequestered at high latitudes by the polar vortex until spring when sunlight returns to the pole and the catalytic cycle between NO_x and O_3 begins. This descent in the winter polar mesosphere occurs at a rate of ~1-2 km/day [*Greenblatt et al.*, 2002, and references therein]. The dynamical property most relevant to the EPP-IE is the rate of descent in polar winter. Factors that influence descent rates include vertical diffusion, the strength of the stratospheric polar vortex, the strength of the residual circulation, and the propagation and breaking of planetary waves and gravity waves. Secondary impacts from the quasi-biennial oscillation (QBO), tides, and the El Niño Southern Oscillation (ENSO) must also be considered. The situation is further complicated during analysis by nonlinear wave-mean flow interactions, unresolved waves in models, poorly understood coupling and feedback mechanisms, limited observations, and coarse model resolution.

1.5 Middle Atmosphere Dynamics

EPP influences on the middle atmosphere are strongly modulated by atmospheric dynamics. Of greatest importance are the residual circulation and the winter polar vortex.

1.5.1 Residual Circulation

Much of middle atmosphere dynamics are driven by radiative equilibrium temperatures established via a balance between the absorption of UV radiation by O_3 and the infrared cooling by CO_2. If this were the only controlling factor of dynamics, winds would be entirely zonal with no meridional component [*Shine*, 1987]. Figure 1.2 shows calculated zonal mean temperatures for June in the Southern Hemisphere (SH) using only radiative equilibrium to drive dynamics (top panel). In this idealized situation, locations that receive no sunlight (poleward of 65°S) become extremely cold. The bottom panel shows results from a combined observational temperature product [*Barnet and Corney*, 1985]. Comparison of the two panels reveals that the middle atmosphere is not controlled by radiative equilibrium alone. The processes that cause temperatures to deviate from radiative equilibrium are vertical motions induced by breaking gravity and planetary waves. The breaking waves deposit momentum in the middle atmosphere and this added forcing drives a pole-to-pole circulation known as the meridional residual circulation that results in descent over the winter pole and adiabatic heating that significantly warms the winter polar stratosphere and mesosphere [*Andrews et al.*, 1987].

Figure 1.3 is a schematic of streamlines depicting the residual circulation from *Dunkerton* [1978]. The circulation can be split broadly into two branches. The lower branch (known as the Brewer-Dobson circulation) is marked by ascending air at the equatorial lower stratosphere and poleward flow throughout the lower stratosphere. The upper branch circulation is characterized by rising motion in the summer polar regions, meridional flow toward the winter hemisphere, and descent over the winter pole. At high latitudes, vertical components of the wave-driven residual circulation induce an adiabatic cooling (warming) in the summer (winter) hemisphere.
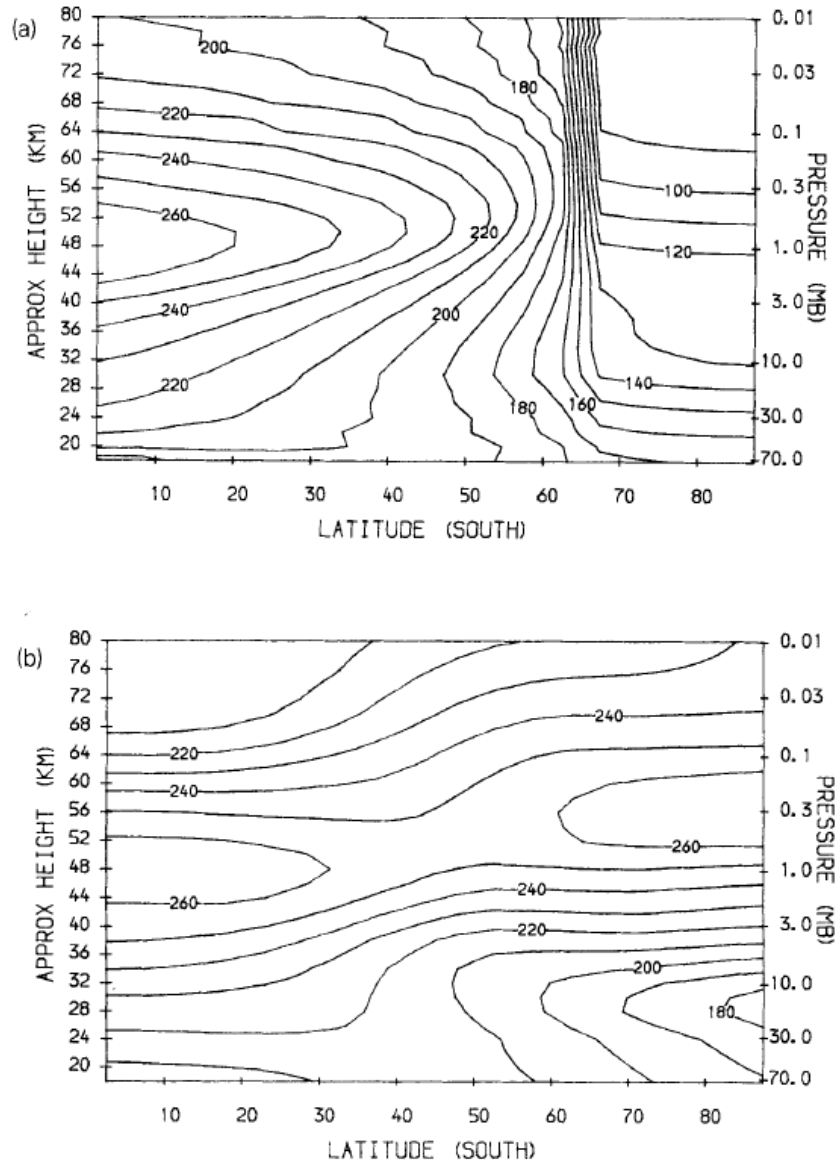
Figure 1.2: Monthly average zonal mean temperature (K) for the Southern Hemisphere in June (a) calculated using radiative equilibrium and (b) observed temperatures from *Barnett and Corney* [1985]. Figure reproduced from *Shine et al.* [1987].
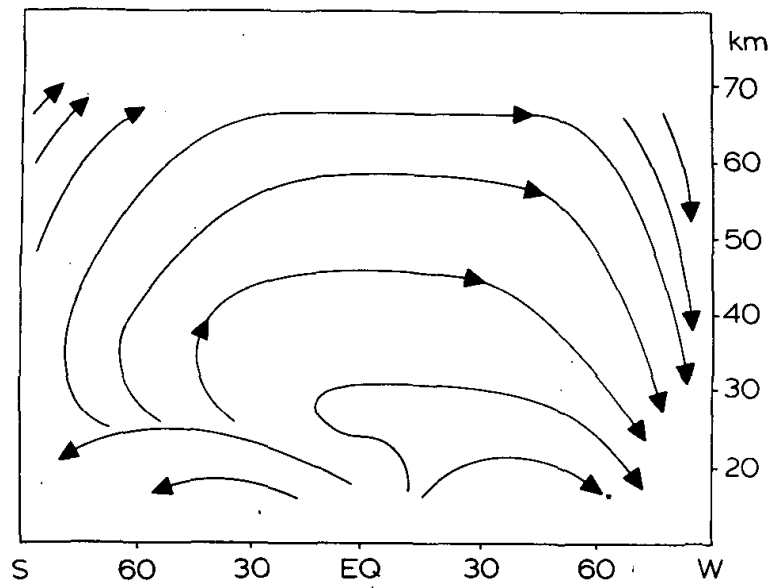
Figure 1.3: Streamline schematic of Lagrangian-mean velocity derived diabatic circulation [*Dunkerton*, 1978].

The residual circulation plays a critical role in the downward transport of NO_x from the mesosphere to the stratosphere in the EPP-IE [e.g., *Hauchecorne et. al.*, 2007]. The description of the EPP-IE thus far has been mainly applicable to the SH. However, perturbations to the ideal descent of EPP-NO_x into the polar vortex and sequestration of air until spring occur regularly in the Northern Hemisphere (NH).

1.5.2 The Polar Vortex and Sudden Stratospheric Warmings

The polar vortex is a circumpolar cyclone that forms in the winter stratosphere due to decreased solar insolation at high latitudes. Thermal wind balance creates strong westerly winds, and these winds demark the boundary of the vortex. The polar winter vortex forms in September in the NH and persists until March or April [*Harvey et al.*, 2002]. In the SH, the vortex forms in March and decays from the top down beginning in October. The polar vortices generally extend from the tropopause to well into the mesosphere and the descending branch of the residual circulation is largely confined to inside the vortex region. The vortex creates a barrier that inhibits mixing across the vortex edge [*Holton*, 2004]. Upon reaching the stratosphere, NO_x is sequestered inside the polar vortex if the vortex is strong and stable.

A sudden stratospheric warming (SSW) [*Scherhag*, 1952] is a disruption to the polar vortex that occurs when large-amplitude planetary waves break and warm the stratosphere, weaken the winds, and promote large-scale horizontal mixing. The breaking planetary waves force the vortex to be either displaced from the pole or is split into two cyclonic lobes through wave-mean flow interaction [*Matsuno,* 1971; *Shepherd*, 2000]. SSWs are often divided into two categories: major and minor [e.g., *Charlton and Polvani*, 2007]. The definition of these warming categories is somewhat arbitrary and has changed over time [*Butler et al.*, 2014]. A common definition for a minor warming is a zonal averaged temperature increase at 10 hPa from 60° to

the pole. A major warming occurs when the conditions for a minor warming are met, along with easterly zonal winds reversal at 60°. The creation of a more scientifically relevant definition of a SSW is an area of current debate [e.g., *Butler et al.*, 2014; *McLandress and Shepherd*, 2009].

When planetary waves are large, such as during SSWs, they change filtering of upward propagating gravity waves. During SSWs, less wave breaking occurs in the upper stratosphere and lower mesosphere, leading to a disruption of the residual circulation. This leads to a decrease in mesospheric temperatures associated with radiative cooling [e.g., *Siskind et al.,* 2007]. Following a SSW, increased mesospheric descent occurs due to greater wave breaking and momentum deposition driving the residual circulation in the upper mesosphere. This increased descent can bring more EPP-NO_x down to the stratosphere as the polar vortex reforms. *Holt et al.* [2013] used WACCM to demonstrate that timing of SSWs influence how much EPP-NO_x descends into the polar stratosphere. Figure 1.4 from *Holt et al.* [2013] shows that more EPP-NO_x descends to the stratosphere following earlier SSWs. The early SSW allows more time for increased descent to bring down EPP-NO_x from the mesosphere. An early SSW also avoids mixing out stratospheric NO_x since there has not been much time for EPP-NO_x to reach the stratosphere.

Planetary waves that cause a SSW are created from tropospheric meteorology and topography. Therefore, the NH is more prone to SSWs than the SH, with the only observed major SSW in the SH occurred in 2002. A major SSH occurs approximately once every two years in the NH [*Richter et al.*, 2010]. This means that the impact of the EPP-IE is more consistent between years in the SH and more variable in the NH.

Wave filtering by the polar vortex and SSWs is a strong driver of whole atmospheric coupling. Geopotential height changes associated with the Northern Annular Mode (NAM) have
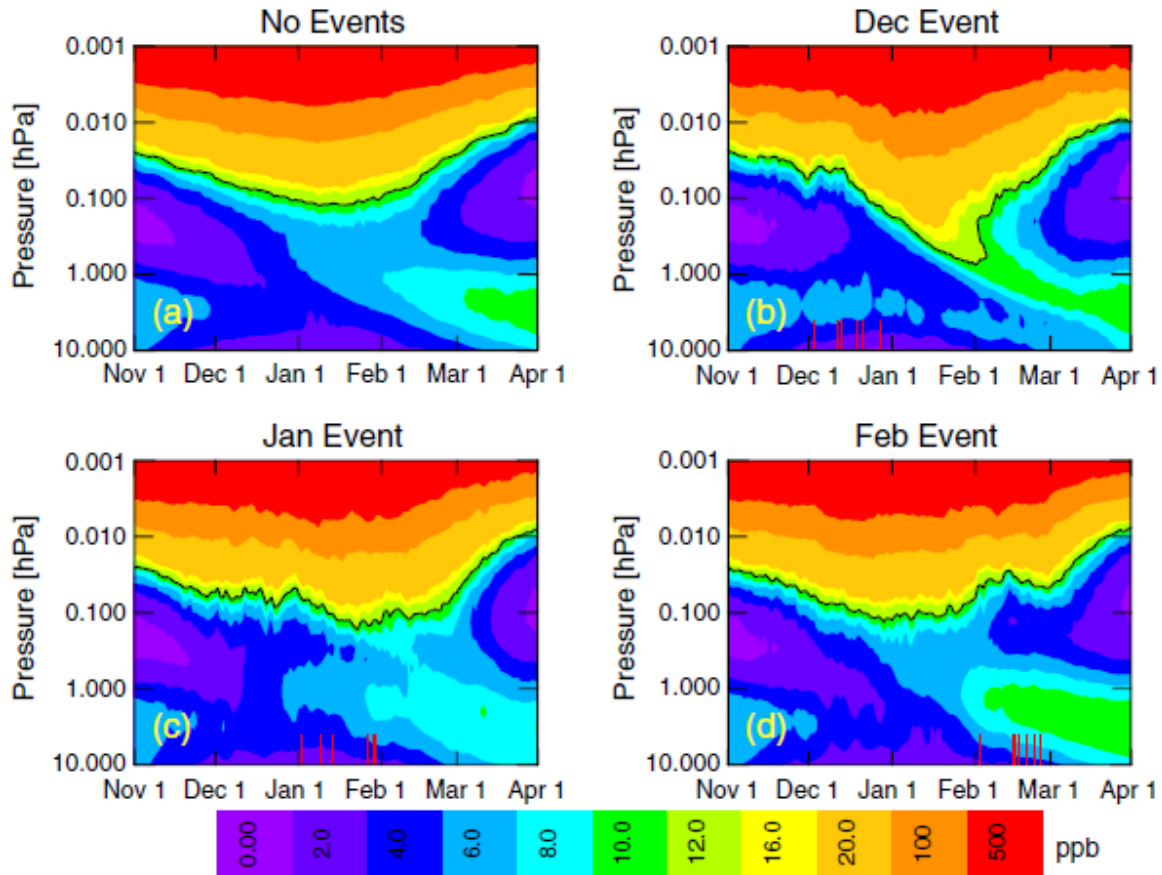
Figure 1.4: WACCM NO$_x$ poleward of 70 degrees North as a function of pressure and time. Plots are daily averages of years with no SSWs (a), December SSWs (b), January SSWs (c), and February SSWs (d). Red lines denote the day of an event in a given year included in the composite [*Holt et al.*, 2013].

been observed to descend from the polar stratosphere after a SSW [e.g., *Baldwin and Dunkerton*, 2001]. The NAM is characterized by geopotential height anomalies of opposite sign between the polar cap and midlatitude regions [*Holton*, 2004]. Changes to the NAM can be associated with synoptic and planetary scale tropospheric shifts, such as an equatorial shifting of the tropospheric polar jet [*Hitchcock and Simpson*, 2014]. Likewise, wave filtering in the stratosphere is linked to inter-hemispheric coupling with the summer polar mesosphere and can increase the occurrence of polar mesospheric clouds [*Becker and Schmitz*, 2003; *Karlsson et al.*, 2007; 2011; *Gumbel and Karlsson*, 2011; *Benze et al.*, 2012].

1.5.3 Elevated Stratopause Events

In the last decade, prolonged SSWs have preceded the reformation of the stratopause at high altitudes near 80 km [*Siskind et al.*, 2007; *Manney et al.*, 2005; 2008; 2009; *France et al.*, 2012]. This phenomenon has also been recreated in model simulations [e.g., *Kvissel et al., 2011*; *de la Torre et al.*, 2012; *Chandran et al.*, 2011; 2013; *Limpasuvan*, 2011; *France and Harvey*, 2014]. As gravity waves reach higher altitudes, they deposit their momentum, causing a strengthening of the residual circulation along with increased descent, which can play a critical role in NO_x transport from the mesosphere to the stratosphere [*Hauchecorne et al., 2007*]. The descent causes adiabatic warming, which causes a stratopause to form at high altitudes (~80 km). This high altitude stratopause descends back to normal altitudes over time as wave breaking and momentum deposition continues to occur below the stratopause height. There is a time delay between the start of an elevated stratopause (ES) event and a SSW, during which time radiative cooling of the mesosphere occurs. The mesosphere continues to cool until the increased residual circulation overtakes radiative cooling and warms the mesosphere. ES events are believed to occur approximately 2-4 times per decade [*de la Torre et al.*, 2012; *Chandran et al.*, 2013].

Formation of an ES is a proxy for a very strong residual circulation, which means enhanced descent of EPP-NO$_x$. Figure 1.5 is taken from *Randall et al.* [2009] and shows observed EPP-NO$_x$ in the NH for each year between 2004 and 2009 based on the Atmospheric Chemistry Experiment Fourier Transform Spectrometer (ACE-FTS) data. Enhanced EPP-NO$_x$ descent is clearly visible in 2004, 2006, and 2009, associated with years with major SSWs that resulted in ES events. The descent that occurred in 2004 is particularly noteworthy as it is the largest NO$_x$ signal from the EPP-IE ever observed [*Randall et al.*, 2005]. ES events were also observed in 2012 and 2013 [Bailey et al., 2014].

1.6 Sources of EPP

This section explains different types of EPP and the atmospheric impact mechanism most associated with them starting from high energies and going to lower energies. Table 1.1 presents a description of several forms of EPP for use as a reference.

1.6.1 Galactic Cosmic Rays

Galactic Cosmic Rays (GCRs) are high energy (1-1000 GeV) protons and alpha particles that enter the Earth's atmosphere from the cosmos [*Gray et al.*, 2010]. GCR occurrence frequency is inversely proportional with the 11-year solar cycle (with a slight phase shift). During solar maximum the sun's interplanetary magnetic field (IMF) diverts GCRs, resulting in a minimum of GCRs entering the solar system [*Lockwood and Fröhlich*, 2007]. Figure 1.6 shows how GCR occurrence frequency and other measurements related to solar variability change with solar cycle. Sunspot counts are an excellent proxy for solar cycle with maximum counts occurring during solar maximum. The magnetic field influences from solar maximum occur during the downward phase of the solar cycle. Thus the maximum influence of the Sun's magnetic field has a slight phase shift from solar maximum. The GCR frequency and the Earth's
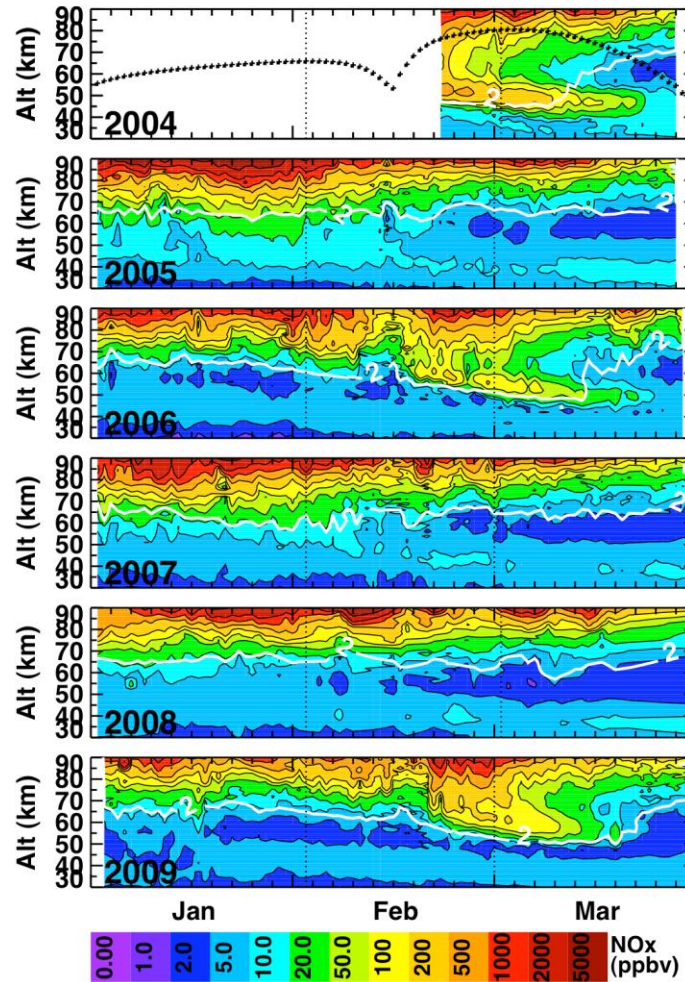
Figure 1.5: Zonal average ACE-FTS NOx (color) in the NH from 1 Jan through 31 Mar of 2004-2009. The white contour denotes CO = 2.0 ppmv; CO increases with increasing altitude. Measurement latitudes (black dots) are shown in the top panel. White regions indicate missing data; vertical black dotted lines denote 1 Feb and 1 Mar. ACE data are unavailable prior to 21 Feb 2004 [*Randall et al.,* 2009].

Particle Population	Primary Particles	Source	Energy Range	Deposition Altitudes	Location	Time Scale	Frequency of Occurrence
Solar Energetic Particles (SEP)	Mostly H+; infrequent e-	Sun	10 – 1000 MeV	20–100 km	Polar cap	~ 1 hr rise time, several days duration	50 – 100 per solar cycle
Auroral — Discrete	e-, H+/H	Magnetotail	1 – 10 keV	>100 km	Auroral oval	Substorm 1-3 hours, multiple times per day	~50 days per year
Auroral — Diffuse	e-, H+/H	Magnetotail	10 – 300 keV	20–150 km; 2nd peak < 50 km (Bremsstrahlung)	Auroral oval	Essentially permanent feature	Continuous
Ring Current	H+, fewer e-; O+ during strong storms	Inner magneto-sphere	1 – 300 keV	>100 km	Subauroral	Maximum during ~1 day storm main phase	~50 – 100 per solar cycle
Radiation Belts	Mostly e-; fewer H+	Inner/outer radi.belts	> 100 keV	30–80 km; 2nd peak < 50 km (Bremsstrahlung)	Subauroral	1 day (flux drop-out events) to 10 day (bursty events)	40 – 50 per solar cycle

Table 1.1: Description of different forms of energetic particles and their regions of impact. Courtesy of Scott Bailey, Janet Kozyra, and Cora Randall.
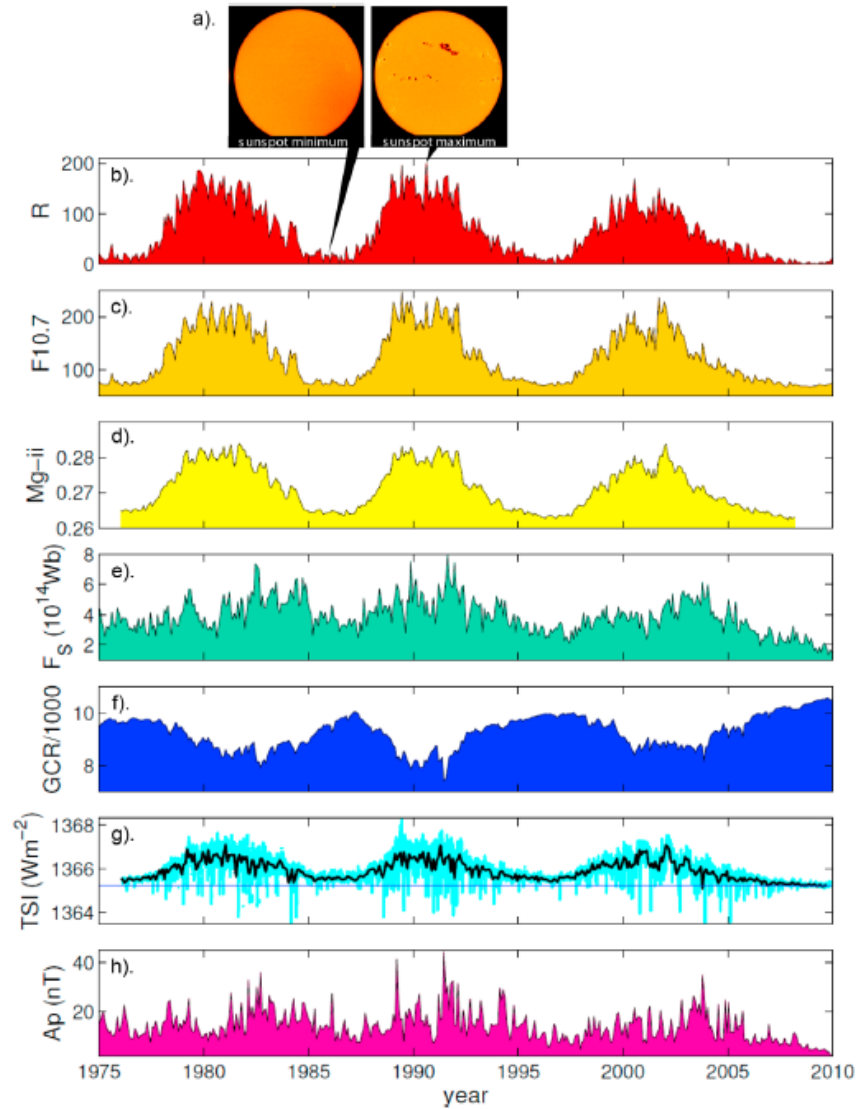
Figure 1.6: (a) Images of the Sun taken at a sunspot minimum (left) and sunspot maximum (right). (b) Number of sunspots represented an index, R, where R = 10N + n, N is the number of sunspot groups, and n is the number of individual sunspots. (c) 10.7 cm solar radio flux (Wm^{-2}Hz^{-1}) measured at Ottawa, Canada. (d) Mg ii line (280 nm) core-to-wing ratio, a measure of the chromospheric MG II ion emission amplitude. (e) Open solar flux calculated. (f) GCR counts per minute measured at McMurdo, Antarctica. (g) Composite of total solar irradiance measurements. (h) Geomagnetic Ap index. All data is monthly averaged except the light blue line in (g) which is the daily total solar irradiance values. Figure from *Grey et al.*, 2010, updated from *Lockwood and Fröhlich*, 2007.

geomagnetic activity both respond to the Sun's IMF. This is why GCR count rate and the geomagnetic index, Ap, are both phase shifted from sunspot count. GCRs ionize atmospheric constituents through the electromagnetic-muon-nucleonic cascade. This cascade process has been modeled using calculated ionization rates and results show that a GCR can result in the ionization of as many as 10^7 molecules [*Usoskin et al.*, 2010]. Results from other modeling studies are in good agreement and indicate that NO production by GCRs occurs between 12 and 13 km at rates ranging from 30 to 50 $cm^{-3}s^{-1}$ [*Jackman*, 1980; *Vitt and Jackman*, 1996; *Ermakov et. al.*, 1997]. GCRs are theorized to have a connection with cloud formation in the troposphere [*Dickinson*, 1975; *Tinsley et al.,* 2000], though the method and magnitude of such an effect is met with some skepticism [*Pierce and Adams*, 2009]. Given the low altitude that GCRs penetrate, their impacts are best described by the EPP-DE.

1.6.2 Solar Proton Events

Solar proton events (SPEs) are sources of high energy (1-200 MeV) protons that originate from the sun following a solar flare or coronal mass ejection [e.g., *Jackman*, 1980]. Since solar proton energies from an SPE are not as high as GCRs, they do not penetrate as deep into the atmosphere, namely in the 40-80 km range [*Jackman et al.*, 2008]. SPE-induced production of HO_x impacts mesospheric O_3 through the EPP-DE mechanism. OH generated from an SPE can significantly increase background HO_x concentrations (~700% at 0.1 hPa). The atmospheric impacts of EPP-HO_x are difficult to measure due to the short HO_x lifetime in the mesosphere [*Jackman et al.,* 2008; *Funke et al.*, 2011]. SPEs also produce NO_x in the mesosphere and stratosphere [*Crutzen*, 1975; *Jackman and Meade*, 1988], which impacts stratospheric O_3 through a combination of the EPP-DE and EPP-IE. The amount of NO that SPEs produce varies depending on the magnitude of the SPE [*Jackman et al.*, 1980; *Vitt and Jackman*, 1996]. Very

large SPEs were modeled and compared to observations from the Halogen Occultation Experiment (HALOE) and the Michelson Interferometer for Passive Atmospheric Sounding (MIPAS) satellite instruments; results showed that NO_x increased by over 50 ppbv, causing a 30% decrease in ozone [*Jackman et al*., 2008].

1.6.3 Radiation belt electrons

Relativistic and medium energy electrons from the Earth's radiation belts span a wide range of energies (~30 kev − 15 MeV) [*Callis et al.*, 1991]. Relativistic electron precipitation (REP) is associated with high-speed solar wind streams [*Callis et al.*,1997; *Blake et al.*, 1997] that energize electrons in the Earth's radiation belts. Given their wide range of energies, radiation belt electrons impact the atmosphere at polar latitudes from the stratosphere through the thermosphere [*Thorne*, 1977; 1980; *Fang et al.*, 2008; 2010; *Roble and Ridley*, 1987; *Baker et al.*, 1987]. Similar to GCRs, radiation belt electron precipitation events create NO in the middle atmosphere that enters a catalytic cycle with O_3. *Callis et al.* [1991] found that radiation belt electron precipitation can result in a 30-35% increase in NO production. *Callis and Lambeth* [1998] used the particle data from the Total Energy Detector (TED) and the Medium Energy Proton and Electron Detector (MEPED), and nighttime NO_2 and N_2O_5 data from the Improved Stratospheric and Mesospheric Sounder (ISAMS) to calculate atmospheric effects. Their results indicated an increase in NO_x and reservoir species (NO_y) at ~0.1 hPa (~60 km) from 6 ppbv to ~40 ppbv over a 24 day period in May of 1992. They attributed the increase to REP in the mesosphere. The NO_y enhancements then descended into the stratosphere during the winter and destroyed O_3 at the beginning of spring. Studies on the impacts of MEEs and REP are limited due to a lack of observations. A new dataset that can be used to quantify radiation belt electron

precipitation is presented in Chapter 3. MEE precipitation will be discussed in sections 1.7 and 1.9 in greater detail.

1.6.4 Auroral electrons

Auroral electrons enter the atmosphere following the plasma sheet (or magnetotail) and enter the atmosphere in the auroral oval over the polar region in each hemisphere [*Eather et al*, 1976]. These electrons have energies less than 30 keV and produce ions in the thermosphere above ~100 km [*Roble and Ridley*, 1987; *Fang et al.* 2008; 2010]. Early two dimensional model studies found that auroral electrons ionize ~3 x 10^{10} cm^{-2} s^{-1} molecules of nitrogen [*Roble and Rees*, 1977; *Crutzen*, 1979]. Auroral EPP-NO$_x$ descends into the mesosphere and stratosphere in the winter hemisphere and catalytically destroys stratospheric O$_3$ in spring as described by the EPP-IE mechanism [*Solomon et al.*, 1982]. The amount of NO that descends into the stratosphere and destroys O$_3$ in the Antarctic winter depends on geomagnetic activity [e.g., *Randall et al.*, 2007]. In the Arctic, the amount of NO that descends into the stratosphere can also depend on the meteorology of the polar vortex [*Randall et al.*, 2005; 2006; 2007; 2009; *Holt et al.*, 2013]. Modeled impacts of the solar cycle using SSI and auroral EEP are described in greater detail in Chapter 2.

The impacts of auroral proton precipitation are not described here. Atmospheric impacts from auroral protons are usually considered small compared to electrons, but can be important at times and have been the topic of many studies [e.g., *Fang et al.*, 2013, and references therein].

1.7 MEE-related magnetospheric particle physics

As mentioned in section 1.6.3, MEEs precipitate into the Earth's atmosphere from the van Allen radiation belts. Particles have three modes of motion in the radiation belts: Cyclotron, Bounce, and Drift.

1.7.1 Particle Cyclotron Motion

As a particle moves in a magnetic field, $\vec{B}$, with velocity, $\vec{v}$, the particle will follow cyclotron motion as a result of the Lorentz force. This force acts perpendicular to $\vec{B}$ and causes the particle to rotate around the field line in a circular motion, imparting a velocity perpendicular to the magnetic field direction, $v_\perp$. Assuming the particle has some parallel velocity, $v_\parallel$, it will follow a helical motion around the center field line as shown in Figure 1.7 from *Tsurutani and Lakhina* [1997]. This figure illustrates particle cyclotron motion. The angle between the particle velocity vector and the magnetic field line vector is defined as the particle pitch angle, α, and is expressed mathematically as:

$$\alpha = \arctan\left(\frac{v_\perp}{v_\parallel}\right) \tag{1.35}$$

1.7.2 Particle Bounce and the Bounce Loss Cone

When magnetic field strength is inhomogeneous parallel to the magnetic field, such as that of the Earth, particle bouncing occurs. As the field lines converge over the pole and the magnetic field strength increases, the Lorenz force increases. Conservation of energy causes the particle to convert more of its velocity into rotation around the field line, $v_\perp$, instead of parallel, $v_\parallel$. Eventually, the particle pitch angle, α, reaches 90°, causing $v_\parallel$ to change sign and the particle to reflect. This form of motion is known as particle "bouncing". In the event the particle bounces on both ends of the magnetic field, such as the case on Earth, the particle is referred to as trapped and will remain trapped until acted upon by another force. A schematic of this type of motion is shown in Figure 1.8 from *Tsurutani and Lakhina* [1997].

The van Allen radiation belts are composed of particles that bounce in the Earth's magnetic field. The smaller a particle's starting pitch angle is at the magnetic equator, the farther the particle will travel before bouncing. On Earth, a particle with a small pitch angle at the

$$\sin \alpha = \frac{V_\perp}{V}$$
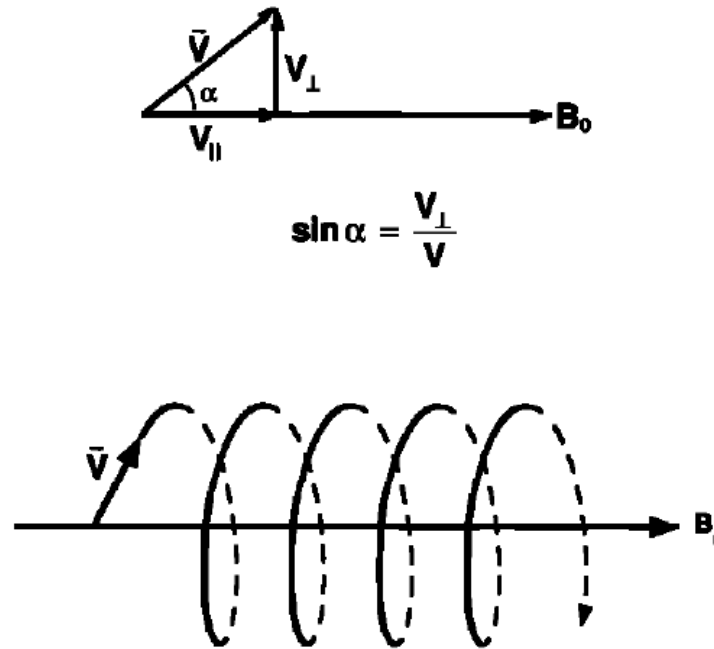
Figure 1.7: Schematic definition of a particle pitch angle (top) and schematic of cyclotron motion (bottom) [*Tsurutani and Lahkina*, 1997].

Magnetic Bottle

$$\mu = \frac{E_\perp}{B} = \text{constant}$$

(first adiabatic invariant)

Earth's Radiation Belts

Magnetic Mirror
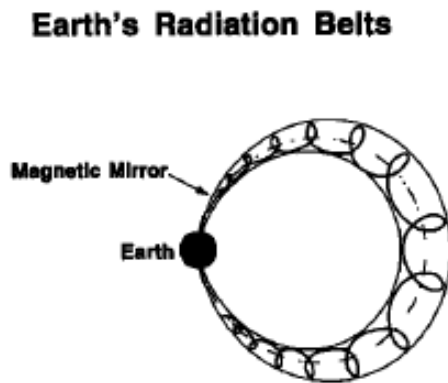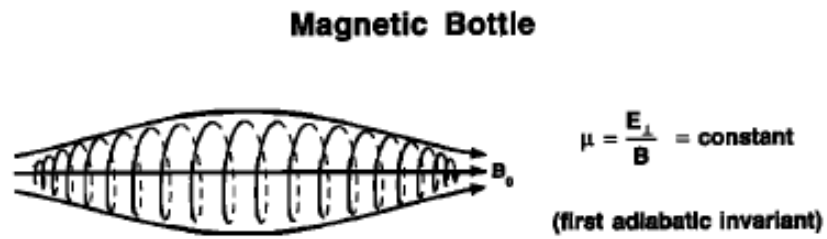
Earth

Figure 1.8: Schematics of particle bouncing (magnetic mirroring) caused by closing magnetic field lines and radiation belts around the Earth [*Tsurutani and Lahkina*, 1997].

magnetic equator has a mirroring point deep in the Earth's atmosphere (<~120 km). In this case, the particle is lost by ionizing atmospheric molecules as described by the chemistry in Section 1.3. Therefore, the particle pitch angles that allow particles to be lost into the atmosphere are known as the bounce loss cone (BLC).

1.7.3 Particle Drift, South Atlantic Anomaly, and the Drift Loss Cone

Particle bouncing requires an inhomogeneous magnetic field strength parallel to the magnetic field direction; however, particle drift occurs when the magnetic field strength is inhomogeneous perpendicular to the magnetic field direction. In this case, the Lorenz force will change depending on where the particle is along its cyclotron motion path. Where the field is strong, the Lorenz force is stronger, meaning $v_\perp$ increases and the helix of the cyclotron motion is tighter. Likewise, the opposite is true in a location of weaker field strength. Thus a particle does not return to its starting location (in relation to the distance from the original magnetic field line), and will "drift" perpendicular to the magnetic field. The direction of the drift depends on the sign of the particle charge; electrons drift eastward while protons drift westward. A schematic of this motion from *Walt* [1994] is shown in Figure 1.9.

In addition to particles being lost from the radiation belts in the BLC, it is also theoretically possible for particles to be lost by drifting into a region of weaker magnetic field. This means that the BLC is longitudinally dependent as well as latitudinally dependent. The location of the weakest magnetic field strength on Earth is located in the South Atlantic near Brazil, known as the South Atlantic Anomaly (SAA). Since this region has the weakest magnetic field strength, particles penetrate deepest into the atmosphere and thus the BLC is largest. Therefore, the drift loss cone (DLC) encompasses all angles at which a particle is lost from the radiation belts as it drifts over the SAA. All particles with pitch angles greater than that needed
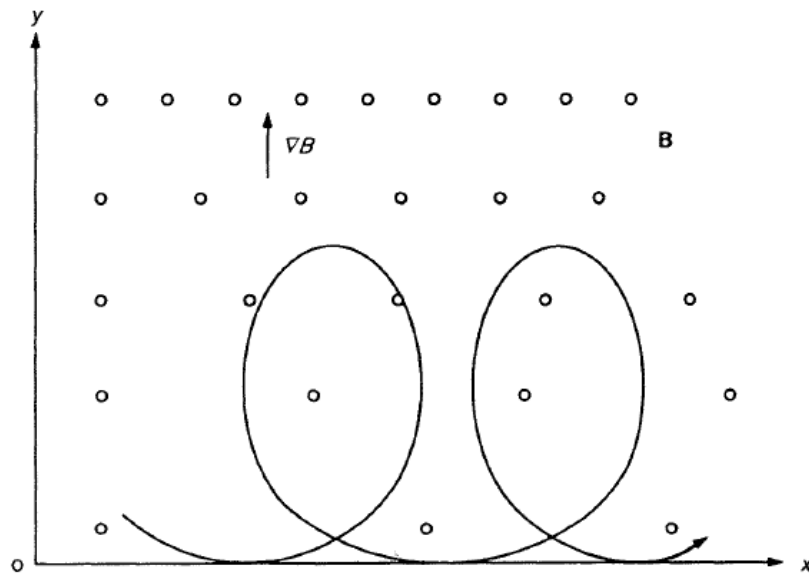
Figure 1.9: Schematic of particle drift [*Walt*, 1994].

to be in the DLC are permanently trapped in the Earth's radiation belts unless acted upon by another force. It should be noted that recent studies [e.g., *Andersson et al.*, 2012; 2014; *Verronen et al.*, 2011] do not find evidence of increased atmospheric ionization in the SAA region, and it is believed that there may not be any radiation belt particle precipitation in that location, contrary to current theory.

1.8 POES SEM-2 MEPED Description

There are six polar orbiting satellites equipped with the SEM-2 MEPED instrument (NOAA-15/-16/-17/-18/-19 and MetOp-02). Measurements began with NOAA-15 on 1 July 1998 and continue to the present. NOAA-17 failed on 10 April 2013, leaving only five satellites presently measuring using SEM-2 MEPED. Each satellite occupies a sun-synchronous polar orbit with a nominal altitude of 870 km, orbital period of 102 minutes, and an inclination of 98.7 degrees. The satellites are three-axis stabilized keeping their orientation fixed in the direction of motion and local zenith. A full description of the SEM-2 MEPED instrument can be found in *Evans and Greer* [2000], along with additional information in *Yando et al.* [2011].

The following description of SEM-2 MEPED will be limited to the telescope detectors. MEPED is designed to measure proton energies of 30 keV − 200 MeV and electron energies of 30 − 2500 keV. There are two sets of telescopes observing approximately zenith (0°) and ram (90°) directions. Each instrument set has a proton telescope and an electron telescope. The proton telescope has a stack of two silicon detectors (each 200 μm thick) mounted within an aluminum and tungsten housing. Above the detectors is a set of samarium-cobalt magnets which provide a strong magnetic field (~0.25 Tesla) designed to sweep away incident electrons. The electron telescope has a similar design to the proton telescope, but uses only one detector and no magnets. Proton counts are supposed to be subtracted from the electron detector using results from the

proton telescope. Particle energies are binned in each telescope using pulse-height analysis of detector output, which is described in greater detail by *Wüest et al.* [2007]. Specifics of pulse-height analysis in application to MEPED can be found in *Evans and Greer* [2000] and *Asikainen and Mursula* [2011]. Protons are reported in six channels P1 through P6, where P6 is an integral channel nominally measuring greater than 6900 keV protons. Channels P1 through P5 are differential channels that split up proton measurements with energies between 30 and 6900 keV. Electrons are reported in three integral channels E1 through E3, with nominal electron measuring at energies of greater than 30 keV, 100 keV, and 300 keV.

The MEPED instrument is known to have issues with proton detector degradation and cross-contamination from electrons and protons in both the proton and electron detectors. A detailed review of the proton detector degradation can be found in *Asikainen and Mursula* [2011] and *Asikainen et al.* [2012]. Work to correct for particle contamination issues will be presented in Chapter 3.

1.9 Motivation

EPP has significant impacts on the middle atmosphere by ionizing the atmosphere, resulting in NO_x and HO_x that destroys O_3, which in turn, alters atmospheric dynamics. These impacts have even been correlated to changes in polar surface temperatures [*Rozanov*, 2005; *Seppällä et al.*, 2009; *Baumgeartner et al.*, 2011]. A multi-model inter-comparison project focused on quantifying EPP-DE impacts on stratospheric O_3 [e.g., *Funke et al.*, 2011] show that models, including WACCM, accurately represent a SPE when not using MEE; however, other studies [e.g., *Smith*, 2012] indicate that descent rates in WACCM are not properly represented. In addition, there are likely unaccounted for sources of NO_x production, such as MEE, that are

required to simulate observed levels of stratospheric NO_x due to the EPP-IE [e.g., *Randall et al.*, 2014].

Observations of enhanced stratospheric NO_x in the Arctic spring of 2004 are used to exemplify these ongoing issues. Initial studies proposed that the increased NO_x was due to production during the October 2003 SPE [*Natarajan et al.*, 2004; *Seppälä et al.*, 2004; *Orsolini et al.*, 2005] followed by the EPP-IE. Subsequent work explored the role of meteorology in December 2003 and January 2004 [*Manney et al.*, 2005] and a theory emerged that was based on anomalous transport and not the SPE [e.g., *Randall et al.*, 2005]. When similar stratospheric meteorology and enhanced NO_x was observed again in 2009 [*Manney et al.*, 2009], despite low solar and geomagnetic forcing, it became widely accepted that anomalous descent was responsible for the NO_x enhancements [e.g., *Randall et al.*, 2009]. However, recent model analysis from *Randall et al.* [2014] showed that auroral particles do not fully explain the EPP-IE signal observed in 2004 and suggested that MEE precipitation may be necessary to reproduce the observations.

It has been long theorized that MEE and relativistic electron precipitation (REP) have profound impacts on the middle atmosphere climate [*Baker et al.*, 1987]. *Callis et al.* [1991] show globally integrated increases of EPP-NO_y from MEEs and REP of 35-40% from 1979 to 1985 using observations and 2D model calculations. The SOLar Atmospheric Coupling by Electrons (SOLACE) research effort provided further insights into the atmospheric impacts of MEE and REP [*Callis et al.*, 1998a, 1998b, 2001]. They used satellite observations of particles and of NO_y to estimate atmospheric impacts due to MEE and REP. Their results showed large (>20% near 25 km) increases in observed NO_y [*Callis et al.*, 1998a] and ~12% column increases from 25-40 km were reproduced in a 2D transport model using particle input [*Callis et al.*,

1998b]. Impacts from MEE and REP are significantly higher in the upper stratosphere (>25 km) [*Callis et al.*, 2001]. NO_x driven O_3 loss is dominant in the upper stratosphere while chlorine-driven O_3 loss is dominant at lower stratospheric altitudes (~20 km) [*Brasseur and Solomon*, 2005]. Thus, MEE and REP may be important contributors to total EPP-NO_x production and must be quantified to accurately simulate subsequent O_3 depletion.

Codrescu et al. [1997] incorporated observations of precipitating MEE from the SEM-1 MEPED on board the POES satellites into in the NCAR Thermosphere-Ionosphere-Mesosphere-Electrodynamic general circulation model (TIME-GCM). Results showed a 13% increase in HO_x at 78 km near 75°N in January, and an associated 25% decrease in O_3 at the same location. This decrease from EPP-HO_x follows the EPP-DE mechanism. There are important caveats to this work. Unfortunately, the data used by *Codrescu et al.* [1997] is known to have proton contamination of the electron data channels [*Evans and Greer*, 2000]. In addition, the hemispheric map input used in TIME-GCM was created using a statistical combination of satellite half orbits over the lifetime of all the satellites; thus daily variations are removed. The MEPED 0° detector was used to create the hemispheric maps, resulting in only a portion of the BLC included into the model simulations. How much an underestimate *Codrescu et al.* [1997] was is unknown since there are no observations of the total particle flux within the BLC. Finally, the TIME-GCM simulation was run for only 20 days and the results did not provide the time resolution or the atmospheric altitude range necessary to analyze the impacts from the EPP-IE mechanism. *Codrescu et al.* [1997] showed large impacts (>500% NO increase at 80 km in both hemispheres) from MEE precipitation on middle and upper atmosphere climate; however, the aforementioned issues with the data and the assimilation scheme prevented their work from gaining wide-spread acceptance. The goal of this work is to address the data and model

shortcomings that plagued *Codrescu et al.* [1997] and to revisit their work using the next generation of observations from the POES SEM-2 MEPED instrument. This is challenging since SEM-2 MEPED suffers from proton contamination of electron channels similar to its predecessor, has a limited range of magnetic local time (MLT) coverage per satellite, and has degradation in the proton measuring telescopes [*Evans and Greer,* 2000].

Given the issues of proton contamination and sparse data coverage by the POES SEM-2 MEPED, there have been several recent attempts to quantify the impacts of MEE indirectly. One attempt was to correlate EPP-HO_x production of OH with observations of precipitating particles. Results found MEPED 100-300 keV electron count rates could explain 56-87% of nighttime OH concentrations using the Microwave Limb Sounder (MLS) aboard the Aura satellite with observations from 71-78 km between 55 and 65° magnetic latitude during March 2005 and April 2006 [*Verronen et al.*, 2011]. Results showed that sensitivity of nighttime OH concentrations is strongly influenced by seasonal background H_2O concentrations controlled by the residual circulation. Similar results were found by *Andersson et al.* [2012] using observations from 2004 to 2009. Both studies suggested that mesospheric nighttime OH concentrations are a suitable proxy for MEE precipitation. Analysis of MEE using nighttime OH concentrations is complicated by correlations that vary as a function of longitude [*Andersson et al.,* 2014]. However, without more accurate measurements from the MEPED instrument, parameterization of MEE precipitation using nighttime OH concentrations is difficult to calculate. Another important result from these studies was that while the MEPED instrument measured high MEE precipitation values in the SAA, no correlations with mesospheric nighttime OH could be found. Therefore, it is believed that high MEE measurements by the MEPED instrument in the SAA

region are caused high energy proton contamination and should be treated with skepticism [*Andersson et al.*, 2014].

Several attempts to produce improved SEM-2 MEPED datasets have been made. *Lam et al.* [2010] attempted to remove proton contamination using the bow-tie method [e.g., *Selesnick and Blake*, 2000] combined with an assumption that the proton differential flux can be modeled using a series of exponential functions. *Asikainen et al.* [2013] created a new dataset through three steps. First they removed errors from proton detector degradation [e.g., *Asikainen et al.*, 2009]. Next they assumed the proton spectrum can be modeled using a series of power law functions. Finally they ran their proton spectra through a forward model using gathering power from *Yando et al*., [2011] to remove proton contamination from the electron channels. *Wissing and Kallenrode* [2009] used the Atmospheric Ionization Module Osnabruck (AIMOS) model to calculate MEE precipitation data and ionization rates. This model assimilated MEPED data and calculated an electron differential count flux spectrum using multiple power law fits between energy channels. A global map of particle precipitation rates was then produced using parameterizations that rely on a geomagnetic index (Kp). Unfortunately, the AIMOS model cannot account for errors in the raw MEPED data on which it is based. In addition, the model inherits errors by using Kp as a parameterization since MEE varies with geomagnetic activity in different ways depending on timing relative to SPEs [*Rodger et al.*, 2010a]. Ultimately all of these methods have limitations since they do not accurately calculate an error from their spectral distribution assumptions and they do not adapt to changing particle populations that can either be exponential, power law, or Maxwellian distributions.

Chapter 2 examines solar cycle impacts in the WACCM3 versus WACCM4 models in order to better understand how the newer model version simulates solar cycle variations. Chapter

3 presents a new correction method to POES SEM-2 MEPED data that does not assume a single spectral distribution for protons and electrons, and includes error bars that take into account measurement error and spectral shape fit errors. Chapter 4 uses the knowledge gained from Chapter 2 and the improved data from Chapter 3 to assimilate MEE precipitation on a daily basis into WACCM. This provides the first new direct insight into impacts of MEE precipitation on the middle atmosphere since *Codrescu et al.* [1997]. Chapter 5 summarizes the results of this work and gives insight into future development for studying MEE precipitation.

Chapter 2

Simulated solar cycle effects on the middle atmosphere: WACCM3 vs. WACCM4

This chapter includes the contents of *Peck et al.* [submitted, 2014a]. The goal of this chapter is to understand how the Whole Atmosphere Community Climate Model version 4 (WACCM4) simulates impacts from solar cycle; specifically focusing on solar spectral irradiance (SSI) and auroral energetic particle precipitation (EPP). WACCM4 is compared to WACCM version 3.1.9 (WACCM3), as well as observations and reanalysis.

The main results of this work are: (1) dynamical changes between WACCM4 and WACCM3 cause shifts in middle atmosphere chemical morphology (e.g., O_3 maximum is ~2 km higher in WACCM4) and dynamics; (2) increased winter polar descent in WACCM4 compared to WACCM3 causes greater sensitivity to the EPP Indirect Effect (EPP-IE); and (3) solar cycle variation in both versions of WACCM are in agreement with observations and reanalysis except for issues in zonal wind and temperature.

2.1 Introduction

To isolate and quantify climate-induced changes in the atmosphere, it is necessary to first understand natural variability in the Earth system. In the stratosphere, mesosphere, and lower thermosphere, there is a balance between non-linear dynamics, chemical interactions, and radiative processes [*Andrews et al.*, 1987; *Brasseur and Solomon*, 2005]. Since ozone (O_3) is an important radiatively active gas, processes affecting O_3 distributions must be well accounted for.

The goal of this work is to quantify the combined effects on O_3 from auroral electron precipitation and solar irradiance as represented in a state-of-the-art global climate model.

Energetic particle precipitation (EPP) produces odd hydrogen ($HO_x = H + OH$) [*Solomon et al.*, 1981], hereafter referred to as EPP-HO_x, and odd nitrogen ($NO_x = NO + NO_2$) [*Rusch et al.*, 1981], hereafter referred to as EPP-NO_x. EPP-HO_x in the lower mesosphere or upper stratosphere can deplete O_3 [e.g., *Damiani et al.*, 2010; *Jackman et al.*, 2011; *Sinnhuber et al.*, 2012], but this requires precipitation of particles that are higher in energy than auroral electrons, and is thus not relevant to this work. NO_x is photolyzed in the presence of sunlight, with a photochemical lifetime on the order of days or less in the mesosphere and lower thermosphere (MLT) [*Frederick et al.*, 1983; *Minschwaner and Siskind*, 1993; *Siskind et al.*, 1997]. During the dark polar winter, however, EPP-NO_x produced in the MLT can be transported to the stratosphere via the residual circulation, a process referred to as the EPP indirect effect [*Randall et al.*, 2006; 2007]. Once in the stratosphere EPP-NO_x can have significant impacts on stratospheric O_3 [e.g., *Jackman et al.*, 2009; *Randall et al.*, 1998, 2001; *Semeniuk*, et al., 2011; *Seppälä et al.*, 2007] since the NO_x catalytic cycle is the primary loss mechanism for odd oxygen between 25 km and 40 km [*Garcia and Solomon*, 1994; *Watson et al.*, 1986].

The majority of stratospheric NO_x is produced via the reaction of N_2O that originates in the troposphere with $O(^1D)$ [*Crutzen*, 1971; *Jackman et al*., 1980]. However, EPP-NO_x descent into the stratosphere contributes to the NO_x budget; *Randall et al*. [2007] estimated that in years with high amounts of particle precipitation, EPP-NO_x constitutes as much as 40% of total NO_x in the polar stratosphere. Model calculations suggest that EPP-NO_x induced O_3 changes lead to stratospheric circulation changes that affect temperatures down to the surface [*Rozanov et al.*,

2005; *Seppälä et al*., 2009; *Baumgaertner et al*., 2011] via mechanisms similar to a descending Northern annular mode (NAM) [*Baldwin and Dunkerton*, 2001]

Middle-atmosphere O_3 also depends on variations in solar irradiance. The total solar irradiance only changes by about 0.1% during the 11-year solar cycle; however ultraviolet (UV) radiation from 200-250 nm can change by 4-8% [*Lean et al.,* 1997]. Stratospheric O_3 changes during the solar cycle have been well documented [e.g., *Haigh,* 1994; *Soukharev and Hood*, 2006; *Frame and Gray,* 2010; *Gray et al.*, 2010; *Merkel et al*., 2011]. Results show high tropical O_3 at both 20 km and 45 km during solar maximum compared to solar minimum, and increases or decreases in polar O_3, depending on altitude. Results of these studies will be compared in more detail to this work in Section 2.3.

Solar cycle changes in solar spectral irradiance (SSI) can impact O_3, temperature, and winds in the stratosphere and lower mesosphere via the "top-down" mechanism [*Gray et al.*, 2010, and references therein]. This refers to the influence on stratospheric temperatures and winds from solar irradiance-induced changes in O_3 production and heating, followed by stratosphere-troposphere coupling. Increased UV radiation during solar maximum leads to more O_3 production, primarily in the middle-to-upper stratosphere at low latitudes. Both the increased irradiance and increased O_3 lead to increases in the local temperature. This, in turn, changes the meridional temperature gradient and the zonal winds through thermal wind balance [*Gray et al.*, 2010, and references therein]. As suggested by *Hines* [1974], solar cycle-induced changes in upper stratospheric winds then affect planetary wave propagation at lower altitudes. For example, *Kodera and Kuroda* [2002] suggested that solar cycle influences on the upper stratosphere lead to changes in the middle and high latitude lower stratosphere via effects on the

polar night jet. Finally, the top-down mechanism leads to additional changes in temperature by redistributing O_3 concentrations through planetary wave feedbacks [*Gray et al*., 2009].

The quasi-biennial oscillation (QBO) also affects solar cycle impacts on middle atmosphere temperatures and dynamics [*Gray et al.,* 2010, and references therein]. *Matthes et al.* [2013] showed that the east phase QBO generates poleward-downward propagating easterly wind anomalies in the Northern Hemisphere (NH) winter, creating disturbed atmospheric conditions. This work does not explicitly examine QBO phase dependencies, but inferences are made about the net effect of having a QBO or not.

Marsh et al. [2007] (hereafter referred to as M07) used the Whole Atmosphere Community Climate Model version 3.1.9 (WACCM3) to simulate the combined effects on the atmosphere from changes in solar irradiance and EPP between solar minimum and solar maximum conditions. Relevant to the work presented here, M07 calculated solar cycle changes in stratospheric O_3, NO_y (NO + NO_2 + NO_3 + N_2O_5 + HNO_3 + HO_2NO_2 + $ClONO_2$), temperature, and zonal winds. Subsequent to M07, a new version of WACCM was introduced, WACCM4, which had several improvements that are described below. In this paper, results from M07 will be compared to results from WACCM4, to show the sensitivity of calculated solar cycle effects to the model modifications. Section 2.2 describes WACCM4, notable changes from WACCM3, and the simulations analyzed in this work. Section 2.3 quantifies differences due to changing model versions. Section 2.4 presents solar-cycle dependencies from WACCM4 and compares them to M07 and to other work. Conclusions are given in Section 2.5.

2.2 Whole Atmosphere Community Climate Model

This work presents the solar cycle response in simulations using WACCM4 and compares the results to previously published WACCM3 simulations [M07]. WACCM4 is

described in detail in *Marsh et al.* [2013] and is part of the Community Earth System Model (CESM) version 1.0.4 framework developed by the National Center for Atmospheric Research [*Hurrell et al.*, 2013]. WACCM4 is an extension of the Community Atmosphere Model version 4 (CAM4) described in *Gent et al.* [2011]. CAM4 uses a finite-volume dynamical core [*Lin*, 2004]. The vertical extent of WACCM4 runs from the Earth's surface to the lower thermosphere (~145km) with 66 vertical hybrid levels that are isobaric above ~100 hPa. The vertical resolution increases with altitude, ranging from 1.1 km in the troposphere, to 1.5 km near 50 km and 3.5 km above ~65 km. The horizontal resolution used here is 1.9° latitude by 2.5° longitude. WACCM4 uses the Model for Ozone and Related Chemical Tracers version 3 (MOZART3), described in *Kinnison et al.* [2007], as its chemistry module. The parameterization of non-orographic gravity waves is as described in *Richter et al.* [2010]. A surface stress due to unresolved topography termed turbulent mountain stress (TMS) is included; this has led to an improvement in the frequency of NH Sudden Stratospheric Warmings (SSWs) [*Richter et al.*, 2010; *Marsh et al.*, 2013]. Sea surface temperatures are based on a merged 1982-2001 climatology product between HadISST1 and OI.v2 on the CAM grid [*Hurrell et al.*, 2008]. Auroral EPP is as described in M07; it varies with hemispheric power that is estimated using the K_p planetary geomagnetic index [*Maeda et al.*, 1989]. SSI used to characterize the solar cycle varies with spectral range in WACCM4. For wavelengths shorter than 121 nm, a parameterization based on f10.7 is used [*Solomon and Qian*, 2005]. For longer wavelengths, WACCM4 uses SSI as described in *Lean et al.* [2005].

WACCM3 uses the same SSI parameterization as WACCM4 for wavelengths shorter than 121 nm, but the model of *Woods and Rottman* [2002] for longer wavelengths. Figure 2.1 shows the solar maximum (solid) and solar minimum (dotted) SSI input for WACCM3 (black)

and WACCM4 (red) in the top panel. The bottom panel shows the differences between solar maximum and solar minimum (solid) in both model versions and these differences multiplied by ten (dotted) for clarity. At wavelengths longer than ~180 nm, the solar cycle differences in SSI input in WACCM3 and WACCM4 are very similar. However, between 121 nm and 165 nm WACCM4 shows smaller changes between solar maximum and solar minimum than WACCM3; just the opposite is true from 165-180 nm. These spectral regions include the molecular oxygen Schumann-Runge and Herzberg absorption bands, so SSI-induced differences in the MLT between WACCM3 and WACCM4 are expected.

Other notable differences between WACCM3 and WACCM4 of particular relevance to the work presented here are as follows. The WACCM3 simulations in M07 used a coarser horizontal grid of 4° latitude by 5° longitude. WACCM3 uses dynamics from CAM3 and is a stand-alone atmospheric model, whereas WACCM4 is integrated into the CESM framework and uses CAM4 dynamics. The WACCM3 simulations shown here from M07 do not have either a spontaneously generated or externally forced QBO [*Garcia et al.,* 2007], whereas WACCM4 explicitly forces a QBO as described in *Matthes et al.* [2010]. The QBO causes changes to background temperature, zonal winds, the residual circulation, and the distribution of chemical constituents affected by transport processes [e.g., *Trepte and Hitchman,* 1992; *Hansen et al.,* 2013]. Inclusion of the QBO in WACCM4 will cause a westerly shift in equatorial zonal winds below 50 hPa compared to WACCM3 when averaged over several years. WACCM3 uses a seasonally and latitudinally varying specified source function for non-orographic gravity waves, rather than one triggered by convection and frontal/baroclinic systems. WACCM3 does not include parameterized TMS and has relatively few SSWs. Finally, WACCM4 uses chemical
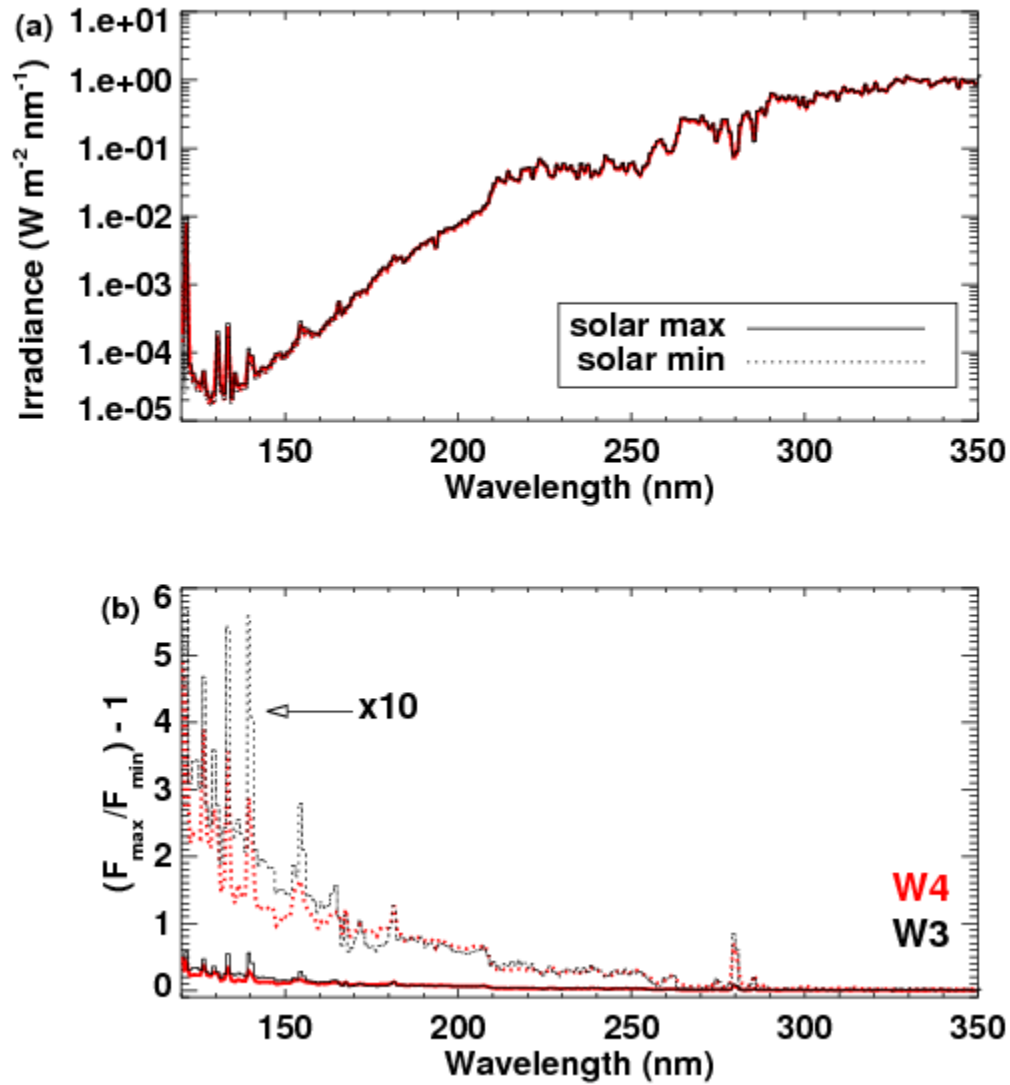
Figure 2.1: (a) Spectral irradiance (W m^{-2} nm^{-1}) between 120 nm and 350 nm for solar maximum (solid) and solar minimum (dotted) in WACCM3 (black) and WACCM4 (red). (b) Change in spectral irradiance from solar minimum to solar maximum (solid) in both model versions and these differences multiplied by 10 (dotted) for clarity.

reaction rate constants from *Sander et al.* [2006], whereas WACCM3 uses those from *Sander et al.* [2003].

A description of the model simulations presented in the remainder of this work is as follows. Table 2.1 lists the solar and geomagnetic input values for the two WACCM4 simulations used here. These two WACCM4 simulations are analogous to the M07 solar maximum and solar minimum simulations to which they are compared. Both WACCM4 simulations were run for 42 years, with 2 years removed for spinup, leaving 40 years from which to extract results. The WACCM3 simulations presented in M07 were 30 years in length after spinup.

2.3 Differences due to model version: WACCM4 compared to WACCM3

The following section shows 40-year zonal mean annual averages and related analysis for O_3, NO_y, temperature, and zonal winds in WACCM4 compared to 30-year averages in WACCM3. Since annual averages are used for this analysis, NO_y is a more applicable constituent to follow than NO_x since it captures both NO_x and its reservoir species. WACCM4 output was interpolated to the WACCM3 grid for direct comparison. Differences are presented in actual (vs. percent) values to emphasize absolute differences. All results are for solar minimum and low auroral EPP conditions, so the differences presented in this section are attributed only to changes in the model and not to variations in SSI or EPP over the solar cycle.

Figure 2.2 shows multi-year, annual average zonal mean O_3 during solar minimum in both WACCM versions, and their differences. Overall, the distribution of O_3 is in good agreement between model versions. The following differences are noteworthy: Between ~10 hPa and ~1 hPa (~35 km to 55 km), O_3 in WACCM4 is higher than in WACCM3 at all latitudes. Between ~100 hPa and ~10 hPa (~20 km to 35 km), WACCM4 O_3 is lower at all latitudes.

Name	Solar Flux f10.7	Ap (Kp) Index	SSI Data Year
Solar Min	72	3 (2/3)	1996
Solar Max	210	27 (4)	2000

Table 2.1: Specification of solar flux and geomagnetic activity for WACCM4 simulations.
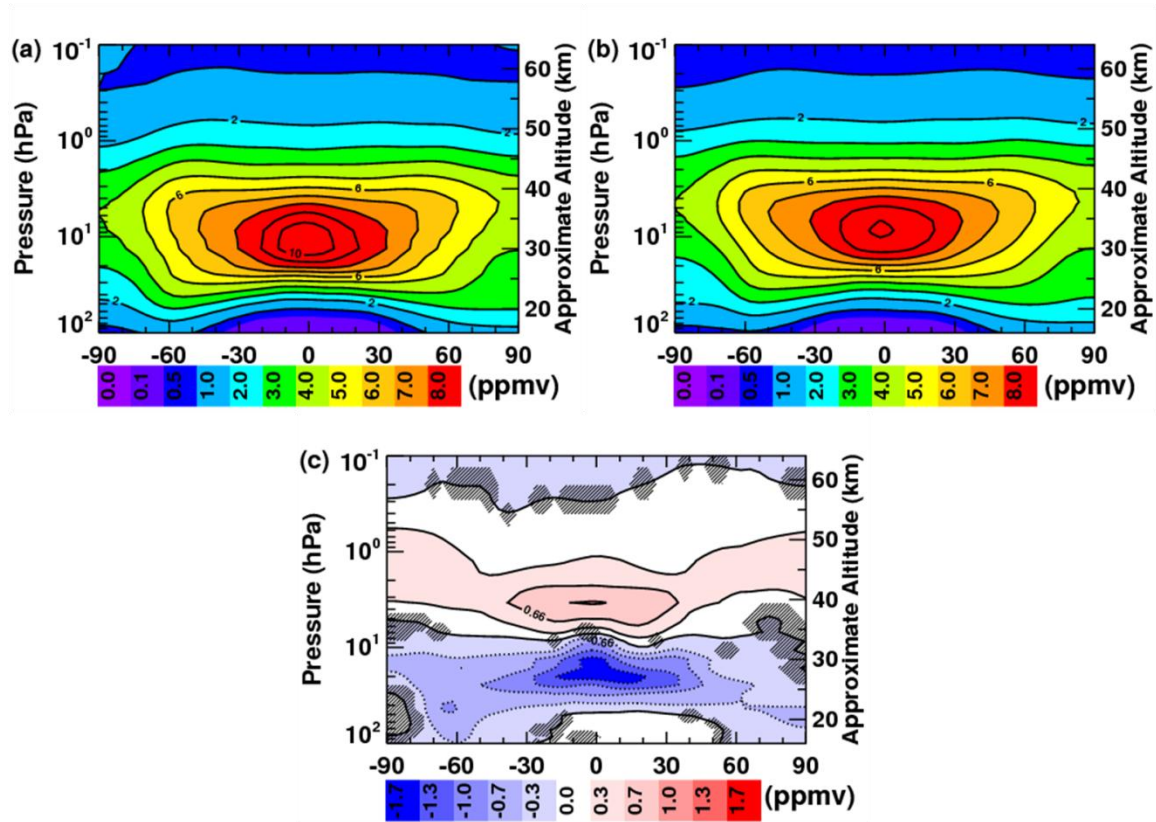
Figure 2.2: Multi-year annual mean zonal mean O_3 (ppmv) for (a) WACCM3, (b) WACCM4 and (c) the model version difference in O_3 (WACCM4-WACCM3) during solar minimum conditions. Black contours in plots (a) and (b) occur every 1 ppmv, and in (c) every 0.33 ppmv. Unshaded areas represent 95% statistical significance using the Student's T-test.

Maximum (~15%) differences occur in the tropics, and reach about +1 ppmv near 4 hPa and -1.5 ppmv near 20 hPa. These differences result in part because the O_3 mixing ratio profiles in WACCM4 are displaced to slightly higher altitudes relative to WACCM3. For instance, the equatorial maximum in WACCM3 is at 11 hPa, whereas in WACCM4 it is at 8 hPa; the polar maxima are close to 6 hPa in WACCM3 and 5 hPa in WACCM4. The vertical profile displacement suggests that one cause of the differences is most likely changes to the circulation from different horizontal resolution [see *Hamilton et al.,* 1999], gravity wave parameterization, or QBO treatment in WACCM4 vs. WACCM3. WACCM4 has both an easterly and westerly QBO phase, while WACCM3 is perpetually easterly; thus a comparison of WACCM4 to WACCM3 is similar to QBO west (QBOW) minus QBO east (QBOE), but with a smaller magnitude. Positive O_3 differences atop negative differences for QBO-noQBO simulations are consistent with *Punge and Giorgetta* [2008] (see their figures 11 and 12) and with the QBOW minus QBOE differences shown by *Hansen et al.* [2013] (see their figure 6).

Figure 2.3 compares the annual cycle of total column O_3 between 80°S and 90°S in WACCM3 (green) and WACCM4 (red) to O_3 derived with the IMK/IAA level-2 data processor from the Michelson Interferometer for Passive Atmospheric Sounding (MIPAS) spectral data (black) [*Fischer et al.*, 2008]. This comparison examines the ozone hole region. Retrieval information for MIPAS O_3 measurements can be found in *von Clarmann et al.* [2009]. The MIPAS data was interpolated to the WACCM4 grid for a more direct comparison between the observations and models using the method described in *Brakebusch et al.* [2013]. MIPAS for solar minimum comes from years 2007-2009. WACCM3 and WACCM4 are similar throughout the year, and are generally lower than MIPAS but within observed variability. Column O_3 is roughly constant in WACCM3, WACCM4, and MIPAS from February to August, with average
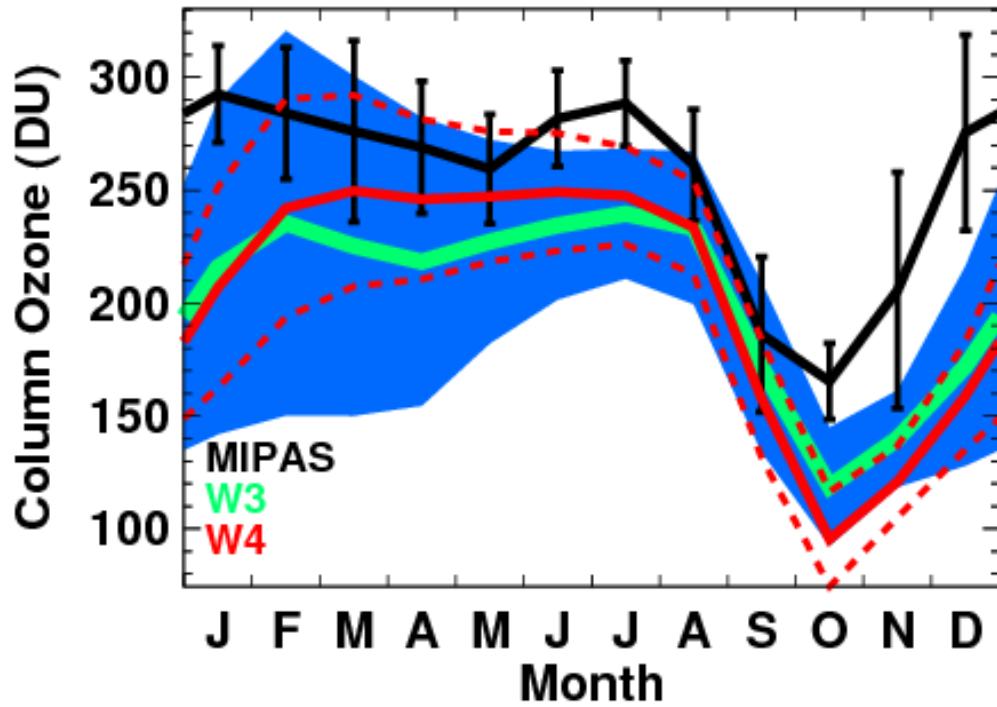
Figure 2.3: Multi-year mean monthly averaged total column ozone during solar minimum averaged over 80-90°S. The green solid line and surrounding blue shading are WACCM3 averages and 2-sigma variability, respectively. The red solid line and red dashed lines are WACCM4 averages and 2-sigma variability, respectively. The black lines are averages based on MIPAS data with 2-sigma variability bars.

values over this time period near 230, 250, and 280 DU, respectively. All three time series show large declines due to the annual Antarctic ozone hole from August to October, followed by recovery. The minimum O_3 column in WACCM3 and in WACCM4 is lower than in MIPAS, which follows from the lower values prior to the O_3 hole. The total loss inferred from MIPAS, ~120 DU, is close to that seen in WACCM3 (~110 DU) and somewhat less than in WACCM4 (~150 DU). Therefore, catalytic O_3 loss in the SH spring is properly modeled. During the rest of the year, polar stratospheric O_3 is dynamically controlled below ~25 km [*Garcia and Solomon*, 1985]. Analysis of partial column O_3 below 25 km (not shown) demonstrates a consistent low bias in WACCM. This suggests insufficient meridional transport of high tropical ozone into the polar latitudes especially in December.

Figure 2.4 compares WACCM3 and WACCM4 multi-year, annual average zonal mean NO_y. Thick, white contours are carbon monoxide (CO), which is used as a proxy for descent from the mesosphere. Qualitatively the distribution of NO_y is similar between model versions, but there are systematic, quantitative differences. NO_y is 2 ppbv to 4 ppbv lower in WACCM4 than in WACCM3 throughout the tropical and midlatitude stratosphere and up to 5 ppbv lower near 30° N and 5 hPa. In the polar upper stratosphere and mesosphere, NO_y is 1 ppbv to 6 ppbv higher in WACCM4 than in WACCM3. In the lower stratosphere, NO_y in WACCM4 is slightly higher than in WACCM3 in the Antarctic, but slightly lower in the Arctic. Like O_3, negative tropical differences are likely caused by differences in SSI and dynamical changes associated with the QBO. Since production of NO_x by EPP is similar in both model versions, higher polar NO_y in the upper stratosphere and mesosphere (especially in the Antarctic) in WACCM4 is attributed to faster descent rates in the WACCM4 MLT, which result in ~20% more EPP-NO_x
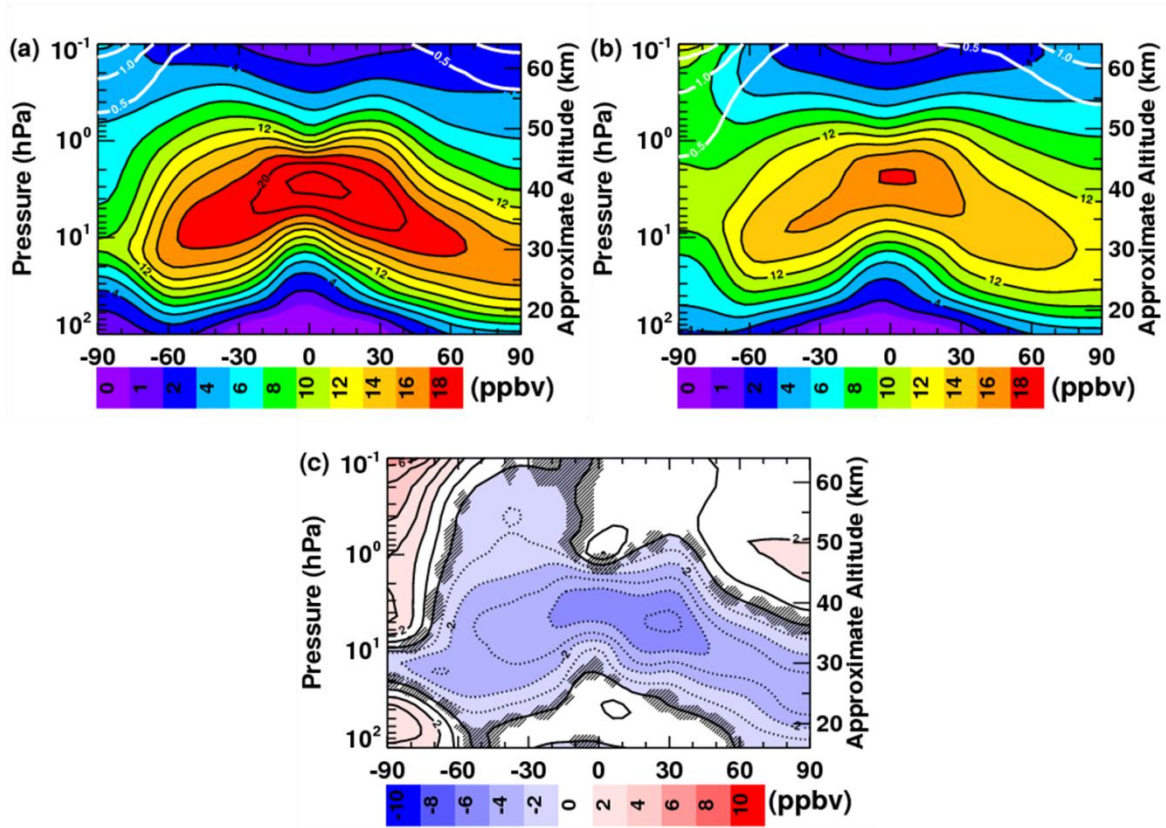
Figure 2.4: Same as Figure 1 but for NO$_y$. Black contours in (a) and (b) are every 1 ppbv, and in (c) every 2 ppbv. White contours in (a) and (b) are CO every 0.5 ppmv.

being transported downward into the upper stratosphere during polar winter. Faster descent rates are corroborated by more CO at lower polar altitudes in WACCM4 than in WACCM3.

Figure 2.5 shows multi-year, annual average zonal mean temperature comparisons between WACCM3 and WACCM4. The overall temperature structure is in general agreement between model versions; however, significant positive and negative differences exist throughout the middle atmosphere. Temperatures in WACCM4 are lower than in WACCM3 by up to 15 K throughout most of the mesosphere, by up to 25 K in the Antarctic middle and upper stratosphere, and by less than 5 K at most latitudes in the lower stratosphere. Temperatures in WACCM4 are higher than in WACCM3 by up to ~10 K in the polar lower mesosphere in both hemispheres, and by less than 5 K in the tropical and midlatitude upper stratosphere. Lower temperatures in WACCM4 in the tropical mesosphere improve upon a known 10-20 K warm bias in WACCM3 (see Figure 1 in *Smith* [2012]), likely as a result of improved gravity wave parameterizations. Lower temperatures in the Antarctic stratosphere in WACCM4 suggest that the cold pole problem described in *Marsh et al.* [2013] is exacerbated in the newer model version. Higher temperatures in the subtropical upper stratosphere are consistent with co-located increases in O_3 in WACCM4 (see Figure 2.2c), which leads to more UV absorption at these altitudes than in WACCM3. Dynamics responsible for the O_3 changes could also independently affect temperature through adiabatic processes; increased descent in the polar mesosphere would explain the higher temperatures there in WACCM4, for instance.

Figure 2.6 shows multi-year, annual average zonal mean zonal wind in WACCM3 and WACCM4. While the zonal wind structure is in good agreement between model versions, it is apparent that tropical easterly winds are weaker in WACCM4 and the Antarctic westerly polar night jet extends higher into the mesosphere in WACCM4 compared to WACCM3. Figure 2.6c
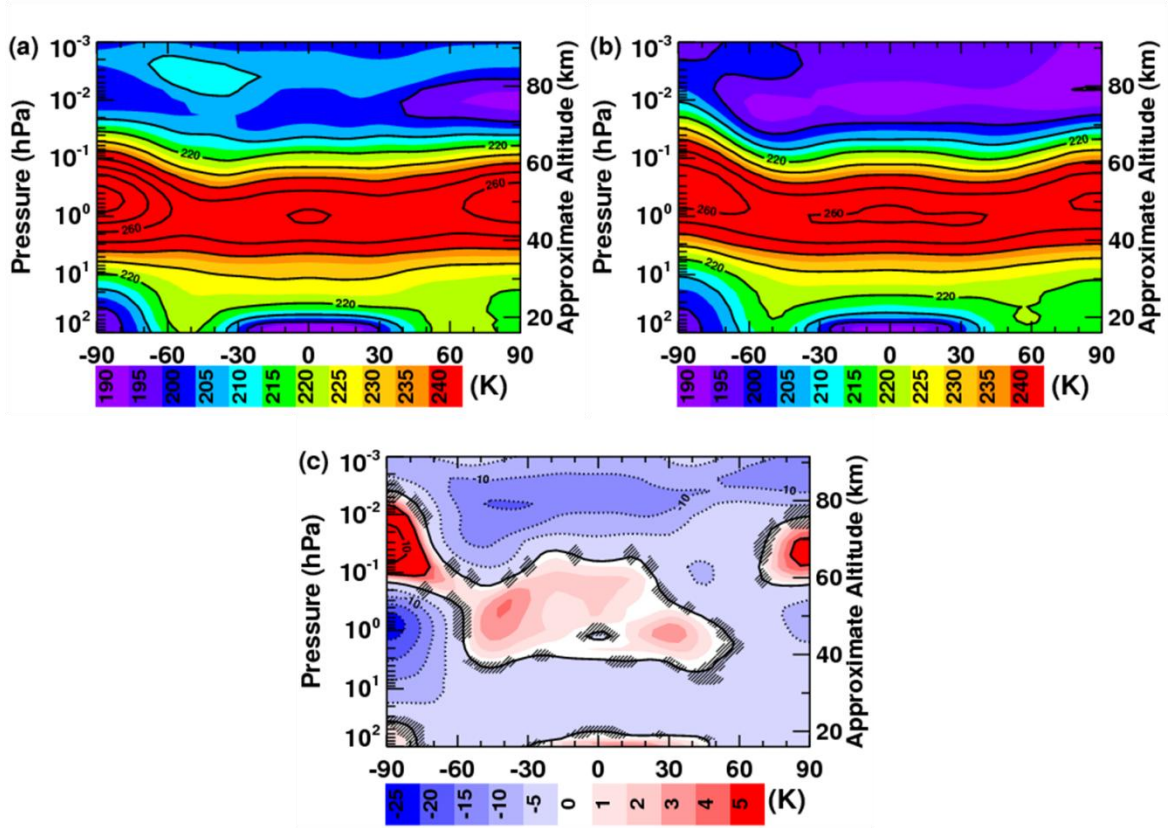
Figure 2.5: Same as Figure 1 but for temperature. Black contours in (a) and (b) are every 10 K, and in (c) every 5 K.
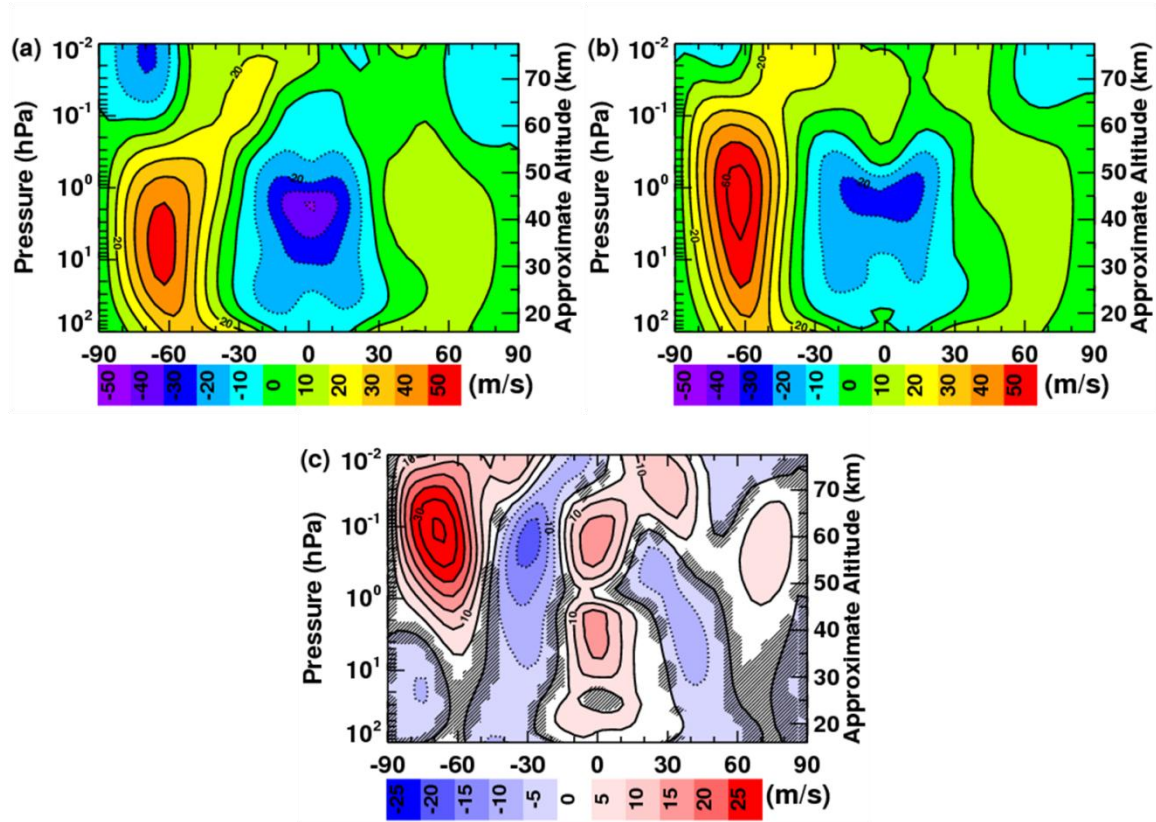
Figure 2.6: Same as Figure 1 but for zonal wind. Black contours denote intervals of 10 m/s in (a) and (b), and 5 m/s in (c).

highlights these prominent differences as well as more subtle differences elsewhere. WACCM4 shows a shift toward more positive (westerly) middle atmosphere wind speeds in the tropics and at high latitudes. The change to the equatorial winds is likely caused by inclusion of the QBO in WACCM4, which has a westerly phase in the equatorial region that is otherwise absent in WACCM3. Negative differences in the subtropics largely reflect a poleward shift of the polar night jet. In addition to the poleward shift of the jet, WACCM4 also has a 10 m/s stronger polar night jet in the Antarctic, and the jet core is located ~5 km higher in altitude. Changes to the Antarctic polar night jet are the result of the non-orographic gravity wave parameterizations between model versions and the exacerbated cold-pole problem in WACCM4. While the Antarctic polar night jet is known to be too strong in the winter [*Smith*, 2012], the upward extension of the westerlies into the mesosphere is an improvement over WACCM3 and results in a more accurate representation of the Antarctic vortex in the lower mesosphere, as shown next.

A comparison of polar vortices in WACCM3, WACCM4, and 36 years (1979-2014) of the Modern-Era Retrospective Analysis for Research and Applications (MERRA) is shown in Figure 2.7. A detailed description of MERRA can be found in *Rienecker et al.* [2011]. The vortex edge is defined using the method described in *Harvey et al.* [2002]. Annual cycles consist of multi-year, monthly means. The top row represents the NH and the bottom row represents the Southern Hemisphere (SH). The columns from left to right are plotted on the 3000 K, 1600 K, and 700 K isentropic surfaces, which correspond to altitudes of approximately 60 km, 45 km and 30 km, respectively. The vortex edge (50% frequency) is shown in green for WACCM3, red for WACCM4, and black for MERRA. Blue shading, red dashed lines, and black vertical lines indicate 25% to 75% frequency of occurrence. The x-axes in the top panels are shifted so that the winter season is in the middle of each plot. In the NH (top row) at 3000 K, WACCM3
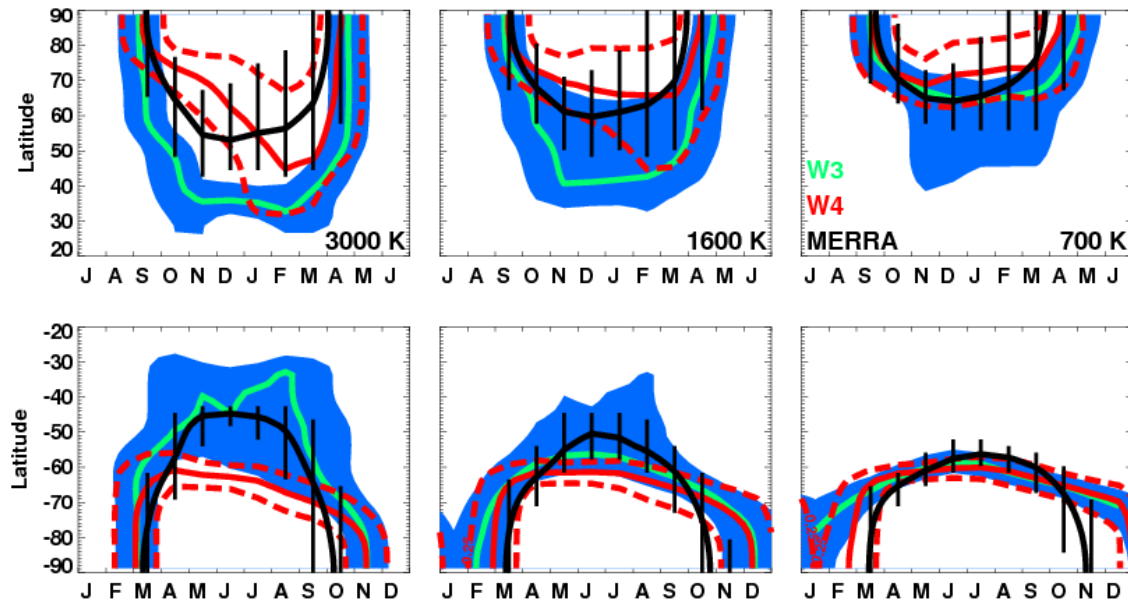
Figure 2.7: Multi-year mean monthly mean annual cycle showing the latitudinal extent of the polar vortices in the NH (top) and SH (bottom). A two dimensional boxcar smoother is applied. Columns from left to right correspond to potential temperatures of 3000 K, 1600 K, and 700 K. Thick solid contours denote the vortex edge, as indicated by where the vortex was present 50% of the time. Variability is marked by showing 25% to 75% of the time the vortex was present. The green solid line and surrounding blue shading are WACCM3. The red solid line and red dashed lines are WACCM4. The black line and vertical bars are MERRA.

overestimates the equatorward extent of the Arctic polar vortex throughout the entire season compared to MERRA. In the winter, the edge of the vortex is near 55° N in MERRA and 35° N in WACCM3; this translates to the model overestimating the vortex area by a factor of 2.3. While the vortex in WACCM4 is still too large in the NH spring, vortex area overestimation is largely alleviated in the new model version. Likewise near 1600 K, the Arctic vortex in WACCM3 extends much too far equatorward throughout the season, whereas the WACCM4 vortex is in good agreement with MERRA, including increased variability in the spring. In the lower stratosphere near 700 K the vortex is in good agreement between both model versions and MERRA, though midwinter variability in WACCM3 exceeds observations. At all levels shown, the vortex in WACCM3 (WACCM4) persists 2-4 (1-2) weeks longer than in MERRA.

In the Antarctic (bottom row), the WACCM3 vortex at 3000 K extends to latitudes equatorward of 40° S during winter, much too far equatorward compared to MERRA. This reflects the low latitude of the SH westerly jet near 60 km in Figure 2.6a. In WACCM4 and in MERRA, the Antarctic polar night jet in the stratosphere extends upward beyond 60 km and this reduces the latitudinal extent of the SH vortex. Note however, that the SH westerly jet in WACCM4 does not tilt equatorward with altitude as indicated by both MERRA and the Upper Atmospheric Research Satellite (UARS) Reference Atmosphere Project (URAP) [*Swinbank and Ortland*, 2003] zonal wind climatology (See Figure 2 in *Smith* [2012]). This results in an underestimation of the mesospheric vortex area in WACCM4 at 3000 K. At 1600 K, the Antarctic vortex in both model versions is smaller compared to MERRA during mid-winter. This is due to the ~10° latitude poleward shift of the Antarctic polar night jet in both WACCM versions compared to MERRA and to URAP (Figure 2 in *Smith* [2012]). In the lower stratosphere near 700 K, the SH vortex latitudinal extent in both WACCM versions agrees with

MERRA during the winter. However, large differences remain in vortex duration with the vortex in WACCM4 forming ~2 weeks early and lingering ~1 month longer compared to MERRA, and the vortex in WACCM3 persisting year-round at this altitude. This reflects continued challenges to accurately simulate observed temperatures in the Antarctic polar stratosphere.

2.4 Solar Cycle induced changes in WACCM

This section compares the solar cycle response in WACCM3 and WACCM4. This is achieved by showing differences between simulations for the solar "max" and solar "min" conditions defined in Table 2.1 and Figure 2.1. Comparisons focus on zonal mean annual averages and related analysis for ozone, NO_y, temperature, and winds. Hereinafter the solar maximum minus solar minimum differences are referred to as ΔX, where X is the constituent of interest; i.e., O_3, NO_y, temperature, or zonal winds. Differences are expressed as a percent equal to solar maximum minus solar minimum divided by solar minimum and multiplied by 100. Approximate altitude is calculated using a linear interpolation from the global, annual average geopotential height from the highest pressure level to the lowest pressure level seen in the figure. Differences that are not statistically significant at the 95% confidence level are indicated with black shading.

Figures 2.8a and 2.8b show multi-year, annual average zonal mean WACCM3 and WACCM4 ΔO_3, respectively. Here, as in M07 (see their Figure 7), there is a 2%-3% increase in O_3 throughout the midlatitudes and equatorial stratosphere during solar maximum (positive differences). O_3 is produced in the stratosphere via photodissociation of molecular oxygen (O_2) by solar UV radiation, followed by a reaction of an oxygen atom with O_2 [e.g., *Chapman*, 1930; *Johnston*, 1975]. Therefore, the O_3 increases are an expected result of increasing UV radiation
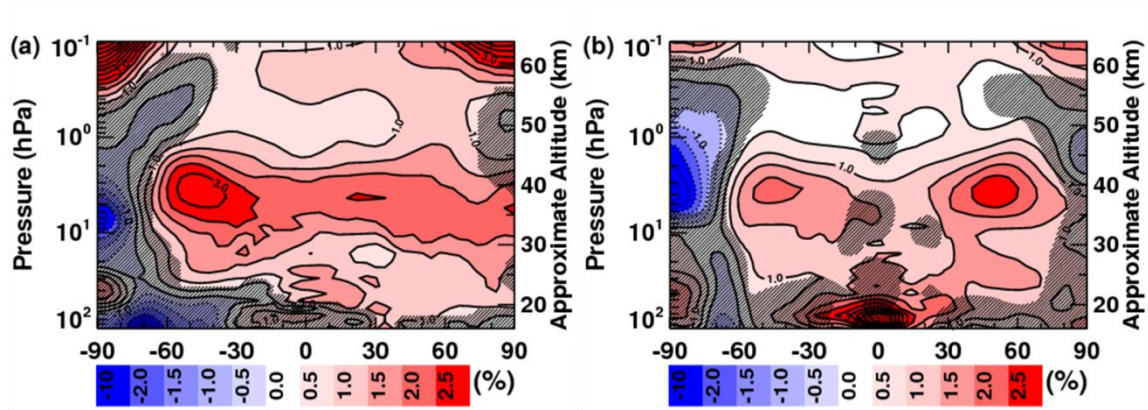
Figure 2.8: Multi-year annual mean zonal mean ΔO_3 (solar maximum minus solar minimum) for (a) WACCM3 and (b) WACCM4. Differences are expressed as a percent change relative to solar minimum. Non-shaded areas are statistically significant to 95% using Student's T-test. Black contours are every 0.5%.

during solar maximum. The O_3 increase in WACCM4 is smaller than in WACCM3 and has a smaller area of statistical significance, except near 4 hPa and 45°N, where the WACCM4 increase is larger. Figure 2.1 shows that SSI in the molecular oxygen Herzberg continuum increases more at solar max in WACCM 4 than in WACCM3 near 200 nm, but less near 215 nm. Since the differences in ΔO_3 between WACCM3 and WACCM4 in Figure 2.8 are only on the order of ~1%, it is plausible that changes in SSI input in WACCM4 caused these differences.

Soukharev and Hood [2006] show annual average, zonal average comparisons of solar maximum and solar minimum O_3 profiles using version 8 Solar Backscatter Ultraviolet (SBUV/2) data from 1979-2003 [*Frith et al.*, 2004], version 6.2 Stratospheric Aerosol and Gas Experiment (SAGE II) data from 1984-2003, and version 19 UARS Halogen Occultation Experiment (HALOE) data from 1991-2003 [*Remsberg et al.*, 2001]. SAGE II showed O_3 increases of 4% at 30° S and 3 hPa from solar min to solar max. SBUV/2 had maximum ΔO_3 of 3% at 50° S and 7 hPa. HALOE showed two middle stratospheric peaks in ΔO_3 of 4% at 20° S, 10 hPa and 40° N, 17 hPa. The midlatitude ΔO_3 maxima simulated in WACCM are in general agreement with the observed peaks in ΔO_3, suggesting that both WACCM model versions (especially WACCM4) are capturing observed solar cycle variability in O_3.

Another important feature in Figure 2.8 is a larger region of statistically significant O_3 decrease in the Antarctic polar upper stratosphere in WACCM4 compared to WACCM3. O_3 loss in this region is attributable to catalytic destruction by EPP-NO_x, which is larger during solar maximum than solar minimum. WACCM4 shows a larger increase in EPP-NO_x descent at solar max than WACCM3 (see Figure 2.9 below), thus resulting in more O_3 loss at solar max. This is consistent with the explanation of the WACCM3 vs. WACCM4 differences in solar min NO_y in Figure 2.4, that descent rates in the mesosphere are higher in WACCM4.

Figure 2.9 is analogous to Figure 2.8 but displays ΔNO_y. The 1%-5% decrease in low-latitude stratospheric NO_y during solar maximum is small but statistically significant in both model versions. As discussed by M07, this decrease is probably caused by increased NO photolysis at solar maximum, followed by reaction of the resulting atomic nitrogen with NO, yielding a net loss of NO_y [see also *Minschwaner and Siskind*, 1993]. Large (>50%) positive differences occur in the upper stratosphere and lower mesosphere at high latitudes. During solar maximum there is a larger EPP-NO_x reservoir in the MLT, thus increased descent rates transport more of the reservoir of EPP-NO_x, enhancing the impacts of the solar cycle in the polar stratosphere. Larger ΔNO_y values extend to lower altitudes (especially in the Antarctic) in WACCM4 compared to WACCM3, and this is due to the stronger winter descent inferred from CO distributions in WACCM4 (see Figure 2.4).

The daily average WACCM4 altitude-time series at 90°S of ΔNO_y and ΔO_3, averaged over all years, are shown in Figures 2.10a and 2.10b, respectively; see M07 Figures 2.9a and 2.9b for comparisons to WACCM3. Both Figure 2.10a here and Figure 2.9a in M07 show that NO_y produced by EPP in the MLT descends into the stratosphere during winter and spring. Since there is more EPP-NO_x during solar maximum the difference is positive. The 200% percent increase in NO_y descending to 0.9 hPa in August in WACCM4 is twice as large as in WACCM3. M07 showed ~25% increases in WACCM3 NO_y at 10 hPa in December, whereas the corresponding increases in WACCM4 exceed 50%. Statistically significant 5% negative differences in WACCM4 between January and May are photochemically driven and agree with M07. These regions of negative ΔNOy are likely the result of NO_y being removed in the presence of increased SSI at solar maximum during the SH summer and fall. This affects higher altitudes first and becomes significant at lower altitudes over the course of several months; it is
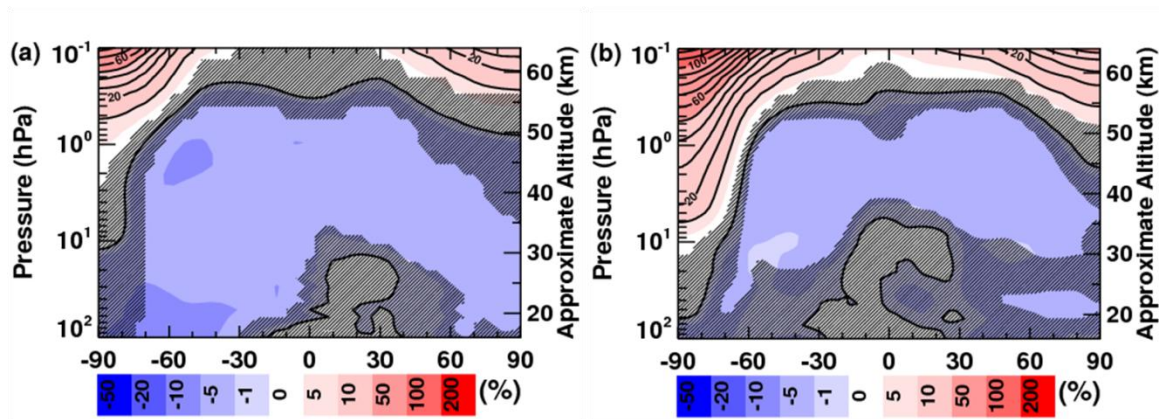
Figure 2.9: Same as Figure 2.8 but for ΔNO_y. Black contours are every 10%.
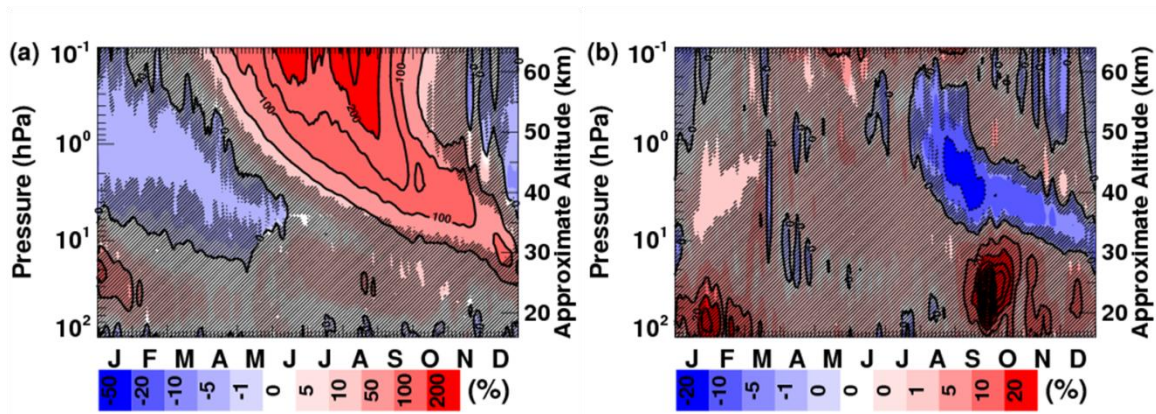
Figure 2.10: Multi-year daily mean zonal mean annual cycle at 90°S of (a) ΔNO_y and (b) ΔO_3. Non-shaded areas are statistically significant to 95% using Student's T-test. Black contours in (a) are every 50% and in (b) are every 10%.

caused by an increase in NO photolysis at solar max, as discussed above in the context of Figure 2.9.

Figure 2.10b shows the corresponding altitude-time series of ΔO_3. Statistically significant 5% to 20% O_3 decreases during solar maximum descend from ~1 hPa in late August to ~10 hPa in December. This decrease is attributed to EPP-NO_x induced loss, as it coincides with the solar maximum increase in NO_y. Similar differences were shown by M07 (see their Figure 9b), but the maximum O_3 loss in WACCM4 is 2-4 times larger than in WACCM3. This is consistent with the larger increase in NO_y during solar maximum in WACCM4 compared to WACCM3. *Randall et al.* [1998] showed evidence for EPP-NO_x-induced O_3 loss near the South Pole in late September of 1994 of ~25% near 30 km (~10 hPa). The only two solar proton events in 1994 occurred in February and October, so the EPP-NO_x increase shown by *Randall et al.* [1998] was likely produced by energetic electrons. Thus the magnitude of the O_3 loss in both WACCM versions is reasonably consistent with observations, although the timing of the NO_x descent and consequent O_3 loss is different than observed.

Figure 2.11 summarizes the multi-year, annual average zonal mean total column ΔO_3 in WACCM3 (green), WACCM4 (red), ground-based observations (dashed black) and satellite observations (solid black) as a function of latitude. Two standard deviations about the mean are shown using blue shading for WACCM3, red dashed lines for WACCM4, and black vertical lines for satellite observations. The ground-based observations and satellite observations from SBUV and the Total Ozone Mapping Spectrometer (TOMS) are from *Randel and Wu* [2007]. WACCM3 and WACCM4 are in good agreement, with an increase in column O_3 between 2 and 3 DU per 100 units of $f10.7$. At most latitudes, the change in column O_3 from solar minimum to solar maximum is smaller in WACCM4 by less than 0.75 DU per 100 units of F10.7. In the
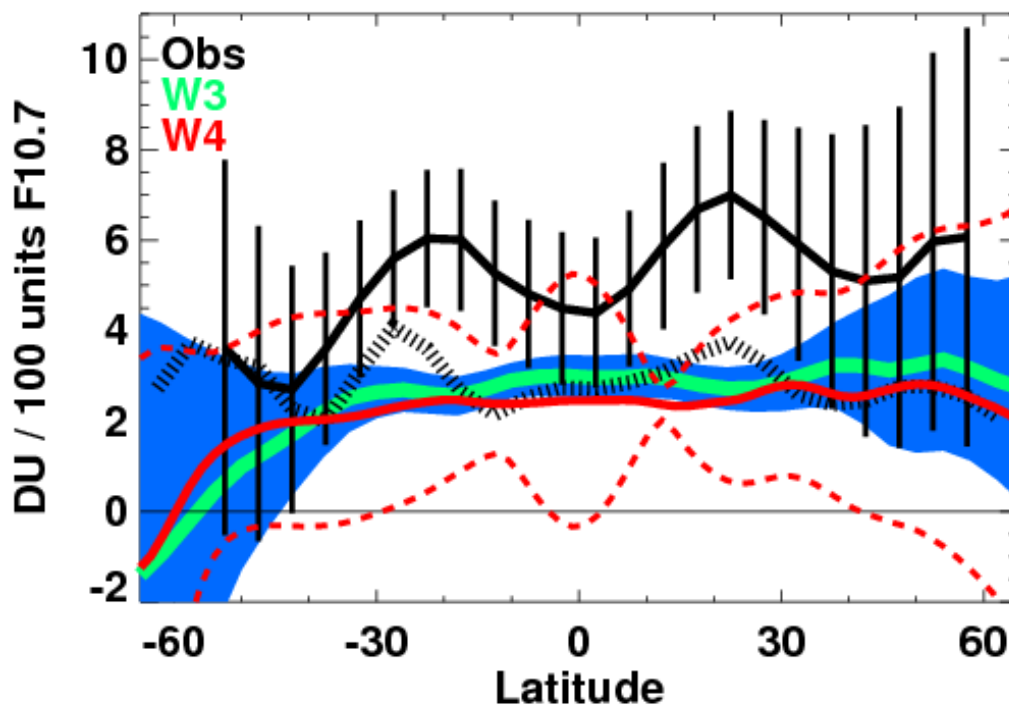
Figure 2.11: Multi-year annual mean zonal average ΔO_3 column per 100 units of 10.7 cm flux. The horizontal black line indicates zero change. The solid green line and solid blue shading are WACCM3 means and 2-sigma variability, respectively. The red solid and dashed lines are WACCM4 means and 2-sigma variability, respectively. The solid black line with vertical lines is combined satellite data means with 2-sigma error bars from *Randel and Wu* [2007]. The black dashed line is means from ground-based data from *Randel and Wu* [2007].

Antarctic poleward of 60° S, both WACCM3 and WACCM4 show a decrease in column O_3 of more than 1 DU per 100 units of f10.7. WACCM4 shows consistently higher variability than WACCM3, and this amount of variability is consistent with the satellite observations. Satellite observations generally indicate that solar cycle-induced O_3 differences are 50% to 100% larger than in the model. The ground-based observations fall directly between the WACCM3 and WACCM4 averages near the equator, but do not corroborate the column O_3 loss in the Antarctic. Given the disagreement between the ground-based and the satellite observations, we conclude that both WACCM3 and WACCM4 give a reasonable change in column O_3 with the solar cycle, except possibly in the SH polar region. As discussed by M07, a large source of uncertainty in the satellite data is the lack of observations, with only 3 full solar cycles being included at most.

Figure 2.12 shows the multi-year, annual average zonal mean ΔT for WACCM3 (a) and WACCM4 (b). As expected, both model versions show 1-4 K increases in temperature at solar maximum in the upper mesosphere. In WACCM4 there are statistically significant temperature decreases of 0.5-1 K in the Antarctic stratosphere and in the equatorial lower mesosphere. These regions of lower temperature are also seen in WACCM3, but did not reach statistical significance. The decrease at the South Pole near 40 km in WACCM4 is consistent with the negative ΔO_3 in the SH polar upper stratosphere shown in Figure 2.8. The loss of O_3 means less absorption of solar radiation and thus an apparent cooling of the atmosphere [*Brasseur and Solomon*, 2005].

Figure 2.13 is analogous to Figure 2.12 but for ΔU. Both versions of WACCM show similar solar cycle effects, with positive ΔU (westerly shifts) at mid-to-high latitudes in the upper stratosphere and lower mesosphere. The regions of statistical significance are shifted latitudinally in WACCM4 vs. WACCM3, but the overall morphology of the response is quite similar in both
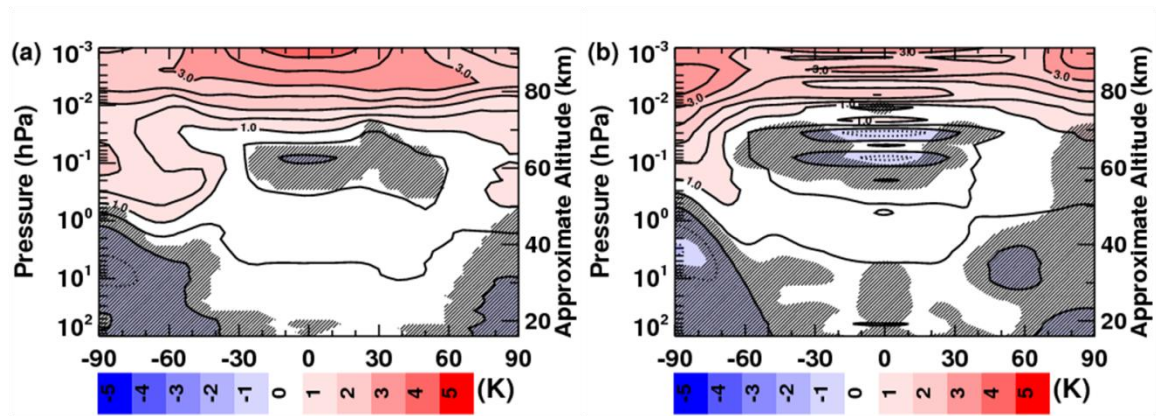
Figure 2.12: Same as Figure 7 but for ΔT. Black contours are every 0.5 K.
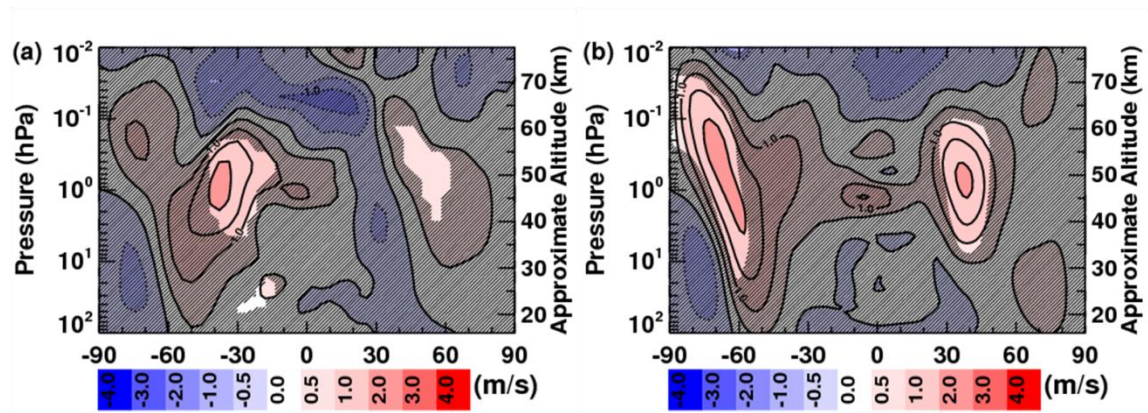
Figure 2.13: Same as Figure 7 but for ΔU. Black contours are every 0.5 m/s.

model versions. The changes in U are consistent with the simulated temperature changes. That is, both versions show increasing latitudinal gradients at solar maximum, which would lead to positive ΔU through thermal wind balance. In WACCM3, the SH positive ΔU is +2 m/s near 40°S and 1 hPa and the NH positive ΔU is +1 m/s near 55°N and 1 hPa. WACCM4 positive ΔU maxima of +2 m/s are centered near 70° S and 40° S and 1 hPa. When viewed as monthly averages (not shown), the SH positive ΔU in WACCM4 is strongest in September and October, while the NH positive ΔU is seen in February. The annual average ΔU in ERA-40 shows westerly maxima of 3-5 m/s near 30° S and 40° N and 50 km [*Frame and Gray*, 2010; see their figure 3]. It is interesting that WACCM3 captures the SH ΔU anomaly while WACCM4 adequately simulates the NH ΔU anomaly. As noted by M07, ERA-40 shows a stronger westerly shift in the NH than seen in WACCM3. In this respect, WACCM4 comes closer to replicating the ERA-40 solar cycle-induced ΔU in the NH. However, a likely culprit for the discrepancies between WACCM4 and ERA-40 in the SH stems from the "cold-pole" problem as described in *Marsh et al.* [2013]. The cold-pole causes an overly strong SH stratospheric polar jet (Figure 2.6c), which creates a stronger temperature gradient impact from EPP-NO$_x$ induced O$_3$ loss at the pole for a longer period of time.

2.5 Conclusions

This work presented the groundwork necessary to further examine solar cycle signals in the atmosphere using a new version of WACCM. Comparisons between WACCM3 and WACCM4 quantified changes due to the different model versions. Solar-cycle dependencies in WACCM4 were then compared to M07.

Several changes are seen between WACCM model versions without taking the solar cycle into account. Of particular note are the changes caused by the inclusion of a QBO, updated non-

orographic gravity wave parameterizations, and increased horizontal resolution. Differences between model versions of note are as follows:

- There is a stronger descending branch of the residual circulation in WACCM4; this leads to enhanced descent of NO_y produced by EPP, more O_3 loss in the polar upper stratosphere, and higher annual average temperatures in the Antarctic mesosphere.

- Inclusion of the QBO in WACCM4 caused the altitude of the tropical stratospheric O_3 maximum to increase by ~2 km, along with associated changes in temperature and zonal winds.

- Both model versions consistently underestimate Antarctic total column ozone over the course of the year. These total column O_3 deficiencies may be related to the "cold pole" problem in both versions of the model.

- The SH cold pole problem is exacerbated in WACCM4, and associated issues in vortex longevity remain an issue.

- WACCM4 zonal winds are more westerly than WACCM3 winds in the tropics throughout the entire stratosphere and mesosphere.

- The Antarctic polar night jet is stronger, shifted poleward, and extends to higher altitudes in WACCM4 than in WACCM3. The effect of this difference improves comparisons of vortex area with reanalysis data.

Solar cycle variations between model versions also yield interesting results as follows:

- Both models show increases in O_3 during solar maximum at low to mid latitudes that are associated with increased production from SSI, as expected.

- Increased NO_y descent from the mesosphere to the stratosphere during solar maximum results in more O_3 loss by the EPP indirect effect, particularly in the SH.

- Both model versions give reasonable results for solar cycle-induced changes in column O_3 at low to mid latitudes.

- During solar maximum, the Antarctic stratosphere is colder than during solar minimum; this strengthens meridional temperature gradients, reinforced by EPP induced O_3 loss, and leads to a 2 m/s westerly wind increase.

- WACCM4 zonal wind is in better agreement with ERA-40 results in the NH compared to WACCM3.

There are some caveats to the analysis presented above that should be noted. NO_x descent in WACCM from the thermosphere into the mesosphere is known to be too small [*Smith et al.,* 2011], suggesting that impacts from EPP-NO_x shown in this work might be underestimated. There is also no treatment of medium energy electrons or solar protons in the simulations presented here, which would contribute an additional source of EPP-NO_x in the mesosphere. The ocean in both versions of model simulations used here comes from prescribed sea surface temperatures, thus any modulation of the solar signal caused by the ocean is not seen.

Chapter 3

POES MEPED differential flux retrievals and electron channel contamination correction

This chapter includes the contents of *Peck et al.* [submitted, 2014b]. The goal of the work in this chapter is to develop a correction method to remove proton contamination in electron channels reported by the Polar-orbiting Operational Environmental Satellites (POES) Medium Energy Proton/Electron Detector (MEPED).

The main results of this work are: (1) A correction method was successfully developed to remove proton contamination in the electron channels reported by MEPED and differential fluxes were calculated for protons and electrons between 25 keV and 10 MeV; (2) a new relativistic electron channel was produced; and (3) corrected MEPED output match data from the Detection of Electro-Magnetic Emissions Transmitted from Earthquake Regions (DEMETER) Instrument for Detecting Particles (IDP).

3.1 Introduction

Energetic particle precipitation (EPP) is known to have a profound impact on nitrogen oxide (NO) [*Rusch et al.*, 1981] and hydroxyl (OH) [*Solomon et al.*, 1981; 1983] production in the stratosphere, mesosphere, and thermosphere. The altitude of production depends on the type and energy of the precipitating particle; larger particles with higher energies penetrate deeper into the atmosphere [e.g., *Jackman*, 1980; *Roble and Ridley*, 1987; *Fang et al.*, 2008; 2010; *Thorne*, 1980]. The NO_x ($NO_x = NO + NO_2 + N$) catalytic cycle is the primary loss mechanism for ozone (O_3) in the stratosphere above about 24 km [e.g., *Garcia and Solomon*, 1994], while the HO_x ($OH + HO_2 + H$) catalytic cycle is prevalent in the mesosphere [*Nicolet,* 1975].

Quantifying natural variations in EPP-produced NO_x (EPP-NO_x) and HO_x (EPP-HO_x) and subsequent O_3 destruction is critical to understanding climate effects in the middle atmosphere. Therefore, it is vital that all relevant sources of EPP be considered.

It has long been theorized that Medium Energy Electron (MEE; ~20 keV to 1 MeV) precipitation and relativistic electron precipitation (REP; >1 MeV) might significantly affect the middle atmosphere [*Baker et al.*, 1987]. *Callis et al.* [1991] showed globally integrated increases of EPP-NO_y from MEE and REP of 35-40% from 1979 to 1985 using atmospheric measurements combined with 2D model calculations. *Callis et al.* [1998a, 1998b, 2001] used data from the Polar-orbiting Operational Environmental Satellite (POES) Space Environment Monitor version 1 (SEM-1) Medium Energy Proton and Electron Detector (MEPED) and from atmospheric sounders to quantify possible impacts from MEE and REP. Large (>20%) increases that were attributed to EPP-NO_x were observed in stratospheric NO_y near 25 km [*Callis et al.*, 1998a]. Calculations with a 2D transport model using particle input showed an EPP-induced column increase in NO_y from 25-40 km of ~12% [*Callis et al.*, 1998b]. Impacts from MEE and REP are significantly higher in the upper stratosphere above 25 km [*Callis et al.*, 2001]. *Randall et al*. [2001] suggested that EPP-NO_x produced by MEEs led to large stratospheric NO_x enhancements observed at high southern latitudes in September-October 2000, although these enhancements are also consistent with EPP-NO_x production by solar protons [*Jackman et al.*, 2008]. *Randall et al*. [2007] showed that EPP-NO_x comprises up to 10% of stratospheric NO_y globally, and 40% in the polar regions. They further showed that the EPP Indirect Effect – the production of EPP-NO_x in the mesosphere or lower thermosphere followed by descent to the stratosphere – correlated with both auroral electron and MEE hemispheric power; but they were unable to distinguish between these two sources.

Codrescu et al. [1997] used data from the SEM-1 MEPED instruments to specify MEE-induced ionization in the Thermosphere-Ionosphere-Mesosphere-Electrodynamic General Circulation Model (TIME-GCM). They calculated a 13% increase in HO_x at 78 km near 75°N in January, and an associated 25% decrease in O_3 at the same location. The MEPED data used by *Codrescu et al.* [1997], however, is known to have proton contamination of the electron data channels [*Evans and Greer*, 2000; hereafter referred to as *EG00*]. Beginning with the launch of NOAA-15, a newer version of the MEPED instrument was used as part of the SEM version 2 (SEM-2) and has been launched on seven satellites (NOAA-15, -16, -17, -18, -19, and MetOp-02 (A) and -01 (B)). Details of SEM-2 can be found in *EG00*. The SEM-2 MEPED instrument suffers from the same problems as the SEM-1 MEPED, including cross contamination between electron and proton detectors [*Rodger et al.*, 2010a].

There have been several studies that attempted to remove proton contamination from the electron channels in SEM-2 MEPED. One way to remove proton contamination is to produce a differential flux spectrum (e.g., counts sec^{-1} cm^{-2} sr^{-1} keV^{-1}) for protons and then calculate the total contamination that would be observed by the electron channels. *Lam et al.* [2010] assumed a series of exponential functions to fit a proton differential flux spectrum and combined it with the bow-tie method [e.g., *Selesnick and Blake*, 2000] to calculate the total contamination in the electron channels. *Yando et al.* [2011; hereafter referred to as *Y11*] quantified the gathering power for each channel in the SEM-2 MEPED telescopes by simulating the instrument in a field of known particle fluxes and analyzing the response of each channel. *Y11* provided details about the electron detectors' response to protons, allowing a better estimate of proton contamination. The *Y11* gathering powers were experimentally confirmed by *Whittaker et al.* [submitted, 2014], who also showed that the *Lam et al.* [2010] approach for proton contamination correction was

effective. However, *Y11* does not provide a proton differential flux spectrum; their results can only be used to calculate contamination if provided with a flux spectrum. *Asikainen and Mursula et al.* [2013] assumed a series of power law spectra to construct a proton differential flux spectrum and applied the response functions from *Y11* to calculate contamination in the electron channels. Neither *Lam et al.* [2010] nor *Asikainen and Mursala* [2013] assessed the error incurred in their calculations by assuming the exponential or power law functional forms, respectively, for the differential flux spectrum; nor did *Codrescu et al.* [1997], who assumed a Maxwellian. In this work we calculate proton and electron differential flux spectra from the SEM-2 MEPED data for each measurement without assuming a single type of spectral function. The resulting spectra have reduced proton contamination, and are accompanied by error bars that account for satellite measurement errors and errors in fitting the spectral distribution. We test the resulting spectra against independent satellite measurements to confirm the validity of our approach. The results of this work provide the necessary data source for accurately modeling the impacts of MEE on the middle atmosphere in future work.

Given the issue of proton contamination noted above, and the fact that the MEPED instruments have sparse coverage in magnetic local time (MLT), there have been several recent attempts to quantify the impacts of MEE indirectly. *Verronen et al.* [2011] and *Andersson et al.* [2012] suggested that mesospheric nighttime OH concentrations could be used as a proxy for MEE precipitation. *Verronen et al.* [2011] based their conclusion on the observation that MEPED 100-300 keV electron count rates and nighttime OH concentrations from 71-78 km and 55°-65° magnetic latitude from the Aura Microwave Limb Sounder (MLS) were highly correlated during March 2005 and April 2006. They found that 56–87% of the OH variation could be explained by EEP. The correlation was weakened by variations in the transport of water

vapor, since photolysis of water vapor will perturb the background levels of OH. Similar results were found by *Andersson et al.* [2012], which covered the time period from 2004-2009. Enhanced electron precipitation linked to increased mesospheric OH concentrations has also been correlated with mesospheric ozone depletion [*Andersson et al.*, 2014b]. Another important result was that the MEPED electron channels have high count rates in the South Atlantic Anomaly (SAA) with no correlations to mesospheric OH in the same region [*Andersson et al.*, 2014a], probably due in part to proton contamination. Therefore, although electron precipitation has been observed in the SAA using other methods [e.g., *Pinto and Gonzalez*, 1989], caution is needed when dealing with MEPED data in the SAA.

Another attempt to create a dataset of MEE precipitation and resulting ionization rates that could be used in models is the Atmospheric Ionization Module Osnabruck (AIMOS) model [*Wissing and Kallenrode*, 2009]. AIMOS calculates an electron differential flux spectrum using multiple power law fits to MEPED particle channels. Hemispheric maps of particle flux are produced using statistical correlations between geomagnetic index (Kp) particle fluxes. Unfortunately, the AIMOS model cannot account for errors in the raw MEPED data upon which it is based. In addition, the K_p parameterization introduces errors since MEE will have a time delayed acceleration after a solar storm beyond what is expected by geomagnetic index [*Rodger et al.*, 2010a]. This would only impact fluxes on the short time scales that immediately follow a SPE and would not have large impacts on longer time scales.

Section 3.2 presents the POES SEM-2 MEPED instrument, including issues that currently exist in the data. Section 3.3 describes the correction method developed to remove proton contamination from the electron channels, and to calculate differential flux spectra for both protons and electrons, along with measurement and correction errors. Section 3.4 shows

results based on the corrected MEPED data along with some comparisons of the corrected data to an independent satellite dataset. Section 3.5 gives conclusions and outlines topics of future work.

3.2 POES MEPED Instrument

The POES MEPED instrument used in this work is part of SEM-2, and is described in *EG00* and *Green* [2013]. The MEPED instrument has two proton telescopes and two electron telescopes. One telescope of each particle type is grouped as the 0° detectors and another set is grouped as the 90° detectors. In reality, on POES the 0° detectors are rotated 9° away from zenith (0°) and the 90° detectors are rotated 9° away from the anti-ram direction [*EG00*, figure 2.1.1]. This rotation of the detectors permits a clear field of view for the telescopes. The 0° detectors generally sample a portion of the precipitating energetic particles in the BLC (see Figure A3 of *Rodger et al.* [2010b]). The 90° detectors sample a mix of trapped or precipitating energetic particles depending on their location.

Table 3.1 shows the nominal ranges of energies detected by the proton and electron detectors and the channels to which those ranges correspond. The proton telescopes have six energy channels, P1-P6. The electron telescopes have 3 energy channels, E1-E3. Channels P6, E1, E2, and E3 are integral channels; channels P1 through P5 are differential energy channels that measure within a limited energy range. The nominal effective maximum measurement energy for the electron channels is 2.5MeV, while the maximum measurement energy for proton channel P6 is over 200MeV. Note that *Y11* has demonstrated the actual energy ranges differ from these nominal values.

The MEPED count rates (counts/sec) used in this study are reported in 16-second intervals, which corresponds to about 100 km along the satellite track, or approximately 1° of

Energy Channel	Proton Response Nominal Range (keV)	Electron Response Nominal Range (keV)
P1	30-80	
P2	80-250	
P3	250-800	
P4	800-2500	
P5	2500-6900	
P6	>6900	
E1	-	>30
E2	-	>100
E3	-	>300

Table 1: MEPED energy channels and nominal responses to electrons and protons.

geographic latitude at mid-latitudes. The raw data is sampled every other second with a one second integration period [*EG00*] and averaged together to create the 16-second data. A description of the 16-second data can be found in Section 3 of *Codrescu et al.* [1997]. If only one count is identified in an energy channel in a single two-second measurement (one second of measuring by the 90° telescope and one second of measuring by the 0° telescope), this would be reported as one count per second for two seconds. Therefore the minimum non-zero value that can be reported in the 16-second data is two counts per 16 seconds (assuming zero counts are identified in the remaining seven measurements), or 0.125 counts/sec.

There are a number of known issues in the data currently reported by the MEPED instrument. The first issue is the deterioration of the proton telescopes by radiation damage. According to *EG00*, this impact becomes significant after 2-3 years of operation and the effect of this deterioration is to raise the energy thresholds required to register a particle in the telescope. An attempt at fixing this proton channel degradation was shown in *Asikainen et al.* [2012] but is not included in the correction method described in Section 3.3 below. In order to assess the proton degradation *Asikainen et al*. [2012] compared measurements when different satellites were in close proximity. This is a reasonable first attempt at assessing potential instrument changes. However, the method is prone to errors because the coincidences are infrequent and only occur at high latitudes where counting statistics are poor. The method also does not account for other circumstances that may affect the measured fluxes such as differences in the pointing direction of the telescopes and the altitude of the satellite. Some studies are underway that statistically compare the satellite measurements over long time periods and give a more reliable estimate of any instrument variation or degradation, but quantitative results are not yet available

[*Sandanger et al.*, 2014]. In order to properly validate the impact of the correction applied in this work we do not include a proton degradation correction.

A second known issue with the reported MEPED data is cross-contamination between the proton and electron telescopes. Details on the magnitude of contamination in the nine reported energy channels (P1-P6, and E1-E3) can be found in *Y11*. For the proton detectors, the greatest medium energy electron contamination occurs in channel P1, and decreases at higher energy channels. Channel P5 is the only "pure" channel reported by MEPED, reading only protons and no electrons. Channel P6 has large contamination from relativistic electrons. *Y11* shows that the P6 channel could be used to report quantitative values of relativistic electron precipitation (REP), but this has previously only been used qualitatively [*Miyoshi et al.* 2008; *Evans et al.,* 2008; *Horne et al.* 2009, *Sandanger et al.* 2009; *Millan et al.* 2010; and *Rodger et al.* 2010a]. Protons also contaminate the electron energy channels, E1-E3. Channel E3 is only contaminated by protons with energies exceeding 400keV, while channels E1 and E2 are contaminated by protons with energies exceeding 100keV. Since the contamination of each electron channel varies, the contamination cannot be subtracted out by subtracting one channel from another. The proton contamination in the electron channels E1-E3 is larger than the electron contamination in the proton channels P1-P5. *Y11* (their Appendix B) tabulates the contamination values. The goals of this work are to calculate a correction for proton contamination of the MEPED E1-E3 electron channels, determine relativistic electron count rates to produce a virtual fourth electron channel (E4, 300 keV – 2.5 MeV with a center energy at ~800 keV), use E1-E4 count rates to calculate continuous spectra over the energy range from 25 keV to 10 MeV, and provide realistic error estimates for these spectra.

Note that MEPED also includes Omni-Directional detectors that detect higher energy protons (*EG00*). These detectors were not modeled by *Y11*. Given the different design of the Omni-Directional detectors, it is difficult to quantify the impacts from high energy protons on the MEPED detectors. Any high energy proton contamination that would be detected by the omni-directional detectors is not taken into account in the correction method that follows since this method only uses protons reported by the P1-P6 channels.

3.3) Proton Contamination Correction

The correction described here is based on the inversion method in *O'Brien and Morley* [2011] and uses weighting functions from *Y11*. The process of removing proton contamination from the electron channels has three main steps. Step one is to convert data from the proton channels into a proton differential flux spectrum using the inversion method. The second step is to use a forward model to calculate the total proton contamination in the electron channels. In step three the corrected electron channels are put through the inversion method to get the electron differential flux spectrum.

The details and mathematics of the inversion method can be found in Appendix A. The inversion method produces a best fit spectrum, $\vec{f}(E)$, which solves the equation:

$$\vec{y} \approx \vec{\lambda} = \delta t \int_0^\infty \vec{G}(E)\vec{f}(E)dE \tag{3.1}$$

Here $\vec{y}$ is a vector of measured counts (16-second data in counts per second multiplied by 16 seconds) and $\vec{\lambda}$ is a vector of expected counts from a forward model of the inversion, both with length N_y, the number of channels to be included in the inversion. $\vec{G}$ is a vector of response functions for the instrument channels as a function of energy, E, taken here from *Y11* (their appendix B), and $\vec{f}$ is the differential flux (counts sec^{-1} cm^{-2} sr^{-1} keV^{-1}). δt is the integration time of the instrument data. For this work, the 16 second data was used, and thus $\delta t = 16$ seconds.

Equation 3.1 is a simple inversion problem, where $\vec{f}(E)$ is unknown. In discrete form, there are many more unknowns in $\vec{f}(E)$ than equations, where the number of equations is equal to N_y. The forward model in this case is simply calculating $\vec{\lambda}$ by solving Equation 3.1 using calculated differential flux, $\vec{f}(E)$.

The first step in removing the proton contamination from electrons is to calculate the proton differential flux spectrum. The inversion method described in Appendix A is applied to 5 proton channels, P1-P5, with the assumption of little to no electron contamination. This assumption is not entirely valid in the lower energy proton channels, P1-P4, but the magnitude of the electron contamination compared to proton counts is small compared to the proton contamination of electron channels [*Y11*]. Channel P5 is the only "pure" MEPED channel that has no electron contamination and only detects protons. P6 is left out of the proton inversion since it is highly contaminated by relativistic electrons [*Y11*]. The goal of the inversion method is to minimize the residual of $\vec{y}$ and $\vec{\lambda}$.

The inversion problem described by Equation 3.1 is unconstrained and needs to be constrained by a possible spectral shape. A spectral shape is calculated by fitting the measurements to a function that combines weighted spectra for energy exponential (EE), power law (PL), single relativistic Maxwellian (RM), and double relativistic Maxwellian (DM) distributions. A graphical example of what these spectra look like alone and when combined can be seen in Figure 3.1, which shows a representative proton differential flux spectrum for L-Shell 6.15 on 13 May 2003 using data from the NOAA-15 MEPED 0° detector. This particular date and location were chosen arbitrarily simply to demonstrate the inversion method. In Figure 3.1a, the solid line with 1-sigma error bars (labeled "combined") is the final calculated differential flux spectrum, while the dashed and/or dotted lines are the best fits of the PL, EE, RM, and DM
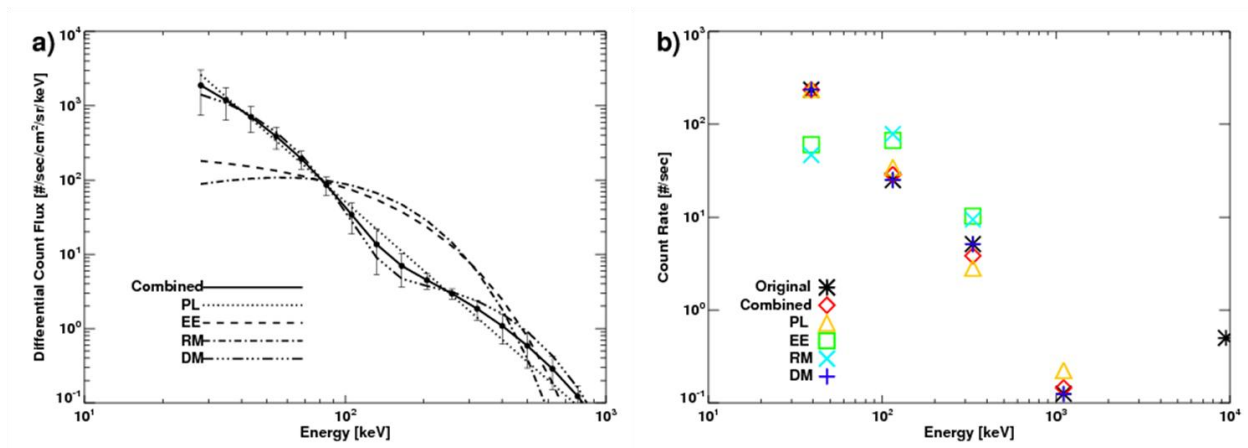
Figure 3.1: (a) Differential flux of medium energy protons (black solid line), along with the best fit spectra for PL, EE, RM, and DM in counts/sec/cm^2/sr/keV. Two sigma standard error of the combined flux spectrum is denoted by vertical bars. (b) Original and calculated channel count rates (counts/sec) using spectra from (a). Channels are marked at their estimated measurement center energies as opposed to nominal energies. Data is taken at an L-Shell value of 6.15 from NOAA-15 0° detector on 13 May 2003.

spectra. The error bars include estimates of the contributions from errors in instrument measurement and spectral shape. Figure 3.1b compares the original proton channel measurements to the results of running a forward model using each spectrum from Figure 1a. Symbols are placed at the estimated measurement center energy for each channel. In this case the proton measurements are fit best with either the combination best fit spectrum or the DM spectrum, not a PL or EE spectrum as is often assumed [e.g., *Asikainen and Mursula et al.*, 2013; *Lam et al.*, 2010]. The combined or DM spectra are generally the best fits among all measurements in 2003 and 2004 (not shown). A forward model is used on the combined best fit spectrum with weighting functions from *Y11* to calculate the proton count contamination in the measured electron counts for each electron channel. The proton contamination is then subtracted from the electron channels, E1-E3, to get uncontaminated electron counts.

A further calculation is also done to create a virtual relativistic electron channel, E4. Since P6 was not included in the calculation of a best proton differential flux spectrum, a forward model can be applied to the proton differential flux to calculate the expected proton counts in the P6 channel. This calculated or "corrected" P6 channel is then subtracted from the original P6 channel. The residual is believed to be the relativistic electron contamination of the P6 channel and is called the E4 channel. The E4 channel acts as an integral channel similar to E3 with a lower energy boundary around 300 keV, but is believed to have a center energy at around 879 keV. As a result the E4 channel is more sensitive to relativistic electrons (> 1 MeV) than the E3 channel. The E4 channel will detect some electrons below 1 MeV and can be compared to gathering power provided by *Y11* for the P6 channel detection of electrons (their Table B2). Therefore, the E4 channel is not a "pure" relativistic electron channel, but does primarily measure > 1 MeV electrons.

Using all the electron channels, E1-E4, an electron differential flux spectrum is calculated

a manner similar to that applied to the proton measurements (e.g., by constrained inversion using

a best fit spectrum). Figure 3.2 shows the best electron spectral fits (a) and the same fits run

through a forward model along with the original and corrected electron channel outputs (b). This

plot is comparable to that seen in Figure 3.1, except the electron channels in Figure 3.2b are all

integral channels. The error bars in the combined spectrum in Figure 3.2a include errors in

instrument electron measurement and spectral shape; they do not account for errors in the

estimate of proton contamination. The best electron differential flux spectrum shown is a

combination of all four spectra or the DM. The combined or DM spectra are generally the best

fits among all measurements in 2003 and 2004 (not shown). This complete differential flux

spectrum can be used by models to provide accurate ionization rates for investigations of the

impacts of MEE and REP on the middle atmosphere.

3.4 Results and Validation

Figure 3.3 shows the NOAA-17 MEPED 0° detector E3 channel for the original (a) and

corrected (b) satellite measurements on the universal time day 29 October 2003 in geographic

coordinates. Black measurements are ones where the proton contamination signal was on the

same order of magnitude as the original MEE signal (e.g., signal to noise ratio less than or equal

to one) and thus no useful electron data could be extracted. During this day a SPE was occurring.

Contamination from high energy protons, greater than detected by the P6 channel, shows up as

fluxes covering the entire magnetic polar cap (poleward of ~60°N and ~60°S in geographic

space). While the correction was able to improve measurements of the radiation belts (areas of
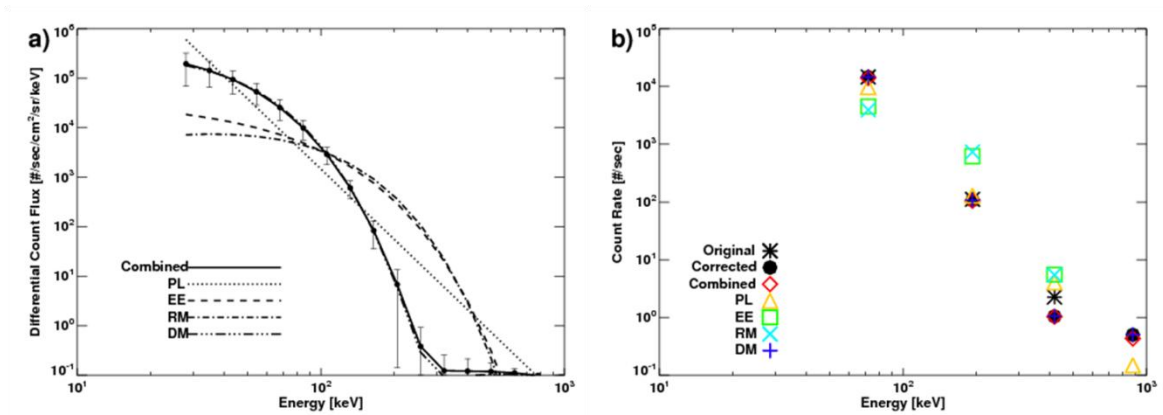
Figure 3.2: (a) Differential flux of medium energy electrons (black solid line), along with the best fit spectra for PL, EE, RM, and DM in counts/sec/cm^2/sr/keV. Two sigma standard error of the combined flux spectrum is denoted by vertical bars. (b) Original, corrected, and calculated integral channel count rates (counts/sec) using spectra from (a). Channels are marked at their estimated measurement center energies as opposed to nominal energies. Data is taken at an L-Shell value of 6.15 from NOAA-15 0° detector on 13 May 2003.
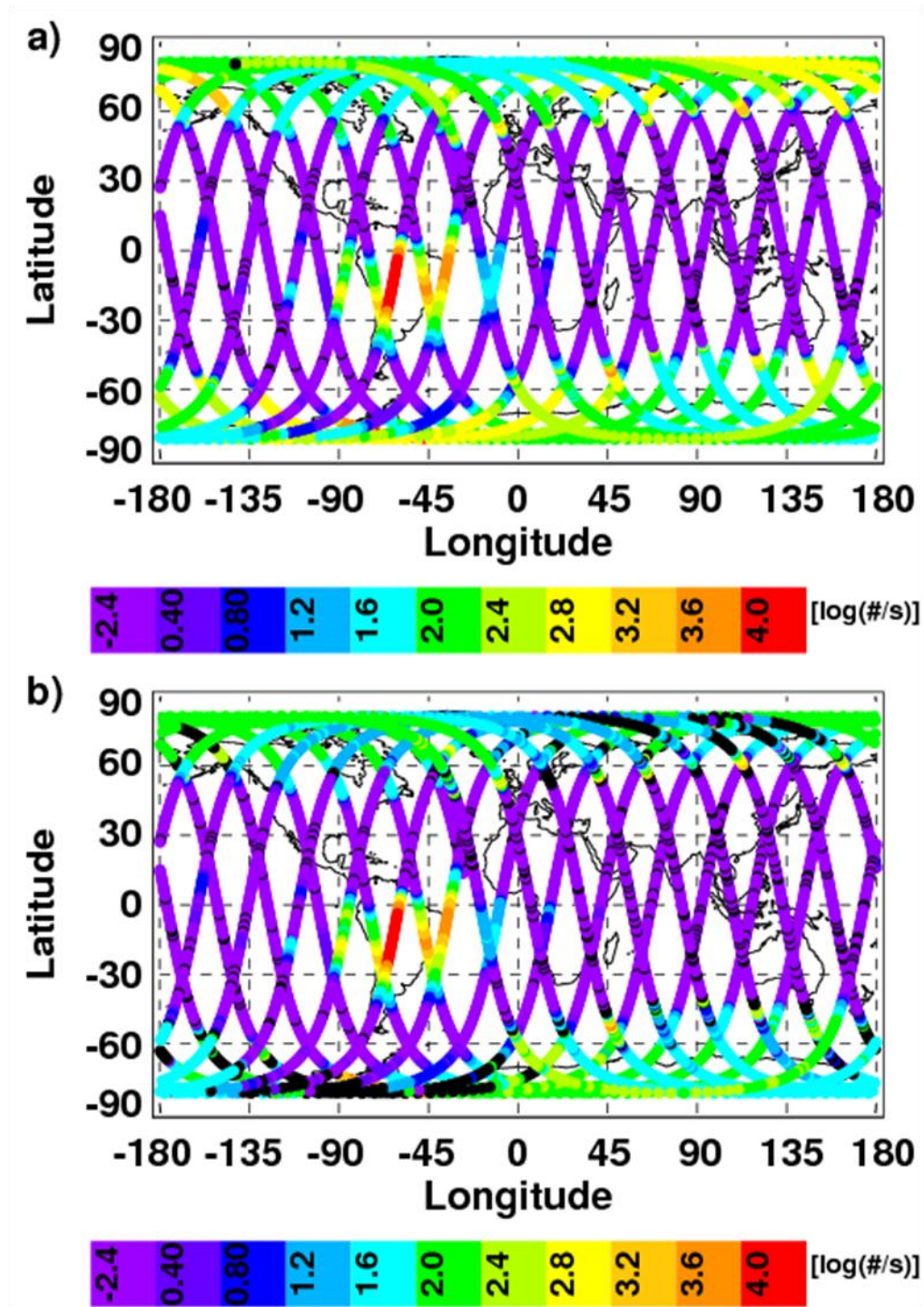
Figure 3.3: NOAA-17 MEPED 0° detector E3 channel (>300 keV) during a SPE on 29 October 2003 with original values (a) and corrected values (b). Black measurements denote measurements with too much contamination to extract a corrected signal. Points in the SAA are likely also invalid due to high energy proton contamination that is not accounted for in the correction method.

maximum electron precipitation), the high energy proton contamination over the magnetic pole could not be removed. This type of contamination only occurs during a large SPE; it is due to very high energy protons that pass through the instrument from all directions and not just the instrument opening. The contamination is extremely difficult to quantify and remove because it would require a complete model of the entire POES/MetOp satellite and its interaction with energetic protons. Such a model is not available; thus, this type of contamination is not accurately removed with the current method. Another region of high energy proton contamination also occurs over the SAA (centered at ~70°W and ~15°S). This region is a zone of weak magnetic field strength where enhanced particle precipitation from the inner radiation belt is believed to occur [Pinto and Gonzalez, 1989]. *Andersson et al*. [2014a] has shown that no atmospheric ionization (estimated using mesospheric nighttime OH concentrations) is correlated with enhanced MEPED electron channel count rates in the SAA. Therefore the MEE precipitation shown in the SAA by Figure 3 is likely an artifact of the measurement.

Figures 3.4 through 3.6 show the mean daily POES MEPED 0° detector electron channels in L-shell bins with a 0.1 value width for the uncorrected data (Figure 3.4), corrected data (Figure 3.5), and ratio of uncorrected to corrected data (Figure 3.6) for 1 January 2003 through 1 January 2005 in the Southern Hemisphere (SH). Where the ratio in Figure 3.6 is high, the data correction had the largest impact. These times coincide with SPEs, the most prominent of which in the timeframe shown is the "Halloween Storm" at the end of October 2003. Fluxes over 1000 electrons per second are seen at all L-shells greater than 4 for all electron channels in both the uncorrected (Figure 3.4) and corrected (Figure 3.5) data sets. MEE should be mostly confined to the radiation belts, and thus the electron signal should decline at L-shell values above eight. Since this is not the case, despite the correction method making a large change to the
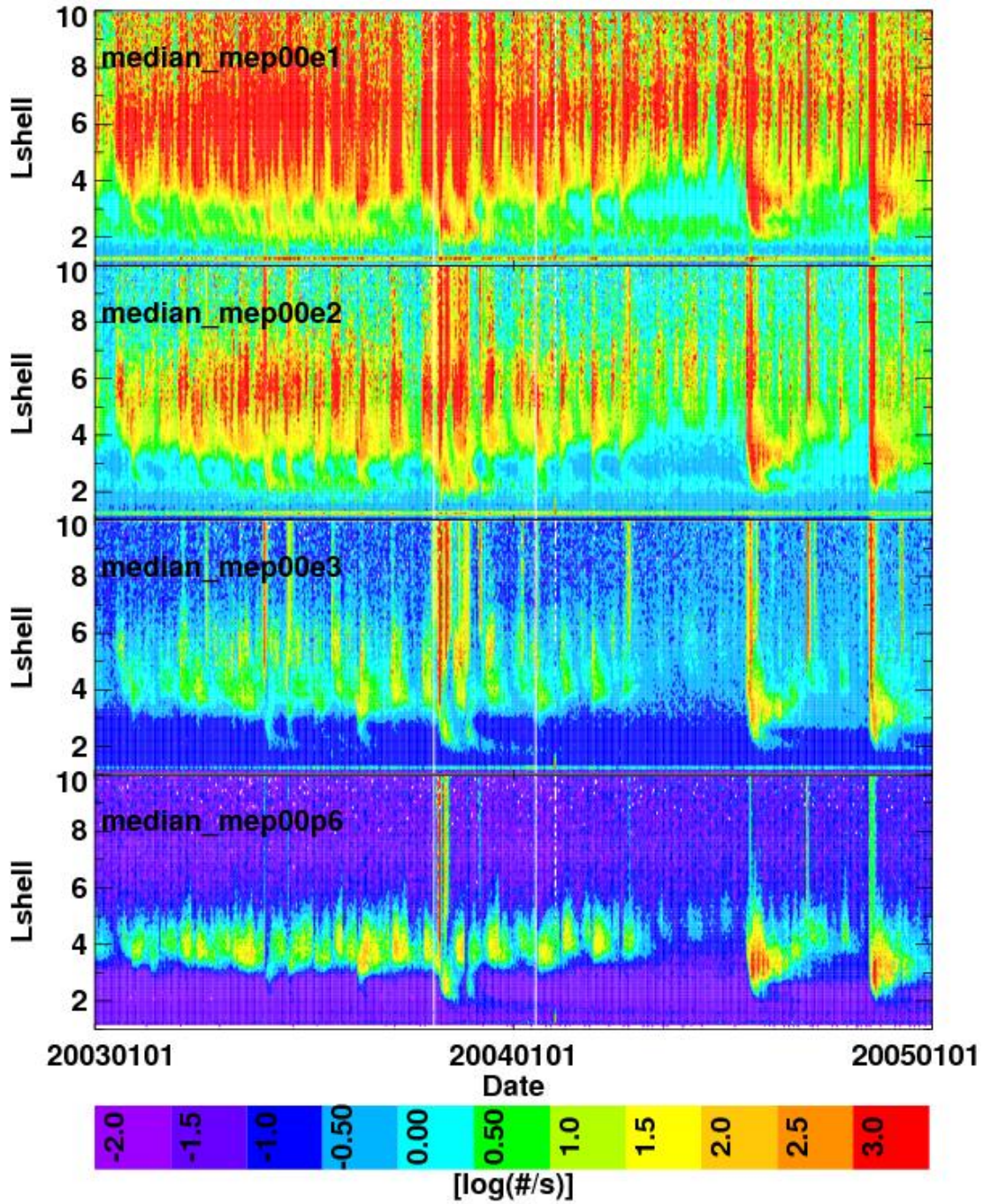
Figure 3.4: Daily average SH original MEPED 0° detector integrated flux channels E1, E2, E3, and P6 in L-shell and time for 1 January 2003 through 1 January 2005 measured in counts/second.
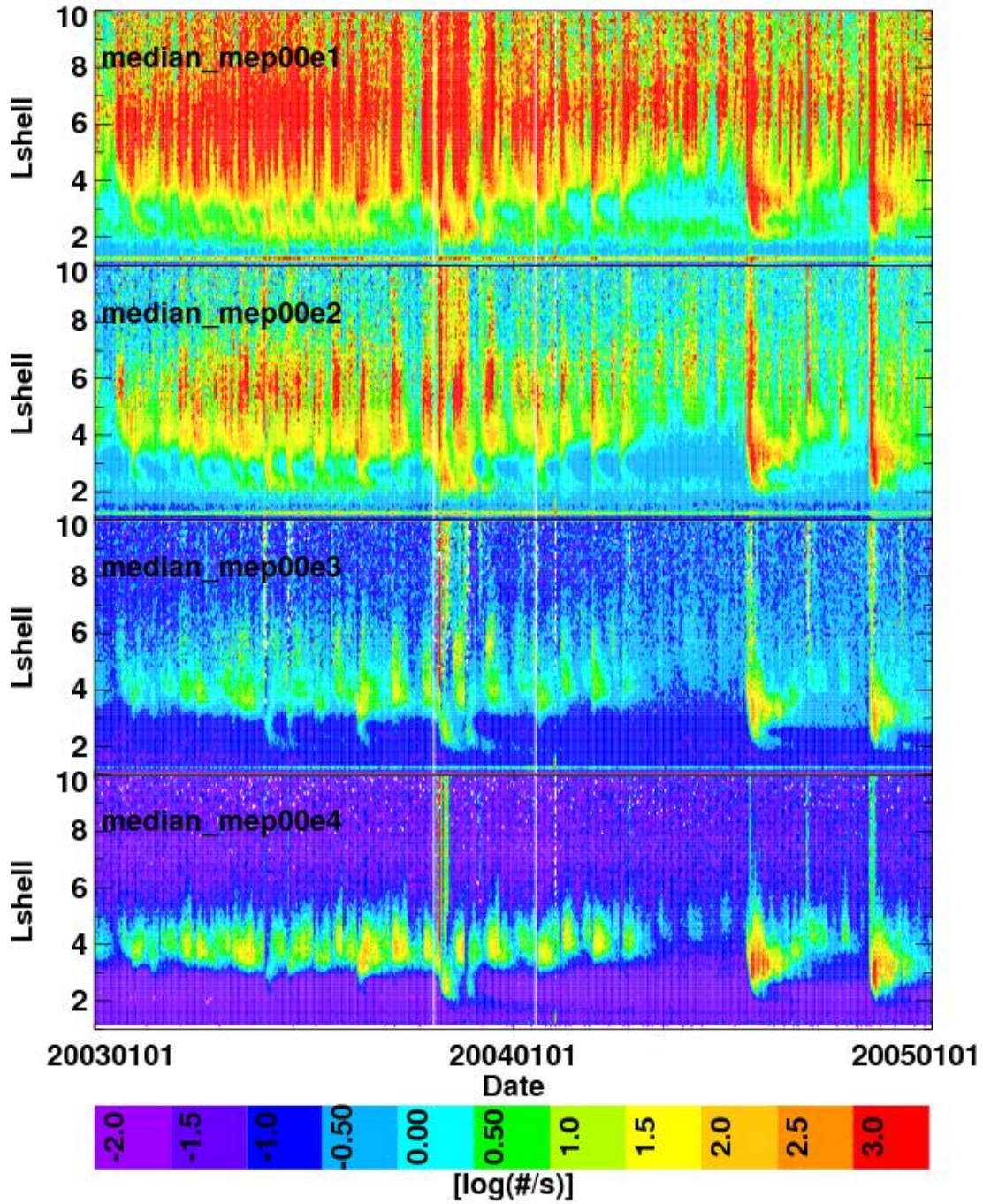
Figure 3.5: Same as Figure 3.4 but for corrected MEPED 0° detector integrated flux channels E1, E2, E3, and E4.
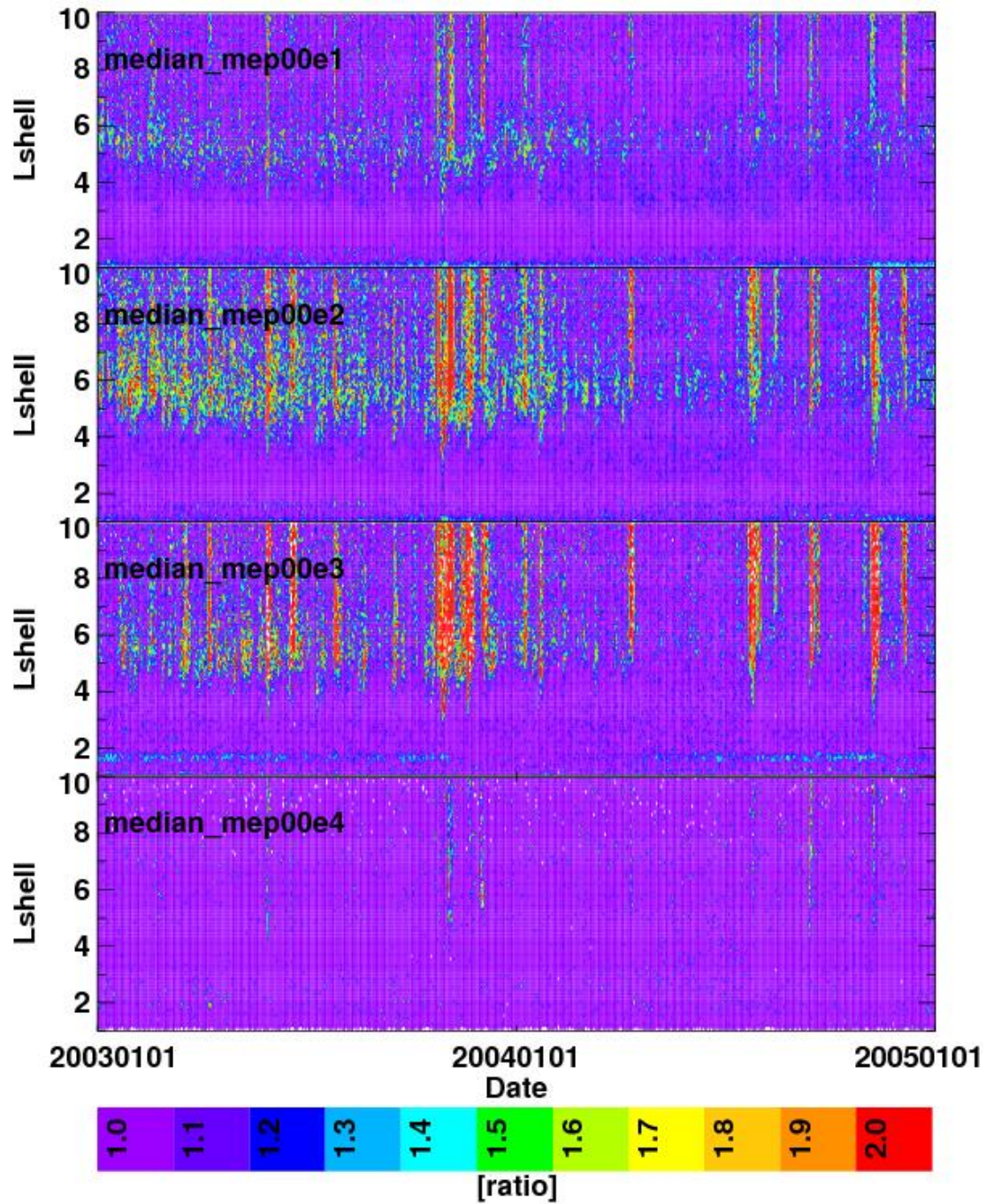
Figure 3.6: Ratio of Figure 3.4 to Figure 3.5, original E1, E2, E3, and P6 divided by corrected E1, E2, E3, and E4.

electron data during the late October 2003 storm, the electron channel correction method was incapable of removing all proton contamination. This is caused by the continued contamination present from high energy protons above the detection of the P6 channel as described in the correction method above.

Enhanced MEE count rates are detected in both the original (Figure 3.4) and corrected (Figure 3.5) datasets following solar storms and are not completely removed by the correction method. This is in agreement with other studies [e.g., *Rodger et al.*, 2010a], where radiation belt electrons are accelerated with a time delay from the arrival of a solar storm. The presence of MEE population levels seen in the 0° detector suggests that following a coronal mass ejection (CME) such as that in October 2003, enhanced MEE precipitation can continue to ionize the atmosphere and create NO_x and HO_x in the mesosphere and above. The culmination of this production in the days to weeks following a solar storm could be large, though exactly how large is not known, and is deserving of further study. Approximately 27-day periodic increases in MEE are also apparent in the original (Figure 3.4) and corrected (Figure 3.5) datasets. This type of periodic signal was reported by *Blake et al.* [1997] and is likely caused by periodic solar-wind changes related to the Sun's rotation bringing high-speed solar wind streams from coronal holes into an Earth affecting position. This phenomenon was also reported by *Rodger et al.* [2010a].

Next we compare MEPED data to electron spectra from the Detection of Electro-Magnetic Emissions Transmitted from Earthquake Regions (DEMETER) satellite Instrument for Detecting Particles (IDP) [*Sauvaud et al.,* 2006]. DEMETER was launched in June 2004 and flies at an altitude of 670 km in a Sun-synchronous orbit. The IDP is chosen as a comparison measurement due to its higher energy resolution and larger geometrical factor when compared with MEPED. IDP data used here represent the trapped electron population in 128 energy bins spanning 72 keV

to 2.3 MeV with bin widths of 17.9 keV. The first and last channels are integral channels measuring all particles less than or more than the specified range, and are thus not used in this work due to difficulties in creating a spectral fit from them [*Whittaker et al.*, 2013]. The IDP is susceptible to contamination by 0.52–2.95 MeV protons [*Sauvaud et al*., 2013] and therefore the comparisons shown below avoid regions of intense proton fluxes, for example the SAA.

The MEPED comparisons to IDP shown here use the MetOp-02 MEPED data. Only the 90° detectors on MEPED are considered in order to match the IDP viewing direction. Since there are no significant differences between the MEPED 0° and 90° detectors [e.g., EG00; *Y11*], comparison results for the 90° detector pertain to the 0° detector as well. Coincident measurements between MEPED and IDP are defined using the same criteria as *Whittaker et al.* [submitted, 2014]. These criteria are:

- Only measurements above an L-Shell value of 2.5 are considered.

- The absolute difference in time between instrument measurements is less than or equal to 10 minutes.

- The absolute difference in longitude between instrument measurements is less than or equal to 3°.

- The absolute difference in L-Shell values between instrument measurements is less than or equal to 0.5.

In this work, when more than one IDP measurement meets the conditions above with a given MEPED measurement, only the closest coincident IDP measurement in L-Shell value is used. This differs from *Whittaker et al.* [submitted, 2014], which used all coincident measurements. This results in 1862 coincidences between MetOp-02 MEPED and DEMETER IDP during the year 2009.

Figure 3.7 shows the SH mean coincident electron spectra between L-shell values of 6.0 and 6.25 from IDP (red) and corrected MEPED (black) with dashed red lines and black vertical bars representing one standard mean error in IDP and MEPED respectively. MEPED has the same general shape as the spectrum from IDP, suggesting that the correction method described above is properly modeling the shape of the electron spectrum. MEPED corrected electron differential flux values are on average about twice as large as IDP between 100 keV and 1 MeV. Given a change in magnetic field strength between MetOp-02 (~850 km) and DEMETER (~600 km) altitudes, particle fluxes would be expected to decrease by a factor of ~1.1 using an inverse cubed estimate of magnetic field strength with distance. The approximate factor of two difference between MEPED and IDP is consistent with results from *Whittaker et al.* [submitted, 2014], and is believed to be partially caused by different measured pitch angle ranges.

Figure 3.8 shows the ratio of differential MEPED flux to coincident differential IDP flux during 2009 at varying L-shells in both hemispheres combined. The year 2009 is used as there were no solar proton events that could corrupt both the MEPED and IDP instruments. Each L-shell bin has a width of 0.25, and measurements with the equivalent of four or fewer detected electron counts by either MEPED or IDP are not included to remove possible noise floor bias. IDP does not report a count rate, so the necessary flux to be above a noise floor of 4 counts is calculated. IDP combines two channels when not in burst mode, thus the noise floor would be four counts in each channel (eight counts total). This occurs over a four second measurement, resulting in a minimum count rate of 2 counts per second. Dividing this count rate by the nominal geometric factor (1.2 cm^2 sr) and energy bin width (17.9 keV) results in the minimum differential flux required to be above the noise floor of four counts (0.0931 counts/sec/cm^2/sr/keV). All L-shells seen in the plot used 15 or more coincident spectra to get
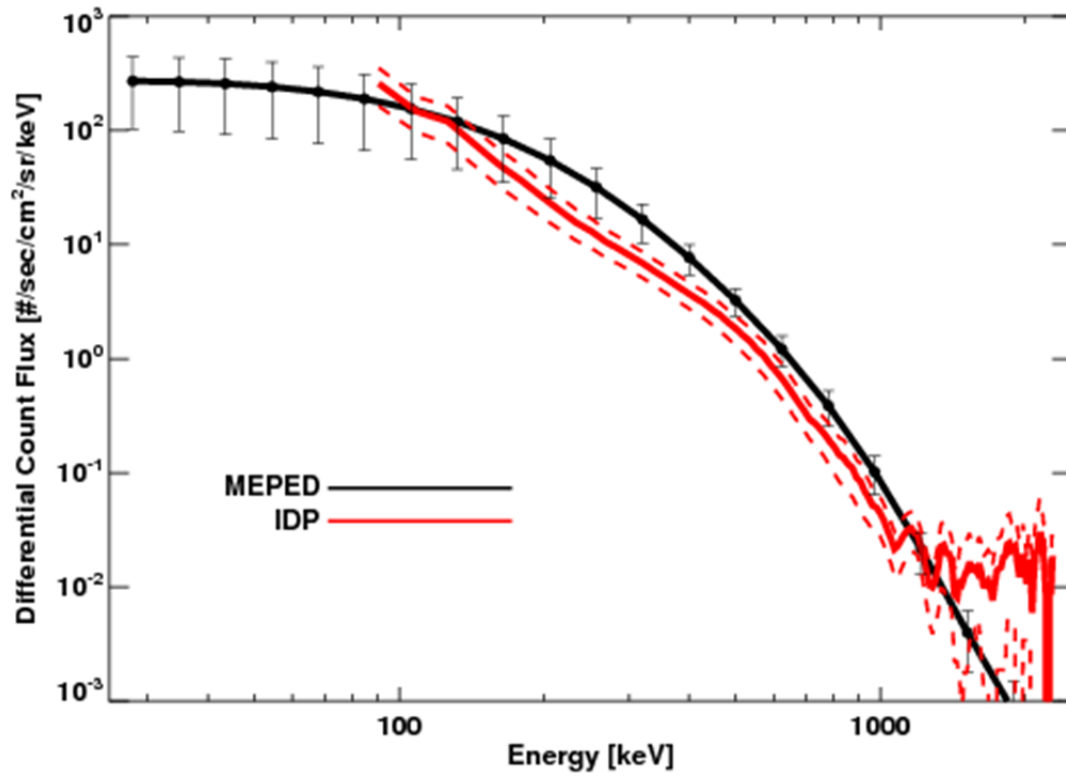
Figure 3.7: Average of SH coincidence measurement spectra from DEMETER IDP (red) and MetOp-02 MEPED (black) in 2009 at L-shell values between 6.0 and 6.25. Dashed red lines and black vertical bars represent one mean standard error for IDP and MEPED respectively.
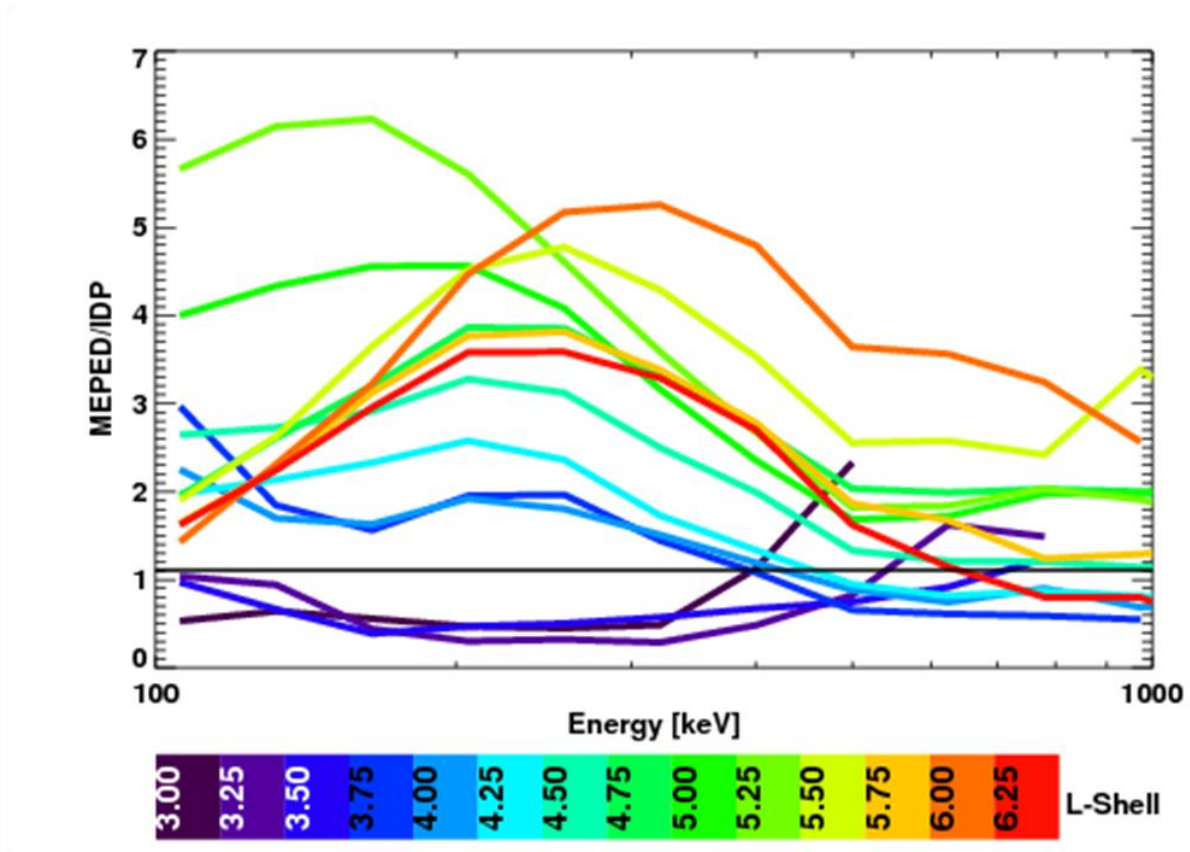
Figure 3.8: Ratio of average electron differential flux between MetOp-02 MEPED and DEMETER IDP coincidences during 2009 for L-shell bins with width 0.25. Coincident spectra are taken from both the NH and SH and a minimum of 15 spectra were required for each L-shell bin. All measurements were required to have more than four electron counts as would be detected by the instrument before conversion to differential flux. A black line representing the expected ratio of MEPED to IDP based on changes to magnetic field strength using an inverse cubed relation has been placed at a value of 1.1. Each colored line represents an L-shell bin with the lower edge of the bin marked in the color bar.

average differential flux values. The 1.1 line that marks the expected ratio between MEPED and IDP differential flux based only on changes to magnetic field strength is marked by a black line. At L-shell values above 3.75, MEPED consistently shows greater than expected electron differential flux compared to IDP. Maximum differences occur between 100 keV and 300 keV. Low L-shells (< 3.75) are generally below the expected ratio line (1.1); this is likely caused by lower electron count rates towards the outer edge of the outer belt region. The consistent high bias of MEPED relative to IDP could be due to several factors, including sensitivity of IDP to a broader range of pitch angles than MEPED, a more rapid differential flux decrease with decreasing altitude than predicted by magnetic field strength changes, and/or a spectral shape dependence on L-shell. This latter hypothesis is supported by the variable nature of the comparisons in Figure 3.8 for different L shells. The observed bias might also be due to residual proton contamination in the MEPED data, but this is unlikely since the comparisons were conducted for a time period of relatively quiet geomagnetic activity.

Figure 3.9 shows a scatter plot of coincident measurements during 2009 between IDP and corrected MEPED. Points represent integrated electron differential flux (counts cm^{-2} s^{-1} sr^{-1}) between 100 keV and 300 keV. This energy bin is used since both IDP and MEPED measure it. A black bisector line showing the expected increase in flux from IDP to MEPED (1.1 to 1 line) is drawn for reference. Colors represent the MEPED L-Shell from which the measurement coincidence is taken.

Comparison of corrected MEPED electron fluxes to IDP reveals two distinct populations. One population shows rough agreement between corrected MEPED and IDP, while the second shows significantly reduced electron fluxes in corrected MEPED results at locations of low electron flux identified by both satellites. These measurements occur at low L-Shell values. The
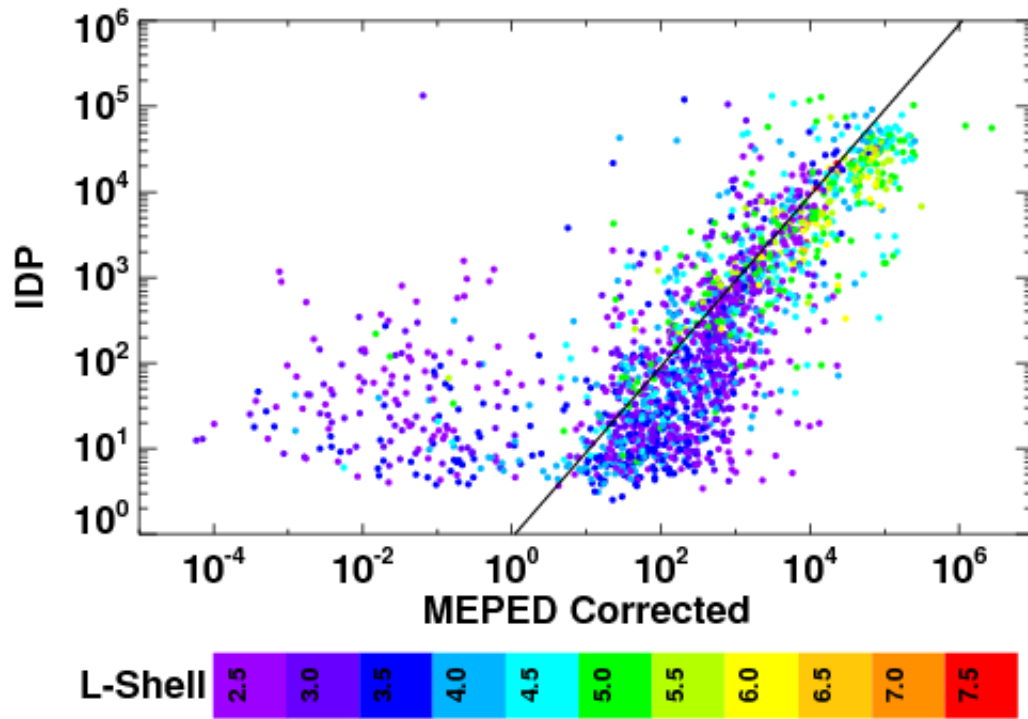
Figure 3.9: Scatter plot of integrated electron differential flux from 100-300 keV for all coincident measurements between DEMETER IDP and MetOp-02 in the year 2009. Comparisons are shown between IDP and corrected MEPED measurements. Points are colored by associated L-Shell value. Black line is a slope of 1.1 for reference.

population of points near the bisector are in agreement with the results presented by *Whittaker et al.* [submitted, 2014] (their Figure 7).

The reduced MEE population at low L-Shell values in the corrected MEPED data is believed to be an artifact caused by the correction method. When the level of proton contamination is of a similar magnitude to the electron count signal, the correction method will cancel out the electron counts. This will happen when electron counts are very small or proton counts are very high. In the case of a very low electron count (~1 count/sec), noise from the proton channel will be counted as a source of contamination in the electron channel and the correction method will artificially decrease the already small electron count signal. A similar influence from the correction method can be seen at times when proton contamination is much greater than the electron count measurement. For example, electron channel neutralization will occur during a SPE when proton contamination is very large. This is seen by the black colored points in Figure 3.3. Note that high energy protons, such as those over the polar cap during a SPE, do not get counted as contamination by the correction method and are not removed. Thus any data used during a SPE when proton fluxes are very high, or when the electron signals are very low (e.g., outside the outer Van Allen belt precipitation regions), should be treated with extreme skepticism.

3.5 Conclusions

In this work a correction method to remove proton contamination from the POES MEPED instrument was applied and compared to coincident measurements from DEMETER IDP. Results from the correction method are:

- Removal of proton contamination from electron channels with the exception of contamination from protons with energies higher than the detection abilities of the P6 channel (> 10 MeV).

- Differential flux from POES MEPED measurements can now be used with error bars for both medium energy protons and electrons (25 keV $- 10$ MeV).

Analysis of corrected MEPED values reveals:

- Enhanced MEE signals during geomagnetic storms induced by a CME are not caused by proton contamination.

- In some circumstances the correction method can artificially neutralize electron signals when the level of recognized proton contamination is on the same order of magnitude as the original electron signal, such as in the case of very low electron fluxes (e.g., low latitudes) or during very high proton fluxes (e.g., the SAA or during a SPE).

- Electron differential flux reported by MEPED is slightly greater than expected compared to IDP in 2009. The most likely explanations for this are different pitch angle ranges viewed by MEPED and IDP or that differential flux changes with altitude more than is expected by magnetic field strength changes alone.

Future work that could improve this method are as follows:

- Inclusion of a proton channel degradation correction prior to processing by the correction method described in this work.

- Removal of measurements where noise is of the same magnitude as signal in the electron and proton channels.

- More understanding of possible particle differential flux changes with altitude aside from those induced by magnetic field strength differences.

Chapter 4

Simulated impacts of medium energy electrons on the middle atmosphere

This chapter includes the current form of *Peck et al.* (manuscript in preparation, 2014). In this work the resulting medium energy electron (MEE) differential flux spectra from *Peck et al.* [submitted, 2014b] (e.g., Chapter 3) are converted into hemispheric maps of MEE precipitation and input into the Specified Dynamics version of the Whole Atmosphere Community Climate Model (SD-WACCM). Simulations are split into three cases: no MEE precipitation, lower boundary MEE precipitation, and upper boundary MEE precipitation. Analysis focuses on the MEE precipitation impact on middle atmosphere NO_x concentrations.

The main results of *Peck et al.* (manuscript in preparation, 2014) are (1) SD-WACCM has weak mesospheric descent, causing EPP-IE related NO_x concentrations to be too low in the stratosphere during late February and March 2004 regardless of MEE precipitation, and (2) current understanding of MEE precipitation into the atmosphere is flawed causing difficulties in properly modeling ion-pair production from MEEs. The conclusions of this paper are that MEE precipitation can generate large amounts of NO_x that can reach the stratosphere; however, there are not enough observations to properly model MEE precipitation. More observations combined with additional analysis and theory is necessary to further understand MEE precipitation.

4.1 Introduction

Middle atmosphere chemistry is known to be heavily impacted by energetic particle precipitation (EPP). EPP can produce NO_x (hereafter referred to as EPP-NO_x) [*Rusch et al.*,

1981] and HO_x (hereafter referred to as EPP-HO_x) [*Solomon et al.*, 1981]. The atmospheric depth of ion production caused by EPP that results in NO_x and HO_x creation depends on the type and energy of the particle, with more energetic particles penetrating deeper into the atmosphere [*Roble and Ridley*, 1987; *Fang et al.*, 2008; 2010]. This work will focus on the potential impacts of medium energy electrons (MEEs, ~20 keV to 2MeV) from the Earth's radiation belts, an EPP source that is currently not included in most models.

EPP-HO_x and EPP-NO_x can impact the atmosphere through two mechanisms. The EPP Direct Effect (EPP-DE) is the direct production of NO_x and HO_x by energetic particles. The EPP Indirect Effect (EPP-IE) is when EPP-NO_x produced in the thermosphere and mesosphere descends through the atmosphere during polar night to impact chemistry in the lower mesosphere and stratosphere [*Randall et al.*, 2006; 2007]. EPP-HO_x enters a catalytic cycle with O_3; however this is generally limited to the mesosphere and upper stratosphere since HO_x has a short lifetime and will not travel far beyond where it is initially produced. Therefore, EPP-HO_x is only applied to the EPP-DE and requires high energy particles such as solar protons [*Damiani et al.*, 2010; *Jackman et al.*, 2011; *Sinnhuber et al.*, 2012]. The NO_x catalytic cycle with O_3 is the primary loss mechanism for O_3 in the stratosphere above ~25 km [*Garcia and Solomon*, 1994; *Watson et al.*, 1986]. EPP-NO_x can comprise a large portion of upper stratospheric NO_x [e.g., *Randall et al.*, 2009], and can be produced in the lower mesosphere and upper stratosphere through the EPP-DE or can be transported as part of the EPP-IE.

There are several types of energetic particle precipitation that can produce NO_x and HO_x. Studies of the EPP-DE have shown large impacts on middle atmosphere O_3 from solar proton events (SPEs) in models [e.g., *Jackman et al.*, 2005; 2008]. *Funke et al.* [2011] conducted a model and data intercomparison focused on a SPE that occurred at the end of October 2003,

known as the "Halloween Storm" along with subsequent events and found that models did a decent job of reproducing the EPP-NO_x and EPP-HO_x signatures seen in satellite observations. Auroral energetic electrons are capable of reducing O_3 in the stratosphere and that models can recreate solar cycle signals that are seen in reanalysis data and observations with some limitations in the magnitude of the signals seen, especially in temperature and wind [*Marsh et al.*, 2007; submitted, *Peck et al.*, 2014a]. *Randall et al.* [2006; 2009] showed that varying atmospheric dynamics can play a major role in the amount of EPP-NO_x that can descend into the upper stratosphere from higher altitudes. The greatest NO_x descent signal by the EPP-IE observed to date occurred in the 2003-2004 NH winter. The extraordinary NO_x signal was originally attributed to the SPEs in October and November 2003, [*Natarajan et al.*, 2004; *Seppälä et al.*, 2004; *Orsolini et al.*, 2005; *Rinsland et al.*, 2005] but were later shown to have come from enhanced descent caused by a major SSW in January 2004 [*Manney et al.*, 2005; *Randall et al.*, 2005] However, recently *Randall et al*. [submitted, 2014] shows that WACCM does not have nearly enough stratospheric NO_x produced in 2004 at times following the Halloween Storm in late winter. This failure to create enough NO_x is attributed to either a missing source of NO_x production, such as from MEE precipitation, or weak simulated descent permitting less EPP-NO_x to reach the stratosphere. In this study, MEE precipitation will be included in similar simulations to those used by *Randall et al.* [submitted, 2014] in order to test if including MEE precipitation will allow for models to better match satellite observations.

MEEs and higher energy relativistic electrons from the radiation belts have been theorized to contribute a large source of NO_x to the middle atmosphere [*Baker et al.*, 1987; *Callis et al.*, 1991]. The Polar Operational Environmental Satellites (POES) Space Environment Monitor (SEM) Medium Energy Proton/Electron Detector (MEPED) is a useful source for

quantifying the amount of MEE precipitation into the atmosphere. *Codrescu et al.*, [1997] used the SEM version 1 (SEM-1) MEPED instruments to create input into the Thermosphere-Ionosphere-Mesosphere Electrodynamic Global Circulation Model (TIME-GCM). Results showed significant increases in mesospheric NO_x; however the model simulation was only run for 20 days and could not be used to study the EPP-IE from MEE precipitation. It is also known that the SEM-1 MEPED and the more recent SEM-2 MEPED are plagued by electron channel contamination by protons [*Evans and Greer*, 2000; *Rodger et al.*, 2010]. *Peck et al.* [submitted, 2014b] implemented a correction method for the SEM-2 MEPED data using a multiple spectrum best fit algorithm and the gathering power results from *Yando et al.* [2011]. This resulted in electron spectra that include data for both MEE (20 keV – 1 MeV) and relativistic electron precipitation (REP, >1 MeV). This work will input corrected SEM-2 MEPED data from *Peck et al.* [submitted, 2014b] into the Whole Atmosphere Community Climate Model (WACCM), building upon the work started by *Codrescu et al.* [1997] in understanding the impacts of MEE precipitation on the middle atmosphere.

Due to the lack of trustworthy MEE data sources, many studies have attempted to quantify the impacts of MEE precipitation indirectly by using mesospheric HO_x as a signal of MEE precipitation. *Verronen et al.* [2011] showed strong correlations between mesospheric HO_x and MEE precipitation from SEM-2 POES, with between 57 and 87% of OH variation explained by energetic electron precipitation. *Anderson et al.* [2012] showed similar results where nighttime mesospheric OH concentrations could be used as a proxy for MEE precipitation. *Andersson et al.* [2014] expanded upon those results by showing meridional variations in OH production attributed to MEE precipitation. They also show that little to no OH production is seen within the Southern Atlantic Anomaly (SAA), a region of weaker magnetic field strength

over Brazil where particle precipitation from the inner radiation belt was believed to be strongest. This result suggests that there might be little to no particle precipitation actually occurring in the SAA.

This work will take the corrected SEM-2 MEPED data from *Peck et al.* [submitted, 2014b] and place it into the WACCM model to study the impacts of MEE precipitation on the middle atmosphere. This work will focus on comparing satellite observations of EPP-NO_x to WACCM with and without MEEs. The goal of this work is to investigate the importance of MEE precipitation as a source of middle atmosphere NO_x. This work will also quantify the possible impacts on stratospheric O_3 from MEE precipitation. Section 4.3 will describe the method by which the SEM-2 MEPED data is prepared for use in WACCM, as well as how the WACCM simulations are designed. Section 4.4 will show results from WACCM simulations and satellite observations for NO_x mixing ratios. Section 4.5 will present discussion of the implications of the results, including perceived impacts on stratospheric O_3 and improvements that can be made to the analysis presented here. Section 4.6 will summarize conclusions.

4.2 Satellite Data

This work will compare multiple model simulations to NO_x measurements from various satellites. Some information about the satellites follows. For information about POES SEM-2 MEPED, refer to Section 1.8. All instrument data used in this Chapter is the same as used in *Randall et al.* [submitted, 2014].

The Halogen Occultation Experiment (HALOE) is a solar occultation instrument that is capable of measuring NO and NO_2 by measuring spectral bands centered at 5.26 μm and 6.25 μm respectively. HALOE was launched on board the Upper Atmosphere Research Satellite and began observations on 11 October 1991. Measurements are taken at 15 sunrises and sunsets.

Details about the instrument design can be found in an overview by *Russell et al.* [1993]. Validation of HALOE NO_x is described in *Gordley et al.* [1996]. Measurement of NO and NO_2 is valid from the lower stratosphere (25 km) through 130 km and 50 km respectively. NO is known to have a low bias at times between 30 and 60 km.

The Stratospheric Aerosol and Gas Experiment (SAGE) II measures NO_2 using solar occultation. The instrument was launched from the space shuttle on 5 October 1984, and measures NO_2 based on the difference of measured irradiances at 0.448 and 0.453 μm. The instrument measuring technique and validation of NO_2 measurements are described by *Cunnold et al.* [1991]. SAGE II NO_2 measurements were found to have a precision of 5% between 36 km and a varying lower altitude (25 km at equatorial latitudes and 29 km at midlatitudes). This precision decreases by approximate 3% per kilometer above 36 km, meaning a precision of about 17% near 40 km. A low bias in NO_2 measurements is incurred above 37 km, which gets worse with higher altitudes.

SAGE III is another solar occultation instrument that measures NO_2 in the middle atmosphere. This instrument was launched in December 2001. *Rault et al.* [2004] described the instrument and validation of the SAGE III NO_2 measurements. Retrievals for NO_2 cover a vertical range of 15 to 40 km with a resolution of 2 km, along with a precision of 20% using spectral absorption features between 430 and 450 nm.

The Polar Ozone and Aerosol Measurement (POAM) III instrument also measures NO_2 using solar occultation and was launched in March 1998. POAM III measures a vertical profile of NO_2 densities between 20 and 45 km with a vertical resolution of 1.5-2.5 km at altitudes below 40km, increasing to 7 km at an altitude of 45 km. A validation of POAM III measurements is described in *Randall et al.* [2002]. There is a slight high bias in POAM III NO_2

measurements compared to HALOE at 40 km (17% higher in POAM than HALOE). Predicted random errors of up to 5% also exist, along with up to 10% errors that can be caused by sunspots.

The Atmospheric Chemistry Experiment Fourier Transform Spectrometer (ACE-FTS) is capable of measuring NO and NO_2 using solar occultation and was launched on 12 August 2003, with science measurements beginning February 2004. A full instrument description is presented by *Bernath et al.* [2005]. Data used in this work comes from ACE-FTS version 2.2. *Kerzenmacher et al.* [2008] presented a validation of ACE-FTS NO and NO_2. ACE-FTS measurements were found to agree with other satellites to within 20% between 25 and 40 km. ACE-FTS NO measurements agreed with HALOE to within 8% between 22 and 64 km.

The Michelson Interferometer for Passive Atmospheric Sounding (MIPAS) can measure polar stratospheric NO and NO_2 during all seasons using atmospheric limb emissions. MIPAS was launched on 1 March 2002 and is described by *Fischer et al.* [2008]. Comparison of NO and NO_2 was conducted by *Kerzenmacher et al.* [2008] between MIPAS and ACE-FTS. They found MIPAS NO to be within 10% of ACE-FTS from 15-42 km, and MIPAS NO_2 to be within 20% of ACE-FTS between 28 and 44 km.

4.3 Methods

This section will describe the creation of hemispheric maps for use in the National Center for Atmospheric Research (NCAR) Specified Dynamics version of the Whole Atmosphere Community Climate Model (SD-WACCM) and how MEE input is implemented in WACCM.

4.3.1 MEE Input Maps

The data used to create hemispheric maps of MEE precipitation comes from the corrected POES MEPED data as described in *Peck et al.* [submitted, 2014b]. A case study of the Northern

Hemisphere (NH) 2003 - 2004 winter is used in this work. The selection of this time period is based on work by *Randall et al.* [submitted, 2014]. They showed that SD-WACCM is unable to reproduce the extraordinary EPP-IE NO_x descent signal seen in early 2004. This case study will show whether the inclusion of MEE will assist the model in reproducing the expected EPP-IE signal. To analyze a case study of Northern Hemisphere (NH) winter 2003-2004, the maps are designed in the form of a sensitivity study. Since it is not known how to properly model particle pitch angle distributions inside the bounce loss cone (BLC), we create upper and lower limit cases that assume particle flux constant at all particle pitch angles within the BLC. Step one is to calculate the BLC edge particle pitch angle at each satellite measurement location. Step 2 is to calculate the energy differential particle count flux distribution at the satellite BLC angle for each measurement that will be used in the upper bound. The lower bounding case will simply use the differential particle count flux distribution from the corrected MEPED 0° detector as a proxy for all angles in the BLC. All cases are scaled to properly represent electron flux into the atmosphere as opposed to at the satellite measuring altitude, as described below. The lower boundary case is similar to *Codrescu et al.* [1997], however in their case a Maxwellian distribution for energy differential particle flux was used whereas distributions used in this work come from *Peck et al.* [submitted, 2014b]. Step 3 is to take the fluxes calculated in step 2 and combine them into hemispheric maps for the NH and Southern Hemisphere (SH).

4.3.1.1 Calculation of the satellite BLC angle

The POES satellite data reports the satellite altitude and optimum particle measurement pitch angle for both the 0° and 90° MEPED telescopes. The magnetic field strength at both the satellite altitude (~850 km) and 120 km, taken here to be the starting altitude at which all particles will be deposited into the atmosphere, is calculated using the International Geomagnetic

Reference Field (IGRF) model [*IAGA*, 2010]. The BLC particle pitch angle can be calculated using the following formula (*Evans and Greer* [2000], their equation 2.3.2):

$$\frac{\sin^2(\alpha_{\text{sat}})}{B_{\text{sat}}} = \frac{\sin^2(\alpha_0)}{B_0} \tag{4.1}$$

where α_{sat} is the particle pitch angle at the satellite altitude and location in radians, α_0 is the particle pitch angle at the starting atmospheric deposition altitude and geographic location that follows the magnetic field towards the Earth's surface from the satellite, B_{sat} is the magnetic field strength at the satellite altitude and location in Tesla, and B_0 is the magnetic field strength at the same altitude and location used for α_0.

At the starting atmospheric deposition altitude all particles are assumed to be within the BLC. Therefore, $\alpha_0 = \pi/2$ for the atmosphere BLC pitch angle. B_{sat} and B_0 are calculated using the IGRF model. Thus the BLC pitch angle at the spacecraft is related to the magnetic field strengths according to:

$$\sin \alpha_{\text{BLC}} = \sqrt{B_{\text{sat}}/B_0} \tag{4.2}$$

4.3.1.2 Calculating BLC differential particle count flux

Upon solving for α_{BLC} the total particle flux in the bounce loss cone must be calculated. This is first done by fitting the two reported MEPED particle pitch angles to a sine curve. We assume that zero particles exist at a pitch angle of 0° and that the maximum number of particles will exist at 90°. Therefore it can be assumed that the sine equation fit will not have a phase shift or an offset, yielding the following form of the sine fit:

$$J_D(\alpha_{\text{sat}}) = A \sin^n(\alpha_{\text{sat}}) \tag{4.3}$$

where $J_D(\alpha_{\text{sat}})$ is the differential particle count flux for a given pitch angle at the satellite with units of counts/cm^2/s/sr/keV, A is the amplitude of the sine function fit with units of counts/cm^2/s/sr/keV, and n is the power of the sine fit. This form of fit has been used to study

particle pitch angles in other studies [e.g., *Gu et al.*, 2011; *Vampola*, 1998], though has not been used in application to the BLC. For simplicity we assume *n* equal to 1 due to a lack of particle pitch angle data with which to fit against. In order to create a more accurate representation of particle flux with pitch angle, an instrument would need to measure particle fluxes at a variety of pitch angles both within and outside the BLC, across multiple L-shells, and through several Magnetic Local Times (MLTs); such an instrument does not currently exist.

Upon calculating the best fit to Equation 4.3 (e.g., solving for *A*) the next step is to calculate the total differential particle count flux in the BLC entering the atmosphere. As particles in the BLC approach the atmosphere, their pitch angles will span a larger range, until they cover all pitch angles at the atmosphere deposition altitude, assumed here to be 120 km above the Earth's surface. Thus at 120 km, we assume the BLC particle flux covers a full hemisphere (e.g., α_{BLC} at the atmosphere equals 90°) and flux can be integrated over the solid angle for a whole downward hemisphere assuming vertical magnetic field lines using the following equation:

$$J_F = \int_0^{2\pi} \int_0^{\pi/2} J_D(\alpha_0) \cos \alpha_0 \sin \alpha_0 d\alpha_0 d\theta \qquad (4.4)$$

such that the differential particle count flux over the entire BLC, J_F, with units counts/cm^2/s/keV is the integral of a solid angle over a hemisphere using the perpendicular component of the differential particle count flux for a given pitch angle at the atmosphere (120 km), $J_D(\alpha_0)$, with units counts/cm^2/s/sr/keV, and θ is the azimuthal angle.

This can be simplified into the following form (*Evans and Greer* [2000], their equation 2.3.3):

$$J_F = 2\pi \int_0^{\pi/2} J_D(\alpha_0) \sin \alpha_0 \cos \alpha_0 d\alpha_0 \qquad (4.5)$$

In the lower bound case, we assume that the particle flux is constant at all pitch angles and equal to the measured flux from the 0° detector:

$$J_D(\alpha_0) = J_D \qquad (4.6)$$

Thus Equation 4.5 simplifies to:

$$J_F = \pi J_D \qquad (4.7)$$

The upper boundary case uses the same equations as the lower boundary case. The difference comes from the value used for J_D in Equation 4.6. In this case we use the value $J_D(\alpha_{\mathrm{BLC}})$ from Equation 4.3, where α_{BLC} was calculated in Equation 4.2.

4.3.1.3 Creation of Hemispheric Maps

With the BLC differential count flux calculated, we create time-varying hemispheric maps that can be used as MEE input in WACCM.

Map binning is performed in both the NH and SH using a horizontal 2° MLT by 2° magnetic latitude grid. The POES SEM-2 data processing and archiving processes include satellite orbit information and use the IGRF model in order to report the MLT and L-shell of each measurement. The magnetic latitude of each point is calculated using the POES reported L-shell at each measurement with the following equation:

$$L = \frac{1}{\cos^2 \Lambda} \qquad (4.11)$$

where L is the L-shell value and Λ is the invariant latitude, an approximation for magnetic latitude, in radians.

For a given day, a 5-day running average is used with all available satellites with 16-second averaged electron count rates acquired from *Peck et al.* [submitted, 2014b]. For example, on January 3$^{\mathrm{rd}}$, 2004, a mean of measurements for each bin is taken using data from 1 January 2004 through 5 January 2004 with the POES-15/-16/-17 satellites. Only measurements with less

than a 200% error are used and any bins with less than 5 measurements within the bin average calculation are rejected as unusable, removing at least 75% of the calculated bins on the map. Note that at this point there is a map for each energy bin in the electron differential count flux spectrum. Thus the units for each bin are counts/cm^2/s/keV.

Differential count flux is then converted to a differential energy flux. This is done by multiplying each map of a given energy bin by bin center energy in ergs. Thus the map values have units of erg/cm^2/s/keV. Edge bins, bins that have data preceding (following) them in MLT but no useful data following (preceding) them, are calculated to be the average of the 3 bins preceding (following) them. All remaining empty or unused bins are filled in using a linear interpolation in MLT. A linear interpolation is acceptable due to the large amounts of data used as a consequence of the 5-day running average. Finally, a 5 by 3 bin (10° MLT by 6° magnetic latitude) boxcar smooth is applied.

The maps used in this work were designed to examine the EPP-IE, which occurs over the course of months, and were thus not concerned with short term variability in MEE precipitation. If analysis for other work using precipitating MEEs requires short term variability in MEE flux, we would recommend using maps that fit smaller amounts of data (finer time resolution) to a sine curve in MLT as done in *Fang et al.* [2007].

Figure 4.1 shows a representative map of the SH, integrated energy flux, on 10 January 2004 in magnetic latitude and MLT for the upper bound case. Circles show individual satellite measurements that were averaged together to create the completed map. As was described above, areas where no measurements were taken are calculated using a linear interpolation from surrounding bins that had valid measurements. This mapping procedure does a reasonable job at
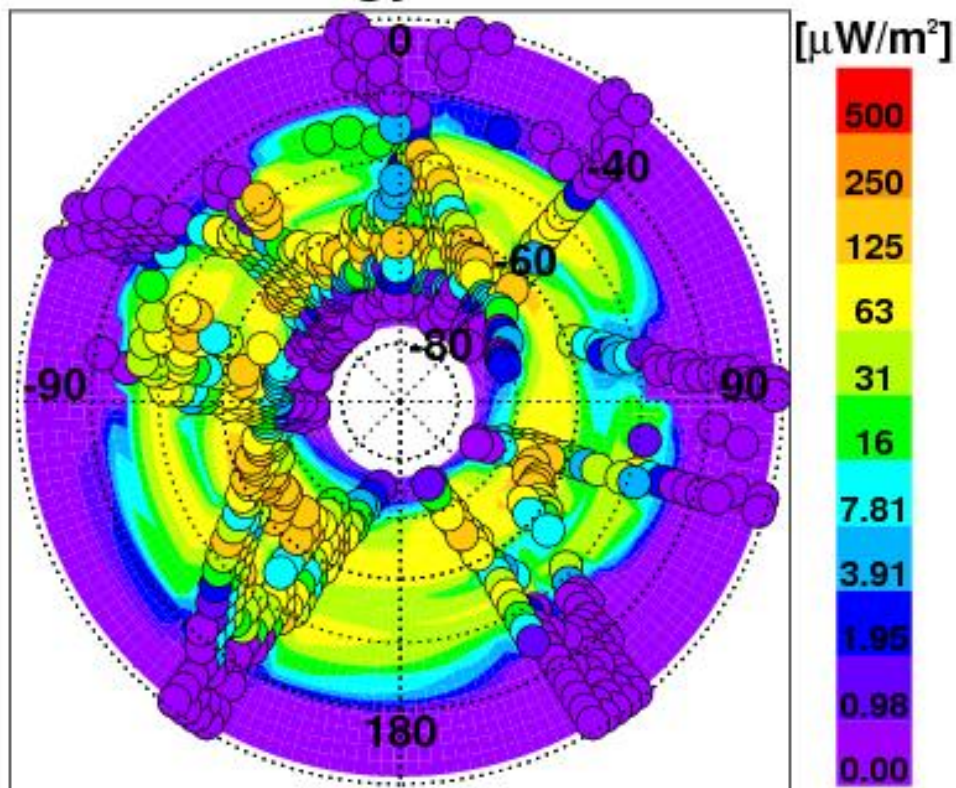
Figure 4.1: Total energy flux in the SH from MEE precipitation for the upper boundary case in MLT and magnetic latitude centered on the magnetic South Pole. MLT is reported in degrees, where 0° is 0:00, 90° is 6:00, 180° is 12:00, and 270° is 18:00. Map horizon is set at 30°S magnetic latitude. Circles represent individual total flux measurements used to create the complete map.

representing the data points shown, but does not have a fine temporal resolution due to the use of a 5-day running average.

Examples of maps for both hemispheres integrated over the entire electron energy spectrum (~20 keV – 2 MeV) for lower boundary and upper boundary cases are shown in Figure 4.2 for 10 January 2004. Figure 4.2 is similar to Figure 4.1 but does not show the individual points used to create the maps. The upper boundary case maps show higher values at all MLTs within the outer belt (~65° magnetic latitude) and inner belt (~50° magnetic latitude) compared to the maps created by *Codrescu et al.* [1997] and the lower boundary case. This is partially caused by longitudinal variations in magnetic field strength that would have increased particle fluxes regardless of MLT. This effect will cause a ring shape in MLT if averaged over a long (daily) time period, which is in agreement with other studies [e.g., *Barth et al.*, 2001; 2003]. However, taking data from small (60°) geographic longitude bands also creates similar results (not shown), suggesting that a large portion of the enhanced MEE precipitation comes from the assumptions used to calculate the flux within the BLC used in the upper boundary case.

A caveat in the creation of the hemispheric maps is the potential for overestimation by noise. It is believed that since the MEPED instrument channels cannot measure negative particle count fluxes, a positive bias will show up in the data. This can be taken into account as a noise floor error in the instrument measurements [*Rodger and Clilverd*, personal communication]. Since this error only occurs with very low values (e.g., single particle counts), it should have a small overall impact on MEE generated EPP-NO_x and EPP-HO_x in model simulations. This error is not taken into account in this work and deserves further study in order to apply a proper correction to the MEPED data beyond what is done in *Peck et al.* [submitted, 2014b].
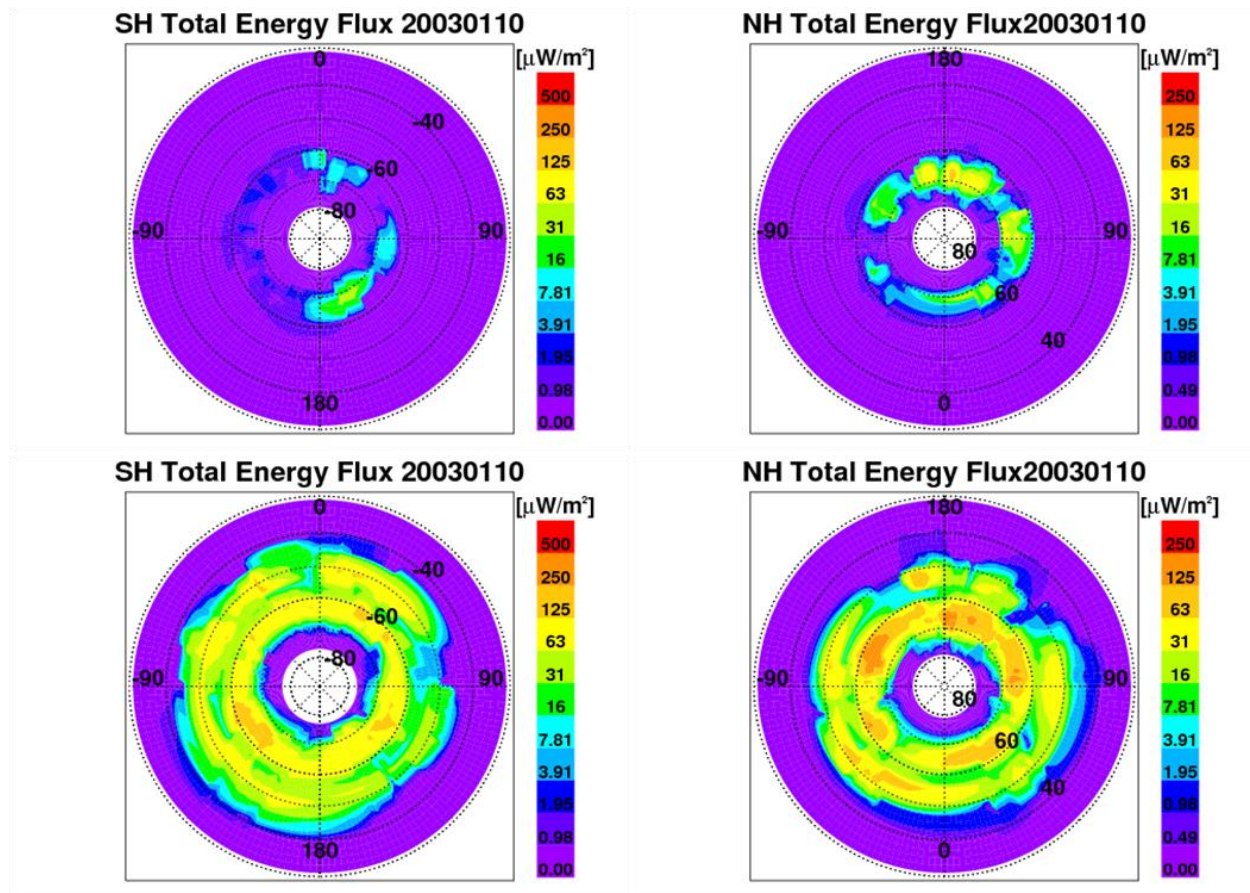
Figure 4.2: Total energy flux for the SH (left column) and NH (right column) for low boundary (top row) and upper boundary (bottom row) cases. Individual plots are similar to Figure 4.1, but without individual measurements marked.

4.3.2 SD-WACCM Simulations

This study uses WACCM in the Community Earth System Model (CESM) framework version 1.2.2 [*Hurrell et al.*, 2013; *Marsh et al.*, 2013]. WACCM is an extension of the Community Atmosphere Model version 4 (CAM4) [*Gent et al.*, 2011] and uses a finite volume dynamical core [*Lin et al.*, 2004]. The WACCM chemistry module is derived from the Model for Ozone and Related chemical Tracers version 3 (MOZART3) [*Kinnison et al.*, 2007]. Planetary waves are resolved in the model and parameterizations for gravity waves are as described in *Richter et al.* [2010]. Sea surface temperatures are determined using a merged climatology on the CAM4 grid [*Hurrell et al.*, 2008]. Upper atmosphere inputs are described in *Peck et al.* [submitted, 2014a] with the aurora module coming from the Thermosphere-Ionosphere-Mesosphere Electrodynamics General Circulation Model (TIME-GCM) [*Roble and Ridley*, 1987] and solar spectral irradiance from a combination of *Lean et al.* [2005] and *Solomon et al.* [2005].

The SD-WACCM simulations in this study use a horizontal grid of 1.9° latitude by 2.5° longitude, with 88 vertical hybrid sigma-levels between the surface and ~145 km. Vertical level resolution decreases with increasing altitude. Vertical resolution in the stratosphere is ~1 km and ~3 km in the mesosphere. WACCM uses a 30 minute time step. Solar proton events are included in the model simulations as described in *Jackman et al.* [2008]. Winds, temperature, surface pressure, heat fluxes, and surface wind stress are taken from the Modern Era Retrospective Analysis for Research and Applications (MERRA) [*Reinecker et al.*, 2011] and a nudging coefficient of 0.01 is used (e.g., dynamical variables are calculated with a linear combination of 1% from MERRA and 99% from WACCM at each time step). The nudging scheme is used

below 50 km with a linear transition to no nudging at 60 km. Above 60 km the model calculates all variables without nudging.

The hemispheric maps for the upper and lower boundary cases are input into SD-WACCM with ion pair production rates calculated using the mono-energetic electron ionization rate scheme developed by *Fang et al.* [2010] within the model simulation. The ion pair production from each energy bin is summed together to get total ion pair production from MEE precipitation. Ion pair production is then converted into NO and OH production using the same process as solar protons in *Jackman et al.* [2008]. MEE HO_x production efficiency is calculated using the same lookup tables as SPEs in *Jackman et al.* [2005] (their Table 1). NO_x production assumes 1.25 nitrogen atoms produced per ion pair, split between ground state (0.55 per ion pair) and excited state (0.7 per ion pair) [*Porter et al.*, 1976]. Contributions to middle atmosphere chemistry from Bremsstrahlung X-rays are not taken into account in these simulations and may add another important source of ionization below 50 km [*Frahm et al.*, 1997]. This study uses three simulations: an upper boundary for MEE precipitation (U-MEE), a lower boundary for MEE precipitation (L-MEE), and no MEE precipitation (No-MEE). Results from these simulations were output on the SD-WACCM grid and at satellite measurement locations using the nearest grid point output for direct comparisons to observations without the use of interpolation.

4.4 Results

Figure 4.3 plots daily average MEE precipitation ion pair production rates ($cm^{-3}s^{-1}$) between October 2003 and March 2004 in the middle atmosphere for the L-MEE (left) and U-MEE (right) simulations. The No-MEE simulation does not have any ion pair production from MEE precipitations and is therefore not shown. The maximum MEE ion-pair production occurs
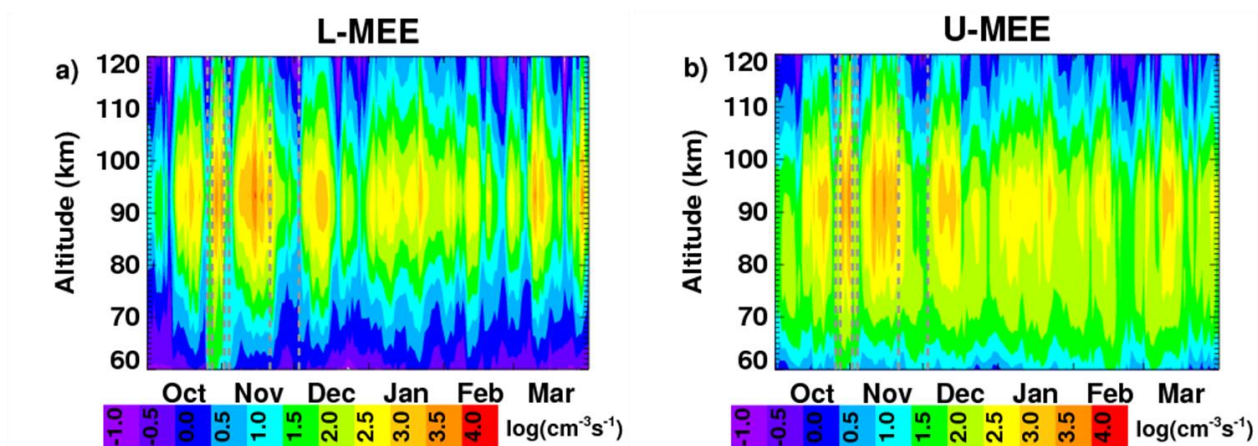
Figure 4.3: Ion-pair production $(cm^{-3}s^{-1})$ on a log scale in a polar cap area weighted average (>70°N) for October, 2003 through March, 2004. Simulations shown are the L-MEE (left) and U-MEE (right) cases.

around 90 km, varying from approximately 10 to 1000 cm^{-3}s^{-1} at that altitude. Substantial ion-pair production (>100 cm^{-3}s^{-1}) reaches as low as 70 km. To put this in perspective, the ion-pair production from protons during the Halloween Storm maximized at over 5000 cm^{-3}s^{-1} at ~60 km [*Jackman et al.*, 2008]. Thus while a SPE causes more ion-pair production during an event, MEE precipitation frequently creates ion-pair production rates of similar orders of magnitude with and without a SPE occurring.

Figures 4.4 through 4.6 compare model simulations and solar occultation measurements at satellite measurement locations near 40 km for 2004. Measurements shown come from HALOE, SAGE II, POAM, and SAGE III. Similar to *Randall et al.* [submitted, 2014], the No-MEE simulation does not recreate the odd nitrogen signal seen in observations in the Arctic late winter and spring of 2004. The L-MEE case shows too much background NO_x for most times, but does not show enough NO_x in April-June when the EPP-IE is occurring. Too much background NO_x continues to be an issue in U-MEE case. The L-MEE case appears to give the proper timing for NO_2 descent to 40 km, based on the comparisons with POAM III and SAGE III, but mixing ratios peak ~2.5 ppbv too low. By contrast, the U-MEE case appears to show NO_2 descent occurring too early (January and February) with peak values similar to observations also occurring too early (March).

A comparison of NO_x between ACE-FTS and the SD-WACCM simulations are shown in Figure 4.7 marked with days since February 20th, 2004 for the NH. The timeframe shown here demonstrates NO_x descent from the EPP-IE. The No-MEE case does not match observations, with far too little NO_x descent occurring related to the EPP-IE. Neither of the cases that include MEE precipitation shows enough NO_x descent in the EPP-IE tongue, but both cases show too

No-MEE
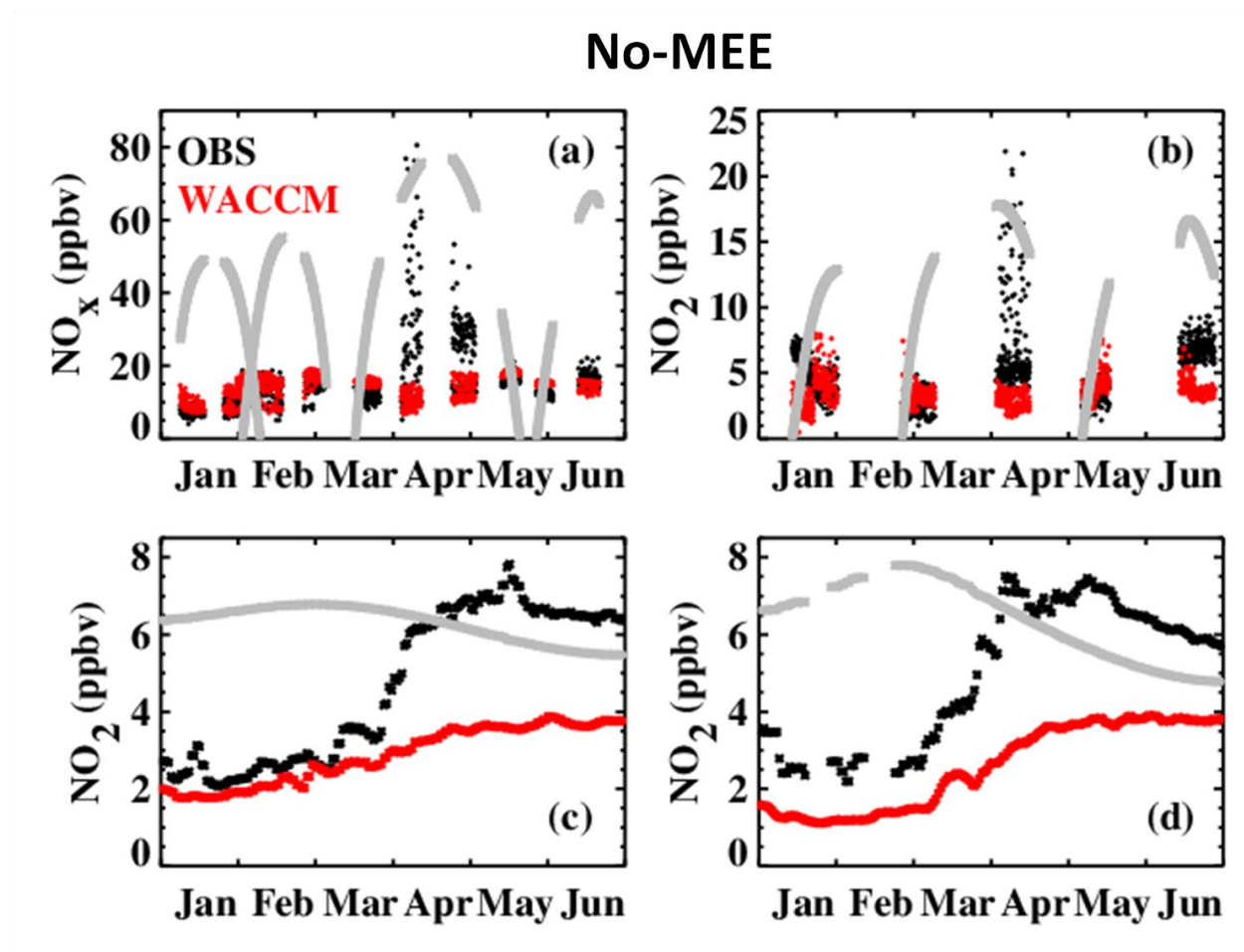
Figure 4.4: Comparisons between SD-WACCM without MEE precipitation (red) and solar occultation measurements (black) in 2004 at 40 km. All NO_x measurements from HALOE are shown in panel (a). All NO_2 measurements from SAGE II are shown in panel (b). Panels (c) and (d) show NO_2 weekly running means for POAM III and SAGE III respectively. Measurement latitudes are given in gray; they are divided by 4 in (b) and by 10 in (c) and (d).
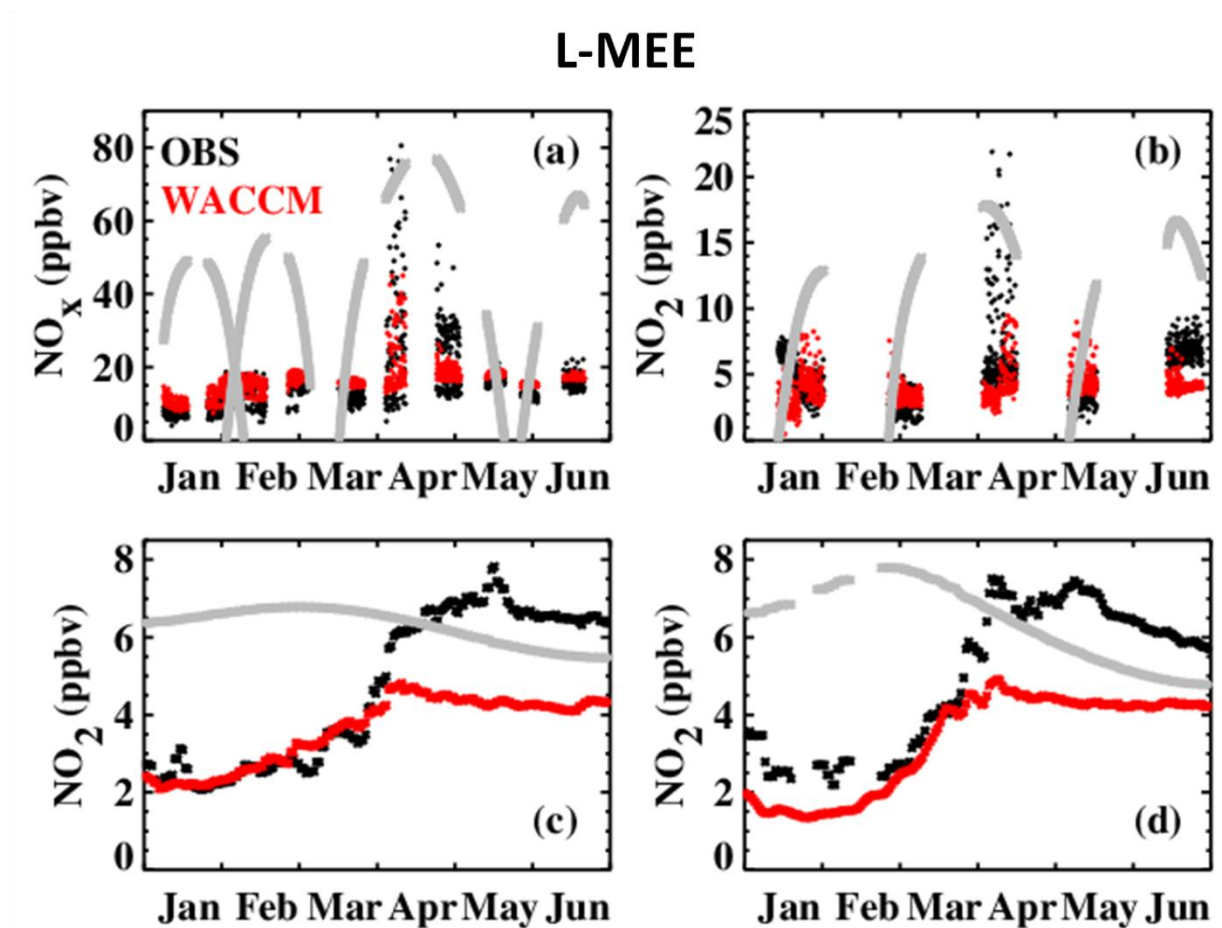
L-MEE

Figure 4.5: Similar to Figure 4.4 but using the L-MEE simulation for SD-WACCM.
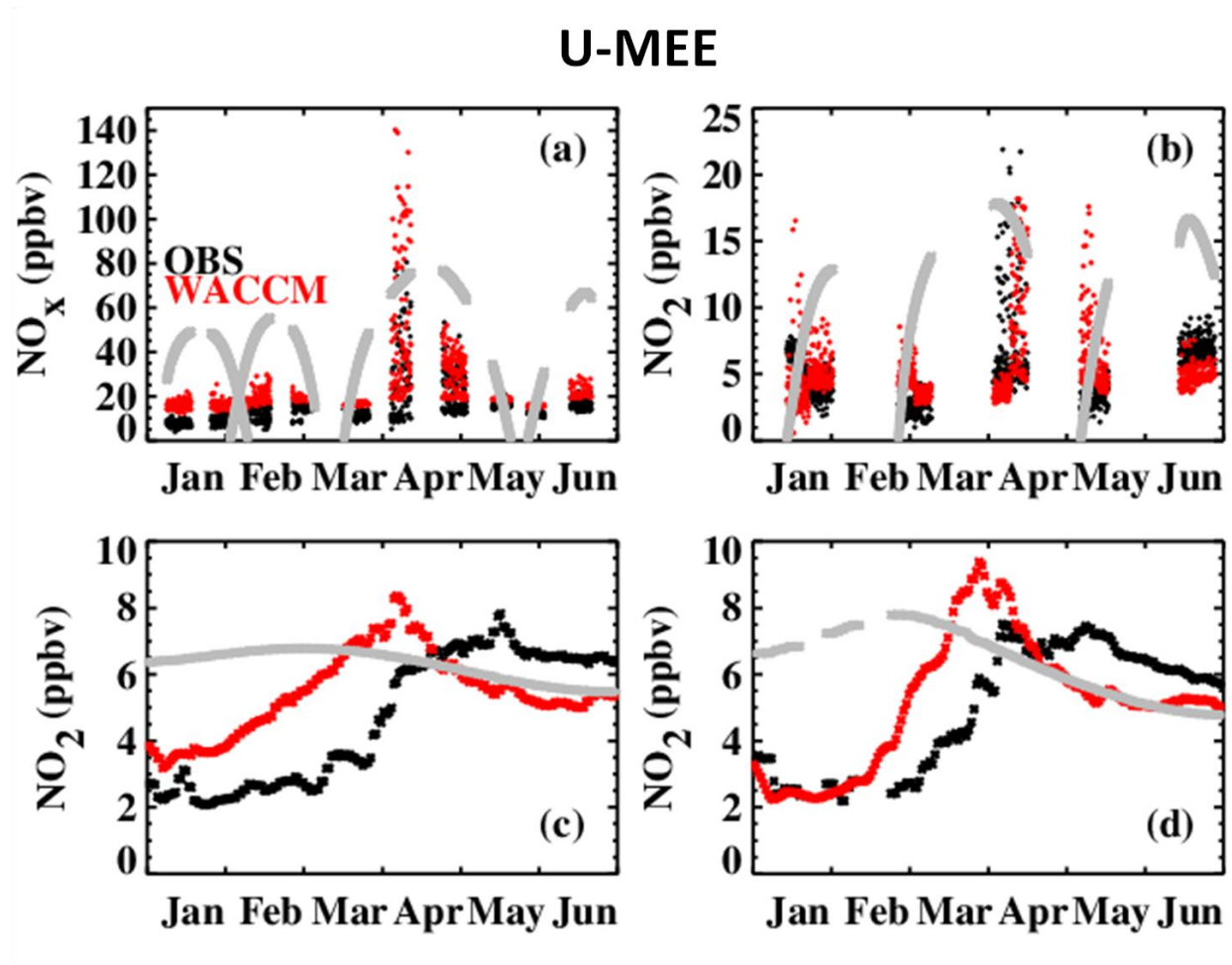
U-MEE

Figure 4.6: Similar to Figure 4.4 but using the U-MEE simulation for SD-WACCM.

much background NO_x below 80km. All three simulations also show too little NO_x above 80 km through March (day 30).

Figure 4.8 is similar to Figure 4.7 but compares the MIPAS observations to the SD-WACCM simulations using MIPAS measurement location 3-day running polar cap averages (>70°N) from November 2003 through March 2004. The NO_x signal can be separated into two distinct descending populations. The first comes from a series of SPEs that occurred over two months beginning with the Halloween Storm in October 2003. The November 2003 time period was analyzed thoroughly by *Funke et al.* [2011]. In that work, WACCM was simulated with both proton and electron ionization rates, as well as with only proton ionization rates. Results showed that WACCM reproduced NO_x associated with the October-November 2003 storms to match observations with MIPAS better if electron ionization rates were not included. Electron ionization rates caused WACCM to overestimate the total NO_x production during the SPEs. Thus it is no surprise that with MEE included in the L-MEE and U-MEE cases, too much NO_x is seen. The second NO_x population comes from the EPP-IE during January, 2004 through March, 2004. MIPAS shows NO_x mixing ratios of 256 ppbv reaching 43 km by the end of March, while the No-MEE simulation has less than 12 ppbv. A slight improvement is seen in the L-MEE case with a value of 32 ppbv. The U-MEE case comes closer with just under 128 ppbv. As supported by Figure 4.7, neither of the MEE cases shows enough NO_x descent from the EPP-IE; meanwhile all other times show too much NO_x from MEE precipitation.

The A_p geomagnetic index, NO_x mixing ratios, and CO mixing ratios are seen in Figure 4.9 for October 2003 through March 2004 between 60 and 120 km for all the simulation cases. There is little change between CO contours in all four simulations, suggesting similar descent rates in all cases. The three MEE cases show more NO_x in the mesosphere than the No-MEE
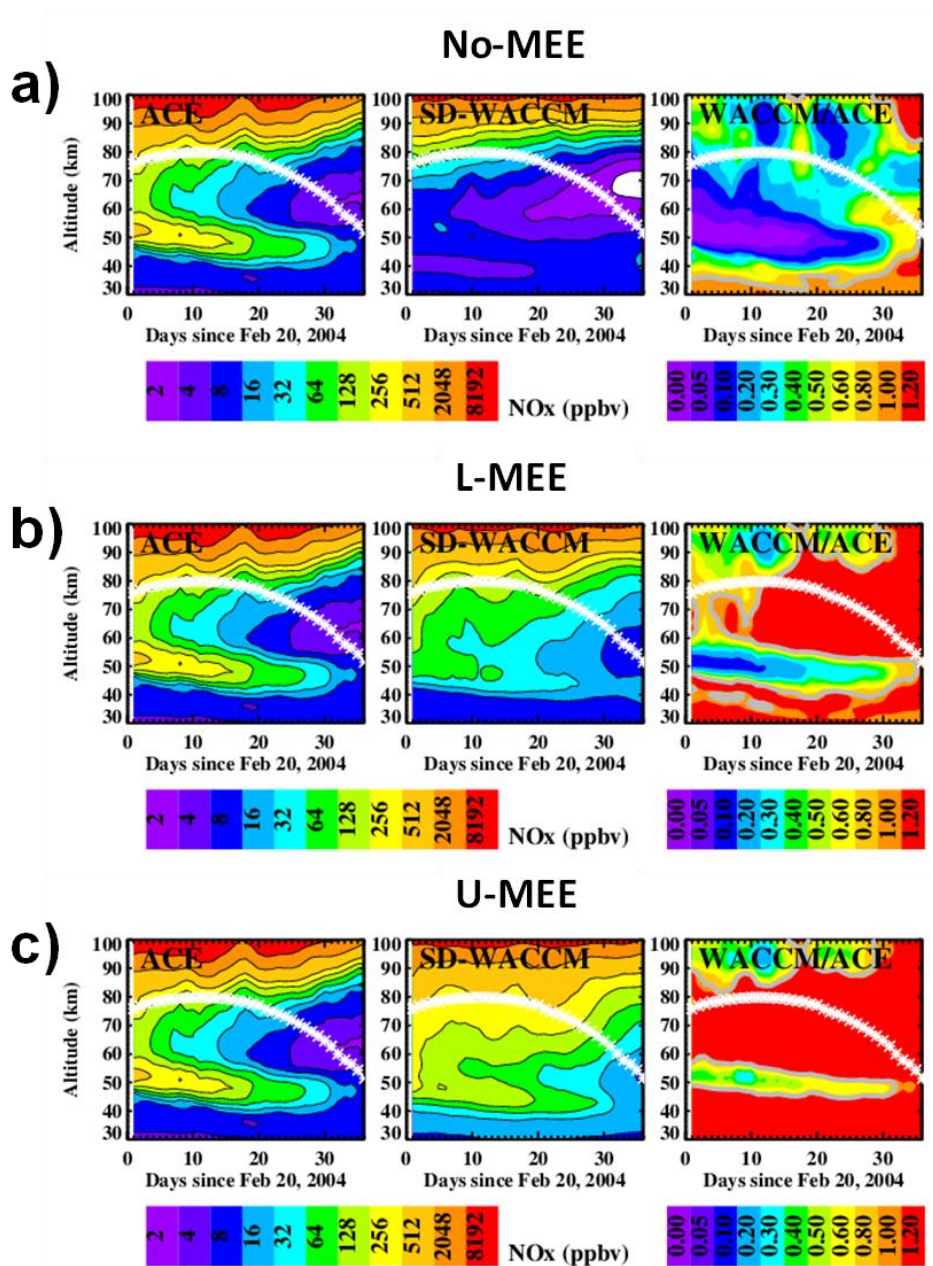
Figure 4.7: Comparisons of ACE (left) and SD-WACCM (middle) NO$_x$ profiles in 2004 with ratios (WACCM/ACE) presented in the right panel. Simulations shown are (a) No-MEE, (b) L-MEE, and (c) U-MEE. Plotted data are 3-day running averages. Latitudes are marked by white symbols. A value of 1.0 in the ratio plots (right) is marked by a grey contour.
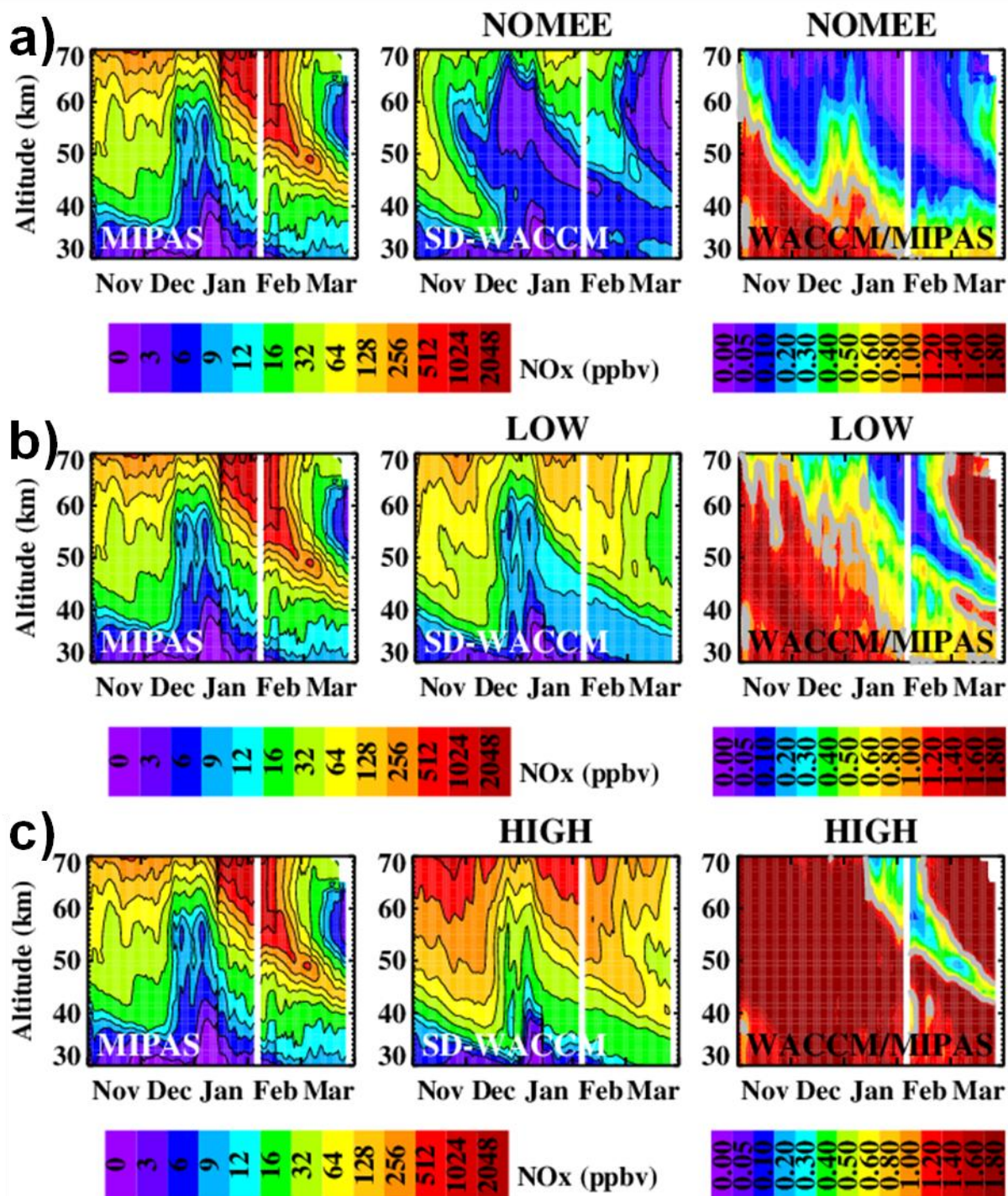
Figure 4.8: Similar to Figure 4.7 but using MIPAS instead of ACE-FTS from November 2003 through March 2004. Plotted data are 3-day running averages of all values poleward of 70°N. White regions represent missing MIPAS data.
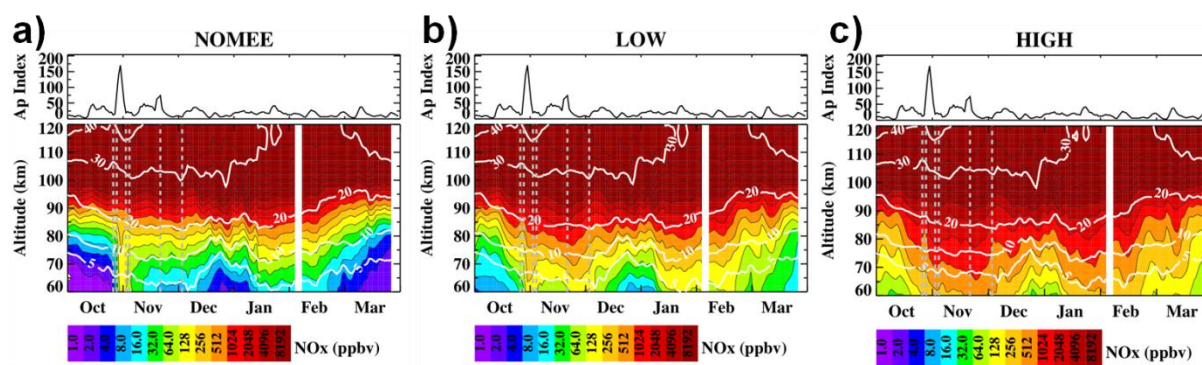
Figure 4.9: Top panels for each plot are 3-day running averages of the Ap index from 1 October 2003 through March 2004. Bottom panels are contour plots of (a) No-MEE, (b) L-MEE, and (c) U-MEE NO_x, with white CO contours at 5, 10, 20, 30, and 40 ppmv. Black NO_x contours above 8192 ppbv continue to increase by factors of 2. NO_x and CO are shown as 3-day running averages over the MIPAS measurement locations poleward of 70°N. White areas indicate missing MIPAS data. Gray, dashed lines indicate SPEs.

case, which is expected given that MEE-NO_x production occurs in the mesosphere. This gives an increased background of mesospheric NO_x in the three MEE cases, as also seen in Figures 4 and 5. At the beginning of October, 2003 the NO_x mixing ratio at 70 km is about 2 ppbv. The L-MEE and U-MEE cases have NO_x mixing ratios of about 32 ppbv and 256 ppbv respectively. This means a factor of 16 and 128 NO_x increase in the L-MEE and U-MEE cases respectively. At 80 km, the NO_x mixing ratios at the beginning of October change to about 16 ppbv, 64 ppbv, and 512 ppbv in the No-MEE, L-MEE, and U-MEE cases respectively. This corresponds to an increase in NO_x by a factor of 4 and 32 in L-MEE and U-MEE respectively compared to the No-MEE case. The pattern of decreasing changes in NO_x with increasing altitude between simulations occurs since MEE-NO_x production drops off in the thermosphere. The No-MEE case should have too little NO_x, though limited observations make it difficult to discern how lacking the NO_x mixing ratios actually are in the mesosphere.

Using a method first described by *Siskind and Russell III* [1996], we calculate total NO_x descent into the lower mesosphere and stratosphere. The original technique has been modified for use in WACCM as described in *Holt et al.* [2012]. The method identifies EPP-NO_x using an anticorrelation between NO_x and CH_4. Once the EPP-NOx is determined, the flux of that NO_x through a given level by a certain date is calculated. In order to avoid counting NO_x created by the October and November 2003 SPEs, we sum total EPP-NO_x descent from 1 February 2004 through 30 April 2004. This time period captures all NOx descent that occurs following a major SSW that lasted through late January 2004.

The total amount of NO_x descent differs greatly depending on the amount of MEE precipitation. Since the descent rates between the three simulations are similar, we assume that all changes in total NO_x descent comes from MEE induced NO_x production. At 0.42 hPa a total

of 0.114, 0.658, and 2.480 Gmol of EPP-NOx was found in the No-MEE, L-MEE, and U-MEE cases respectively. At 1.16 hPa a total of 0.007, 0.486, and 2.090 Gmol was found in the No-MEE, L-MEE, and U-MEE cases. The results from the No-MEE case are in agreement with the results presented by *Holt et al.* [2013], which also used WACCM and did not include MEE precipitation. *Randall et al.* [2007] studied EPP-NO_x descent in the Southern Hemisphere using HALOE measurements and found average values around 0.5 Gmol descent of NOx at 45 km from 1992-2005. The maximum EPP-NO_x descent was 2.6 Gmol in 2003. At 45 km, the EPP-NOx descent in the NH was about zero, 0.306, and 1.543 Gmol in the No-MEE, L-MEE, and U-MEE simulations respectively for the 2003-2004 winter. Therefore, the No-MEE and L-MEE NH simulated EPP-NOx descent is still less than what is usually observed by HALOE in the SH.

4.5 Discussion

Possible reasons for low NO_x in the No-MEE simulation were discussed by *Randall et al.* [submitted, 2014]. Their conclusions were that SD-WACCM exhibited too little production of NO_x in the middle to upper atmosphere, and/or too little downward transport of EPP-NO_x into the stratosphere from the mesosphere and lower thermosphere. In this study a new source of NO_x produced from MEE precipitation is included in the model with two cases, an upper and lower boundary. As seen in Figures 7 and 8, all cases fail to match observations in total NO_x reaching the stratosphere by the EPP-IE. Thus it is clear that regardless of additions to mesospheric NO_x by MEE precipitation, the proper NO_x signal cannot be resolved by SD-WACCM as currently configured. Figure 4.9 showed little change in the CO mixing ratios, indicating that descent rates between the different model cases are all similar. Thus it follows that increased NO_x production did not fix SD-WACCM discrepancies with observations, and descent rates in the mesosphere of

SD-WACCM are too small during the NH winter in 2004; this may be true for other times as well.

Figure 4.9 showed a dramatic increase in NO_x production in the mesosphere by MEE precipitation compared to the No-MEE case that matches ion-pair production from Figure 4.3. The total calculation of EPP-NOx descent reveals that without MEE no NOx descends to 45 km, and with MEE as much as 1.543 Gmol of NOx can reach 45 km. Since the SH regularly sees NOx descent close to 0.5 Gmol [*Randall et al.*, 2007], the model calculated NOx descent suggests MEE is necessary to get realistic results. Likewise, background MEE-NO_x is too high below 80 km and too low above 80 km (Figure 4.7). Ideally NO_x production above 80 km needs to be increased and below 80 km needs to be decreased, and descent rates need to be increased in the mesosphere (at least during the NH winter). If descent rates are increased and MEE production of NO_x stays the same, then even larger background values of NO_x could be expected. MEE precipitation driven NO_x production would needs to decrease and/or be shifted to higher altitudes. The L-MEE case is believed to be an underestimate of MEE production since the POES MEPED 0° detector only measures the lower end of BLC electrons. Since ion-pair production depth is derived from particle energy [e.g., *Fang et al.* 2008; 2010; *Roble and Ridley,* 1987], ion-pair production too low in the atmosphere suggests the energy flux spectrum for MEE precipitation used puts too much electron flux at high energies (>300 keV). Since the flux spectra from *Peck et al.* [submitted, 2014b] were calculated for the satellite altitude (~850 km), it is possible that not only the particle pitch angle distribution changes closer to the atmosphere (Equation 4.1), but the distribution of particle energies also changes. Such changes could come from atmospheric disturbances that would reach to 120 km, but not 850 km. Ionosphere ion temperatures and ionization rates have been observed to be impacted by major atmospheric

disturbances such as Sudden Stratospheric Warmings (SSWs) [e.g., *Goncharenko et al.*, 2008; 2010a; 2010b; 2012; 2013]. This and other events may also be capable of impacting MEE precipitation rates and should be investigated further. Thus the assumption used to map particles from the satellite to the atmosphere (Equation 4.7) may not be appropriate.

At this time, there is no theory or measurements to provide a better guess on how to model electron fluxes with particle pitch angle and altitude. Using instrumentation alone, a constellation of satellites that measure particle flux spectra (e.g., several differential energy channels), at multiple particle pitch angles, and multiple altitudes would be necessary. For example, multiple satellites at varying altitudes, in sun-synchronous polar orbit, that contain several instruments similar to the Detection of Electro-Magnetic Emissions Transmitted from Earthquake Regions (DEMETER) Instrument for Detecting Particles (IDP) [*Sauvaud et al.*, 2006] so that they could measure spectra from multiple pitch angles, ideally within the BLC, would meet the needed specifications. This or a variation on this would provide enough data with which to generate a theory of particle flux distribution with height, pitch angle, and energy within the BLC assuming no atmospheric disturbances can change electron flux distributions in pitch angle or energy.

4.6 Conclusions

This work presents two MEE flux inputs for SD-WACCM simulations to better understand the possible impacts of MEEs on the middle atmosphere. In order to do this, the following assumptions were made:

1. Electron fluxes are dependent on particle pitch angle, and that can be modeled as a sine function (Equation 4.3).

2. Fluxes from the satellite (~850 km) to the atmosphere (~120 km) will change with altitude only from changes in particle pitch angles caused by changing magnetic field strength (Equation 4.1).

The results of the simulations using the two MEE precipitation inputs show the following:

1. Not enough NO_x reaches the stratosphere from the EPP-IE in SD-WACCM regardless of the magnitude of MEE precipitation flux (e.g., Figures 7 and 8), likely caused by too little mesospheric winter descent in the model.

2. Ion-pair production from MEE precipitation likely occurs too low in the modeled atmosphere, suggesting the assumptions made in this analysis are not accurate. This shows up as too much background NO_x except for the EPP-IE tongue and too little NO_x in the upper mesosphere. Given a lack of theory and data, it is currently not possible to formulate the proper energy flux spectrum of MEE precipitation at the atmosphere.

Future work on this topic can take two routes. The first is to indirectly calculate MEE precipitation ion-pair production by trying to fit model simulations to observations. This should result in new electron flux spectra at the atmosphere that have more weight in lower energies to create more NO_x in the upper mesosphere and less in the lower mesosphere. In order for this method to work, the model descent rates would first need to be validated. The second route is to produce more data and theory about how MEEs precipitate into the atmosphere, followed by using that data to improve upon the model input from this work. This would likely entail satellite instrumentation that measures multiple particle pitch angles within the BLC, at many differential particle energy bins (similar to DEMETER IDP), and at multiple altitudes. The exact specifications of such instrumentation are beyond the scope of this work. From increased instrumentation, better theories on how to model MEE precipitation into the atmosphere can be

made, followed by implementation into a global climate model as is done here. Work into theories of MEE precipitation at ~120 km should also investigate possible impacts from the atmosphere on MEE flux distributions in particle pitch angle and energy.

Chapter 5

Summary and Future Directions

What follows is a summary of the work presented in this thesis and considerations for future study of energetic electron precipitation. At the start of this thesis, three goals were presented.

1. **Understand how solar cycle variation, including energetic electron precipitation (EEP) and solar spectral irradiance (SSI), impact the atmosphere as resolved in WACCM4 and how those impacts compare to previous studies.**

Peck et al. [2014a] examined the impacts of the solar cycle on the stratosphere and mesosphere in WACCM4. This work was presented in Chapter 2 and found the following conclusions:

- WACCM4 has a stronger descending branch of the winter hemisphere residual circulation than WACCM3, resulting in stronger NO_x descent and subsequent O_3 loss associated with the EPP-IE.

- The addition of the QBO in WACCM4 resulted in a change to O_3 morphology, where the O_3 maximum was ~2 km higher than in WACCM3. This effect was accompanied by changes in temperature and zonal wind.

- WACCM4 Antarctic middle atmosphere temperatures are too low, known as the "cold-pole" problem. This problem appears to cause dynamical and chemical discrepancies with reality, such as too low stratospheric O_3 concentrations and an overly persistent polar vortex.

- In solar maximum simulations, WACCM O_3 increases from enhanced SSI at mid to low latitudes and O_3 depletion occurs in polar spring from the EPP-IE in agreement with observations.

- Solar cycle induced middle atmosphere dynamics (temperature and zonal wind) in WACCM4 did not agree well with observations in the SH, but were an improvement in the NH compared to WACCM3. This suggests that the "cold-pole" problem is related to Antarctic discrepancies with observations and reanalyses.

The results of *Peck et al.* [2014a] suggest that WACCM4 is capable of simulating the influences of the solar cycle and are in general agreement with observations and reanalysis studies. The only concern is temperature and zonal wind changes in the SH during solar maximum. Therefore, when using WACCM4, it is more appropriate to use specified dynamics to properly simulate middle atmosphere temperatures and winds when trying to examine impacts from the solar cycle.

2. Improve and prepare the POES SEM-2 MEPED data for use in WACCM4.

In order to study the impacts of MEE in WACCM4, it was first necessary to prepare a trustworthy source of MEE precipitation data. *Peck et al.* [2014b] (Chapter 3) presented a new correction method for the POES SEM-2 MEPED MEE data by removing proton contamination from the electron instrument channels. The results of this work were as follows:

- A new dataset was produced where proton contamination was removed from the electron channels. A virtual relativistic electron channel (E4) was added. Proton and electron spectral count fluxes (25 keV − 10 MeV) were created for all POES SEM-2 MEPED measurements.

- Errors from assuming spectral distributions used in the new data product were calculated, permitting an assessment of the best fit method used for each measurement.

- MEE populations are enhanced following SPEs and these signals were not caused by contamination. This suggests that MEE precipitation can have large impacts during solar active periods on middle atmosphere HO_x and NO_x.

- Calculated MEE spectral flux is in agreement with DEMETER IDP.

These results suggest that MEE precipitation is not negligible and should be examined further. This work also provided a fix to proton contamination in the electron channels, with the exception of high energy protons such as those seen in a SPE. This work did not only provide the data necessary to model MEE precipitation in WACCM4, but it also provided a MEE dataset usable by the entire scientific community to study space weather impacts on the atmosphere and magnetosphere.

3. Incorporate MEE into WACCM4 and quantify the modeled impacts on the stratosphere and mesosphere.

In Chapter 4 (*Peck et al.*, 2014, manuscript in preparation), the corrected MEPED electron spectral flux data from *Peck et al.* [2014b] were converted into hemispheric maps and assimilated into SD-WACCM in the form of a sensitivity case study for 2003-2004. Three simulations were created: a control simulation where no MEE precipitation was included, a lower boundary MEE precipitation case, and an upper boundary MEE precipitation case. The results of this study were:

- Not enough NO_x descent associated with the EPP-IE occurred in the simulated NH 2003-2004 winter regardless of MEE precipitation amounts. This suggests an issue with NH winter mesospheric descent in SD-WACCM.

- Below 80 km, too much NO_x production from MEE is occurring in both the upper and lower boundary cases, resulting in greater background levels of NO_x compared to observations.

- Above 80 km, too little NO_x production is occurring in all SD-WACCM simulations, resulting in smaller background levels of NO_x compared to observations.

- Spectral flux calculations in *Peck et al.* [2014b] were made at the satellite altitude (~850 km) and may not be valid at the atmosphere (~120 km). Previous conclusions suggest that a spectral flux that puts more MEE precipitation at lower energies and less at higher energies would solve problems related to MEE induced NO_x production altitudes.

- MEE induced NO_x production can be large in the mesosphere (>100 ppbv) and ion-pair production rates from MEE precipitation can reach >1000 $cm^{-2}s^{-1}$ around 90 km (comparable to a SPE ion-pair production of >5000 $cm^{-2}s^{-1}$ around 60 km).

These results reveal two major conclusions. The first is that MEE precipitation can have a profound impact on the atmosphere and must be better quantified. The second is that the spectral distribution of MEE flux must change at altitudes closer to the Earth. Current theory shows that electron flux should vary only with magnetic field strength. Since too much MEE induced NO_x production was occurring too low in the atmosphere and not enough NO_x production occurred at higher altitudes, the spectral flux of precipitating MEE must have shifted more toward lower energies from higher energies. This is not currently supported by any theory. There are no observations to prove or disprove this possibility.

The three goals, and three studies to achieve those goals, were designed to answer the following question:

What are the impacts of MEE precipitation on the stratosphere and mesosphere?

This work has shown that MEE precipitation can greatly increase NO_x concentrations in the mesosphere and stratosphere. The exact amount of NO_x is difficult to determine given issues of mesospheric descent rates in SD-WACCM. It is possible that the inclusion of improved MEE spectral flux with properly modeled descent rates can explain most or all of the missing middle atmosphere NO_x in models compared to observations. While this thesis has not been able to completely answer the posed question, it has made significant advances in understanding MEE precipitation and is capable of presenting future suggestions for the study of energetic electron precipitation.

Future work in studying MEE precipitation can come in two forms:

1. **Increase observations of precipitating electrons and provide more theory for BLC spectral flux.**

Currently, there are no instruments flying that measure MEE fluxes at multiple pitch angles within the BLC. Without such an instrument, any guess of particle fluxes within the BLC that eventually reach the atmosphere are pure speculation. Ideally, multiple instruments that measure MEE in the BLC at several pitch angles would fly at different altitudes to better understand how those fluxes can change as they approach the Earth. Current theory uses only basic principles to state how particle pitch angle can change with magnetic field strength; however, no work exists that studies how this can differ when approaching the complex Earth system. Just as tropospheric planetary waves can fuel a SSW in the stratosphere, so too can waves propagate from the atmosphere to impact the thermosphere and ionosphere. Such unknown diabatic sources could impact MEE precipitation fluxes that are not included in current adiabatic assumptions.

2. **Improve model descent rates and calculate MEE spectral flux using a backward model.**

If MEE is assumed to be the only major missing source for NO_x production in the mesosphere and thermosphere, then it is possible to calculate the MEE precipitation spectral flux needed to produce that source. This method would require correct descent rates to properly calculate how much NO_x production is needed. The downfall to this method is that it precludes any other potential NO_x source and could result in missing another valid source of NO_x. That said, if the goal is to properly simulate the atmosphere and not study EPP itself, this path would simulate a chemically correct middle atmosphere. This path is not recommended since it essentially parameterizes NO_x production in the mesosphere and lower thermosphere, but may be more feasible for completion in the near future.

Bibliography

Andersson, M. E., P. T. Verronen, S. Wang, C. J. Rodger, M. A. Clilverd, and B. R. Carson (2012), Precipitating radiation belt electrons and enhancements of mesospheric hydroxyl during 2004–2009, *J. Geophys. Res. Atmos.*, *117*(D9), doi:10.1029/2011JD017246

Andersson, M. E., P. T. Verronen, C. J. Rodger, M. A. Clilverd, and S. Wang (2014), Longitudinal hotspots in the mesospheric OH variations due to energetic electron precipitation, *Atmos. Chem. Phys.*, *14*, 1095-1105.

Andrews, D. G., J. R. Holton, and C. B. Leovy (1987), *Middle Atmosphere Dynamics*, Academic Press, San Diego, California.

Asikainen, T., and K. Mursula (2011), Recalibration of the long-term NOAA/MEPED energetic proton measurements, *J. Atmos. Sol. Terr. Phys.*, *73*, 335-347, doi:10.1016/j.jastp.2009.12.011.

Asikainen, T., K. Mursula, and V. Maliniemi (2012), Correction of detector noise and recalibration of NOAA/MEPED energetic proton fluxes, *J. Geophys. Res.*, *117*, A09204, doi:10.1029/2012JA01593.

Asikainen, T., and K. Mursula (2013), Correcting the NOAA/MEPED energetic electron fluxes for detector efficiency and proton contamination, *J. Geophys. Res. Space Physics*, *118*, 6500–6510, doi:10.1002/jgra.50584.

Baker, D. N., J. B. Blake, D. J. Gorney, P. R. Higbie, R. W. Klebesadel, and J. H. King (1987), Highly relativistic magnetospheric electrons: A role in coupling to the middle atmosphere, *Geophys. Res. Lett.*, *14*, 1027.

Baldwin, M. P. and T. J. Dunkerton (2001), Stratospheric harbingers of anomalous weather regimes, *Science*, 294, 581–584, doi:10.1126/science.1063315.

Banks, P. M., and G. Kockarts (1973), *Aeronomy*, 355 pp., Academic Press.

Baumgaertner, A. J. G., A. Seppälä, P. Jockel, and M. A. Clilverd (2011), Geomagnetic activity related NOx enhancements and polar surface air temperature variability in a chemistry climate model: modulation of the NAM index, *Atmos. Chem. Phys.,11*, 4521-4531.

Barnet, J. J., and M. Corney (1985), Middle atmosphere reference model derived from satellite data, *Handbook for MAP, 16: Atmospheric structure and its variation in the region 20-*

120 km: Draft of a new reference middle atmosphere, 47-85.

Barth, C. A., D. N. Baker, K. D. Mankoff, and S. M. Bailey (2001), The northern auroral region as observed in nitric oxide, *Geophys. Res. Lett.*, *28*(8), 1463-1466.

Barth, C. A., K. D. Mankoff, S. M. Bailey, and S. C. Solomon (2003), Global observations of nitric oxide in the thermosphere, *J. Geophys. Res.*, *108*(A1), 1027, doi:10.1029/2002JA009458.

Bates, D. R., and P. B. Hays (1967), Atmospheric nitrous oxide, *Planetary and Space Science*, *15*, 189-197.

Becker, E. and G. Schmitz (2003), Climatological effects of orography and land-sea heating contrasts on the gravity wave-driven circulation of the mesosphere, *J. Atmos. Sci.*, *60*, 103–118, doi:10.1175/1520-0469(2003)0600103:CEOOAL>2.0.CO;2.

Benze, S., C. E. Randall, B. Karlsson, V. L. Harvey, M. T. DeLand, G. E. Thomas, and E. P. Shettle (2012), On the onset of polar mesospheric cloud seasons as observed by SBUV, *J. Geophys. Res.*, *117*, D07104, doi:10.1029/2011JD017350.

Bernath, P. F., et al. (2005), Atmospheric Chemistry Experiment (ACE): Mission overview, *Geophys. Res. Lett.*, *32*, L15S01, doi:10.1029/2005GL022386.

Blake, J. B., D. N. Baker, N. Turner, K. W. Ogilvie, and R. P. Lepping (1997), Correlation of changes in the outer-zone relativistic electron population with upstream solar wind and magnetic field measurements, *Geophys. Res. Lett., 24*, 927.

Brakebusch, M., C. E. Randall, D. E. Kinnison, S. Tilmes, M. L. Santee, and G. L. Manney (2013), Evaluation of Whole Atmosphere Community Climate Model simulations of ozone during Arctic winter 2004–2005, *J. Geophys. Res. Atmos.*, 118(6), 2673-2688 , doi:10.1002/jgrd.50226.

Brasseur, G. P., J. J. Orlando, and G. S. Tyndall (1999), Atmospheric Chemistry and Global Change, Oxford University Press, New York, NY, USA.

Brasseur, G. P., and S. Solomon (2005), Aeronomy of the Middle Atmosphere: Chemistry and Physics of the Stratosphere and Mesosphere, 3rd ed., Springer, Dordrecht, Netherlands.

Butler, A. H., D. J. Seidel, S. C. Hardiman, N. Butchart, T. Birner, and A. Match (2014), Defining sudden stratospheric warmings, *Bull. Am. Meteorol. Soc.*, accepted.

Callis, L. B., D. N. Baker, J. B. Blake, J. D. Lambeth, R. E. Boughner, M. Natarajan, R. W. Klebesadel, and D. J. Gorney (1991), Precipitating relativistic electrons: Their long-term effect on stratospheric odd nitrogen levels, *J. Geophys. Res.*, *96*(D2), 2939-2976.

Callis, L., M. Natarajan, D. Evans, and J. Lambeth, (1998a), Solar atmospheric coupling by

electrons (SOLACE) 1. Effects of the May 12, 1997 solar event on the middle atmosphere, *J. Geophys. Res. Atmos.*, *103*(D21),, 28405-28419, doi:10.1029/98JD02408.

Callis, L., M. Natarajan, J. Lambeth, and D. Baker (1998b), Solar atmospheric coupling by electrons (SOLACE) 2. Calculated stratospheric effects of precipitating electrons, 1979-1988, *J. Geophys. Res. Atmos.*, *103*(D21),, 28421-28438, doi:10.1029/98JD02407.

Callis, L., and J. Lambeth (1998), NOy formed by precipitating electron events in 1991 and 1992: Descent into the stratosphere as observed by ISAMS, *Geophys. Res. Lett., 25*, 1875-1878, doi:10.1029/98GL01219.

Callis, L., M. Natarajan, and J. Lambeth (2001), Solar-atmospheric coupling by electrons (SOLACE) 3. Comparisons of simulations and observations, 1979-1997, issues and implications, *J. Geophys. Res. Atmos.*, 106(D7), 7523-7539, doi:10.1029/2000JD900615.

Chandran, A., R. L. Collins, R. R. Garcia, and D. R. Marsh (2011), A case study of an elevated stratopause generated in the Whole Atmosphere Community Climate Model, *Geophys. Res. Lett.*, *38*, L08804, doi:10.1029/2010GL046566.

Chandran, A., R. L. Collins, R. R. Garcia, D. R. Marsh, V. L. Harvey, J. Yue, and L. de la Torre (2013), A climatology of elevated stratopause events in the whole atmosphere community climate model, *J. Geosphys. Res. Atmos.*, *118*, 1234-1246, doi:10.1002/jgrd.50123.

Chapman, S. (1930), A theory of upper-atmosphere ozone, *Memoirs Roy. Met. Soc.*, 111 (26), 103-125.

Charlton, A. J., and L. M. Polvani (2007), A new look at stratospheric sudden warmings. Part I: Climatology and modeling benchmarks. *J. Clim.*, *20*, 449– 469.

Codrescu, M., T. Fuller-Rowell, R. Roble, and D. Evans (1997), Medium energy particle precipitation influences on the mesosphere and lower thermosphere, *J. Geophys. Res. Space Physics, 102*(A9), 19977-19987.

Crutzen, P. J. (1969), Determination of parameters appearing in the "dry" and the "wet" photochemical theories for ozone in the stratosphere, *Tellus*, *21* (3), 368-388, doi:10.1111/j.2153-3490.1969.tb00450.x.

Crutzen, P. J. (1970), The influence of nitrogen oxides on the atmospheric ozone content, *Quart. J. Roy. Meteorol. Soc.*, *96*, 320-325.

Crutzen, P. J. (1971), Ozone production rates in oxygen-hydrogen-nitrogen oxide atmosphere, *J. Geophys. Res., 76*, 7311-7327.

Crutzen, P. J. (1974), A review of upper atmospheric photochemistry, *Canadian Journal of Chemistry*, *52*, 1569-1581.

Crutzen, P. J., I. S. A. Isaksen, and G. C. Reid (1975), Solar proton events: Stratospheric sources of nitric oxide, *Science*, *189*, 457-459.

Crutzen, P. J. (1979), The role of NO and NO2 in the chemistry of the troposphere and stratosphere, *Annual Review of Earth and Planetary Sciences*, *7*, 443-472.

Cunnold, D. M., *et al.*, (1991), Validation of SAGE II NO2 Measurements, *J. Geophys. Res.*, *96*(D7), 12,913-12925.

Damiani, A., M. Storini, M. L. Santee, and S. Wang (2010), Variability of the nighttime OH layer and mesospheric ozone at high latitudes during northern winter: influence of meteorology, *Atmos. Chem. Phys.*, 10, 10291-10303, doi:10.5194/acp-10-10291-2010.

de la Torre, L., R. R. Garcia, D. Barriopedro, and A. Chandran (2012), Climatology and characteristics of stratospheric sudden warmings in the Whole Atmosphere Community Climate Model, *J. Geophys. Res.*, *117*, D04110, doi:10.1029/2011JD016840.

Dickinson, R. E. (1975), Solar variability and the lower atmosphere, *Bull. Am. Meteorol. Soc.*, *56*, 1240–1248, doi:10.1175/1520-0477(1975)056<1240:SVATLA>2.0.CO;2.

Dunkerton, T. (1978), On the mean meridional mass motions of the stratosphere and mesosphere, *Journal of the Atmospheric Sciences*, *35*, 2325.

Eather, R., S. Mende, and R. Judge (1976), Plasma injection at synchronous orbit and spatial and temporal auroral morphology, *J. Geophys. Res. Space Physics, 81*(16), 2805-2834, doi:10.1029/JA081i016p02805.

Ermakov, V. I., G. A. Bazilevskaya, P. E. Pkrevsky, and Y. I. S. Stozhkov (1997), Ion balance eqution in the atmosphere, *J. Geophys. Res., 102*(D19), 23,413-23,419.

Evans, D. S, and M. S. Greer (2000), Polar Orbiting Environmental Satellite Space Environmental Monitor-2: Instrument descriptions and archive data documentation, *Tech. Mem.*, Natl. Atmos. And Oceanic Admin., Space Environ. Cent., Boulder, CO.

Evans, D., H. Garrett, I. Jun, R. Evans, and J. Chow (2008), Long-term observations of the trapped high-energy proton population (L < 4) by the NOAA Polar Orbiting Environmental Satellites (POES), *Adv. Space Res.*, *41*(8), 1261–1268, doi:10.1016/j.asr.2007.11.028.

Fang, X., M. W. Liemohn, J. U. Kozyra, D. S. Evans, A. D. DeJong, and B. A. Emery (2007), Global 30-240 keV proton precipitation in the $17 - 18$ April 2002 geomagnetic storms: 1. Patterns, *J. Geophys. Res.*, *112*, A05301, doi:10.1029/2006JA011867.

Fang, X., C. E. Randall, D. Lummerzheim, S. C. Solomon, M. J. Mills, D. R. Marsh, C. H. Jackman, W. Wang, and G. Lu (2008), Electron impact ionization: A new

parameterization for 100 eV to 1 MeV electrons, *J. Geophys. Res.*, *113*, A09311, doi:10.1029/2008JA013384.

Fang, X., C. E. Randall, D. Lummerzheim, W. Wang, G. Lu, S. C. Solomon, and R. A. Frahm (2010), Parameterization of monoenergetic electron impact ionization, *Geophys. Res. Lett.*, *37*, L22106, doi:10.1029/2010GL045406.

Fang, X., D. Lummerzheim, and C. H. Jackman (2013), Proton impact ionization and a fast calculation method, *J. Geophys. Res. Space Physics*, *118*, 5369-5378, doi:10.1002/jgra.50484.

Fischer, H., et al. (2008), MIPAS: An instrument for atmospheric and climate research, *Atmos. Chem. Phys., 8*, 2151-2188.

Frahm, R. A., J. D. Winningham, J. R. Sharber, R. Link, G. Crowley, E. E. Gains, D. L. Chenette, B. J. Anderson, and T. A. Potemra (1997), The diffuse aurora: A significant source of ionization in the middle atmosphere, *J. Geophys. Res.*, *102*, 28,203.

France, J. A., and V. L. Harvey (2013), A climatology of the stratopause in WACCM and the zonally asymmetric elevated stratopause, *J. Geophys. Res. Atmos.*, *118*, doi:10.1002/jgrd.50218.

Frame, T. H. A. and L. J. Gray (2010), The 11-Yr Solar Cycle in ERA-40 Data: An Update to 2008, *J. Climate*, 23(8), 2213-2222 , doi:10.1175/2009JCLI3150.1.

Frederick, J. E., R. B. Abrams, and P. J. Crutzen (1983), The Delta Band Dissociation of Nitric Oxide: A Potential Mechanism for Coupling Thermospheric Variations to the Mesosphere and Stratosphere, *J. Geophys. Res., 88*(C6), 3829–3835, doi:10.1029/JC088iC06p03829.

Frith, S., R. Stolarski, and P. K. Bhartia (2004), Implications of version 8 TOMS and SBUV data for long-term trend analysis, paper presented at Quadrennial Ozone Symposium, Int. Ozone Comm., Kos, Greece.

Funke, B., M. L_opez-Puertas, S. Gil-L_opez, T. von Clarmann, G. P. Stiller, H. Fischer, and S. Kellmann (2005), Downward transport of upper atmospheric NO_x into the polar stratosphere and lower mesosphere during the Antarctic 2003 and Arctic 2002/2003 winters, *Journal of Geophysical Research*, *110*, D24308, doi:10.1029/2005JD006463.

Funke, B., A. Baumgaertner, M. Calisto, T. Egorova, C. H. Jackman, J. Kieser, A. Krivolutsky, M. López-Puertas, D. R. Marsh, T. Reddmann, E. Rozanov, S.-M. Salmi, M. Sinnhuber, G. P. Stiller, P. T. Verronen, S. Versick, T. von Clarmann, T. Y. Vyushkova, N. Wieters, and J. M. Wissing (2011), Composition changes after the "Halloween" solar proton event: the High-Energy Particle Precipitation in the Atmosphere (HEPPA) model versus MIPAS data intercomparison study, *Atmos. Chem. Phys., 11*(3), 9407-9514 , doi:10.5194/acpd-11-9407-2011.

Garcia, R. R. and S. Solomon (1985), The effect of breaking gravity waves on the dynamics and chemical composition of the mesosphere and lower thermosphere. *J. Geophys. Res.*, 90, 3850-3868.

Garcia, R. R., and S. Solomon (1994), A new numerical model for the middle atmosphere: 2. Ozone and related species, *J. Geophys. Res.*, 99, 12937–12951.

Garcia, R. R., D. R. Marsh, D. E. Kinnison, B. A. Boville, and F. Sassi (2007), Simulation of secular trends in the middle atmosphere, 1950-2003, *J. Geophys. Res. Atmos., 112*(D9), D09301, doi:10.1029/2006JD007485.

Gent, P. R., G. Danabasoglu, L. J. Donner, M. M. Holland, E. C. Hunke, S. R. Jayne, D. M. Lawrence, R. B. Neale, P. J. Rasch, M. Vertenstein, P. H. Worley, Z.-L. Yang, and M. Zhang (2011), The Community Climate System Model Version 4, *J. Climate, 24*, 4973-4991, doi:10.1175/2011JCLI4083.1.

Goncharenko, L.P. and S. Zhang (2008), Ionospheric Signatures of Sudden Stratospheric Warming: Ion Temperature at Middle Latitude, Geophys. Res. Lett, 35, L21103, doi:10.1029/2008GL035684.

Goncharenko, L. P., J. L. Chau, H.-L. Liu, and A. J. Coster (2010a), Unexpected Connections Between the Stratosphere and Ionosphere, Geophys. Res. Lett., 37, L10101, doi:10.1029/2010GL043125.

Goncharenko, L. P., A. J. Coster, J. L. Chau, and C. E. Valladares (2010b), Impact of Sudden Stratospheric Warmings on Equatorial Ionization Anomaly, J. Geophys. Res., 115, A00G07, doi:10.1029/2010JA015400.

Goncharenko, L. P., A. J. Coster, R. A. Plumb, D. I.V. Domeisen (2012), The Potential Role of Stratospheric Ozone in the Stratosphere-Ionosphere Coupling During Stratospheric Warmings, Geophys. Res. Lett., 39, L08101, doi:10.1029/2012GL051261.

Goncharenko, L. P., V. W. Hsu, C. G. M. Brum, S.-R. Zhang, and J. T. Fentzke (2013), Wave signatures in the midlatitude ionosphere during a sudden stratospheric warming of January 2010, J. Geophys. Res., 118, 472–487, 10.1029/2012JA018251.

Gordley, L. L., et al., (1996), Validation of nitric oxide and nitrogen dioxide measurements made by the Halogen Occultation Experiment for UARS platform, *J. Geophys. Res., 101*, 10,241-10,266.

Gray, L. J., S. T. Rumbold, and K. P. Shine, (2009), Stratospheric Temperature and Radiative Forcing Response to 11-Year Solar Cycle Changes in Irradiance and Ozone , *J. Atmos. Sci.*, 66(8), 2402-2417, doi:10.1175/2009JAS2866.1.

Gray, L. J., et al. (2010), Solar Influences on Climate, *Rev, Geophys.*, 48(4), RG4001, doi:10.1029/2009RG000282.

Greenblatt, J. B., et al. (2002), Tracer-based determination of vortex descent in the 1999/2000 Arctic winter, *Journal of Geophysical Research*, *107*(D20), 5843-5853, doi:10.1029/2001JD000937.

Gu, X., Z. Zhao, B. Ni, Y. Shprits, and C. Zhou (2011), Statistical analysis of pitch angle distribution of radiation belt energetic electrons near the geostationary orbit: CRRES observations, *J. Geophys. Res.*, *116*, A01208, doi:10.1029/2010JA016052.

Gumbel, J. and B. Karlsson (2011), Intra- and inter-hemispheric coupling effects on the polar summer mesosphere, *Geophys. Res. Lett.*, *38*, L14804, doi:10.1029/2011GL047968.

Haigh, J. (1994), The role of stratospheric ozone in modulating the solar radiative forcing of climate, *Nature*, 370(6490), 544-546, doi:10.1038/370544a0.

Hansen, F., K. Matthes, and L. J. Gray (2013), Sensitivity of stratospheric dynamics and chemistry to QBO nudging width in the chemistry-climate model WACCM, *J. Geophys. Res. Atmos.*, *118*, 10,464-10,474, doi:10.1002/jgrd.50812.

Hamilton, K., R. J. Wilson, and R. S. Hemler (1999), Middle atmosphere simulated with high vertical and horizontal resolution versions of a GCM: Improvement in the cold pole bias and generation of a QBO-like oscillation in the tropics. *J. Atmos. Sci.*, 56, 3829–3846.

Harvey, V. L., R. B. Pierce, T. D. Fairlie, and M. H. Hitchman (2002), A climatology of stratospheric polar vortices and anticyclones, *J. Geophys. Res.*, 107(D20), 4442, doi:10.1029/2001JD001471.

Hauchecorne, A., J.-L. Bertaux, F. Dalaudier, J. M. Russell III, M. G. Mlynczak, E. Kyrola, and D. Fussen (2007), Large increase of NO_2 in the north polar mesosphere in January-February 2004: Evidence of a dynamical origin from GOMOS/ENVISAT and SABER/TIMED data, *Geophys. Res. Lett., 34*(3), L03810, doi:10.1029/2006GL027628.

Hines, C., (1974), Possible mechanism for production of sun-weather correlations, *J. Atmos. Sci.*, 31(2), 589-591.

Hitchcock, P., and I. R. Simpson (2014), The downward influence of stratospheric sudden warmings, *J. Atmos. Sci.*, *71*, 3856-3876, doi:10.1175/JAS-D-14-0012.1.

Holt, L. A., C. E. Randall, V. L. Harvey, E. E. Remsberg, G. P. Stiller, B. Funke, P. F. Bernath, and K. A. Walker (2012), Atmospheric effects of energetic particle precipitation in the Arctic winter 1978-1979 revisited, *Journal of Geophysical Research*, *117*, D05315, doi:10.1029/2011JD016663.

Holt, L. A., C. E. Randall, E. D. Peck, D. R. Marsh, A. K. Smith, and V. L. Harvey (2013), The influence of major sudden stratospheric warmings and elevated stratopause events on the

effects of energetic particle precipitation in WACCM, *J. Geophys. Res. Atmos.*, *118*, 11,636-11,646, doi:10.1002/2013JD020294.

Holton, J. R. (2004), *An Introduction to Dynamic Meteorology*, 4th ed., Elsevier, New York, New York.

Horne, R. B., M. M. Lam, and J. C. Green (2009), Energetic electron precipitation from the outer radiation belt during geomagnetic storms, *Geophys. Res. Lett.*, *36*, L19104, doi:10.1029/2009GL040236.

Hunt, B. G. (1966), The need for a modified photochemical theory of the ozonesphere, *Journal of the Atmospheric Sciences*, *23*, 88-95.

Hurrell, J. W., J. J. Hack, D. Shea, J. M. Caron, and J. Rosinski (2008), A new sea surface temperature and sea ice boundary dataset for the Community Atmosphere Model, *J. Climate, 21*(19), 5145- 5153, doi:10.1175/2008JCLI2292.1.

Hurrell, J. W., M. M. Holland, P. R. Gent, S. Ghan, J. E. Kay, P. J. Kushner, J.-F. Lamarque, W. G. Large, D. Lawrence, K. Lindsay, W. H. Lipscomb, M. C. Long, N. Mahowald, D. R. Marsh, R. B. Neale, P. Rasch, S. Vavrus, M. Vertenstein, D. Bader, W. D. Collins, J. J. Hack, J. Kiehl, and S. Marshall (2013), The Community Earth System Model: A Framework for Collaborative Research. *Bull. Amer. Meteor. Soc.*, 94, 1339–1360, doi:10.1175/BAMS-D-12-00121.1

International Association of Geomagnetism and Aeronomy, Working Group V-MOD. Participating members, Finlay, C. C., Maus, S., Beggan, C. D., Bondar, T. N., Chambodut, A., Chernova, T. A., Chulliat, A., Golovkov, V. P., Hamilton, B., Hamoudi, M., Holme, R., Hulot, G., Kuang, W., Langlais, B., Lesur, V., Lowes, F. J., Lühr, H., Macmillan, S., Mandea, M., McLean, S., Manoj, C., Menvielle, M., Michaelis, I., Olsen, N., Rauberg, J., Rother, M., Sabaka, T. J., Tangborn, A., Tøffner-Clausen, L., Thébault, E., Thomson, A. W. P., Wardinski, I., Wei, Z. and Zvereva, T. I. (2010), International Geomagnetic Reference Field: the eleventh generation. Geophysical Journal International, 183: 1216–1230. doi: 10.1111/j.1365-246X.2010.04804.x

IPCC (2013), Climate Change 2013: The Physical Science Basis. Contribution of Working Group I to the Fifth Assessment Report of the Intergovernmental Panel on Climate Change. *Cambridge University Press*, Cambridge, United Kingdom and New York, NY, USA.

Jackman, C., J. Frederick, and R. Stolarski (1980), Production of odd nitrogen in the stratosphere and mesosphere: An intercomparison of source strengths, *J. Geophys. Res.*, *85*, 7495–7505.

Jackman, C. H., M. T. DeLand, G. J. Labow, E. L. Fleming, D. K. Weisenstein, M. K. W. Ko, M. Sinnhuber, and J. M. Russell (2005), Neutral atmospheric influences of the solar proton events in October-November 2003, *J. Geophys. Res.*, *110*, A09S27,

doi:10.1029/2004JA010888.

Jackman, C. H., and P. E. Meade (1988), Effect of solar proton events in 1978 and 1979 on the odd nitrogen abundance in the middle atmosphere, *J. Geophys. Res., 93*, 7084-7090.

Jackman, C. H. D. R. Marsh, F. M. Vitt, R. R. Garcia, E. L. Fleming, G. J. Labow, C. E. Randall, M. López-Puertas, B. Funke, T. von Clarmann, and G. P. Stiller (2008), Short and medium-term atmospheric constituent effects of very large solar proton events, *Atmos. Chem. Phys., 8*(3), 765-785.

Jackman, C. H., D. R. Marsh, F. M. Vitt, R. R. Garcia, C. E. Randall, E. L. Fleming, and S. M. Frith (2009), Long-term middle atmospheric influence of very large solar proton events, *J. Geophys. Res.*, 114, D11304, doi:10.1029/2008JD011415.

Jackman, C. H., et al. (2011), Northern hemisphere atmospheric influence of the solar proton events and ground level enhancement in January 2005, *Atmos. Chem. Phys.*, 11, 6153-6166, doi:10.5194/acp-11-6153-2011.

Johnston, H. (1972), Newly recognized vital nitrogen cycle, *Proceedings of the National Academy of Sciences of the United States of America*, *69*(9), 2369-2372.

Johnston, H. S. (1975), Global ozone balance in the natural stratosphere, *Rev. Geophys*, *13*(5), 637-649, doi:10.1029/RG013i005p00637.

Karlsson, B., H. Körnich, and J. Gumbel (2007), Evidence for interhemispheric stratosphere-mesosphere coupling derived from noctilucent cloud properties, *Geophys. Res. Lett.*, *34*, L16806, doi:10.1029/2007GL030282.

Karlsson, B., C. E. Randall, T. G. Shepherd, V. L. Harvey, J. Lumpe, K. Nielsen, S. M. Bailey, M. Hervig, and J. M. Russell (2011), On the seasonal onset of polar mesospheric clouds and the breakdown of the stratospheric polar vortex in the Southern Hemisphere, *J. Geophys. Res.*, *116*, D18107, doi:10.1029/2011JD015989.

Kerzenmacher, T., et al. (2008), Validation of NO2 and NO from the Atmospheric Chemistry Experiment (ACE), *Atmos. Chem. Phys.*, *8*, 5801-5841.

Kinnison, D. E., et al. (2007), Sensitivity of chemical tracers to meteorological parameters in the MOZART-3 chemical transport model, *J. Geophys. Res.,* 112, D20302, doi:10.1029/2006JD007879.

Kodera, K., and Y. Kuroda (2002), Dynamical response to the solar cycle, *J. Geophys. Res.*, 107(D24), 4749, doi:10.1029/2002JD002224.

Kvissel, O., et al. (2011), Mesospheric intrusion and anomalous chemistry during and after a major stratospheric sudden warming, *J. Atmos. Sol.-Terr. Phys.*, *78–79*, 116–124, doi:10.1016/j.jastp.2011.08.015.

Lam, M. M., R. B. Horne, N. P. Meredith, S. A. Glauert, T. Moffat-Griffin, and J. C. Green (2010), Origin of energetic electron precipitation >30 keV into the atmosphere, *J. Geophys. Res.*, *115*, A00F08, doi:10.1029/2009JA014619.

Lean, J. L., G. J. Rottman, H. L. Kle, T. N. Woods, J. R. Hickey, and L. C. Puga (1997), Detection and parameterization of variations in solar mid and near ultraviolet radiation (200 to 400nm), *J. Geophys. Res.*, 102, 29939-29956.

Lean, J., G. Rottman, J. Harder, and G. Kopp (2005), SORCE contributions to new understanding of global change and solar variability, SOLAR PHYSICS, 230(1-2), 27-53, doi:10.1007/s11207-005-1527-2.

Limpasuvan, V., et al. (2011), The roles of planetary and gravity waves during a major stratospheric sudden warming as characterized in WACCM, *J. Atmos. Sol.-Terr. Phys.*, doi:10.1016/j.jastp.2011.03.004.

Lin, S.-J. (2004), A ''vertically-Lagrangian'' finite-volume dynamical core for global atmospheric models, *Mon. Weather Rev.,* 132, 2293–2307.

Lockwood, M., and C. Fröhlich (2007), Recent oppositely directed trends in solar climate forcings and the global mean surface air temperature, *Proc. R. Soc. A*, *463*(2086), 2447–2460.

Maeda, S., T. J. Fuller-Rowell, and D. S. Evans (1989), Zonally averaged dynamical and compositional response of the thermosphere to auroral activity during September 18–24, 1984, *J. Geophys. Res.*, 94, 16,869-16,883.

Manney, G. L. K. Kruger, J. L. Sabutis, S. A. Sena, and S. Pawson (2005), The remarkable 2003-2004 winter and other recent warm winters in the Arctic stratosphere since the late 1990s, *J. Geophys. Res.*, 110, D04107, doi:10.1029/2004JD005367.

Manney, G. L., et al. (2008), The evolution of the stratopause during the 2006 major warming: Satellite data and assimilated meteorological analyses, *J. Geophys. Res.*, *113*, D11115, doi:10.1029/2007JD009097.

Manney, G. L., M. J. Schwartz, K. Kruger, M. L. Santee, S. Pawson, J. N. Lee, W. H. Daffer, R. A. Fuller, N. J. Livesey (2009), Aura Microwave Limb Sounder Observations of Dynamics and Transport During the Record-breaking 2009 Arctic Stratospheric Major Warming, *Geophys. Res. Lett.*, 36, L12815, doi:10.1029/2009GL038586.

Marsh, D. R., R. R. Garcia, D. E. Kinnison, B. A. Boville, F. Sassi, S. C. Solomon, and K. Matthes (2007), Modeling the whole atmosphere response to solar cycle changes in radiative and geomagnetic forcing, *J. Geophys. Res. Atmos., 112*(D23), D23306, doi:10.1029/2006JD008306.

Marsh, D. R., M. J. Mills, D. E. Kinnison, J.-F. Lamarque, N. Calvo, and L. M. Polvani (2013), Climate Change from 1850 to 2005 Simulated in CESM1(WACCM), *J. Climate*, 26(19), 7372-7391, doi:10.1175/JCLI-D-12-00558.1.

Matthes, K., D. R. Marsh, R. R. Garcia, D. E. Kinnison, F. Sassi, and S. Walters (2010), Role of the QBO in modulating the influence of the 11 year solar cycle on the atmosphere using constant forcings , *J. Geophys. Res. Atmos.*, 115, D18110, doi:10.1029/2009JD013020.

Matthes, K., K. Kodera, R. R. Garcia, Y. Kuroda, D. R. Marsh, and K. Labitzke (2013), The importance of time-varying forcing for QBO modulation of the atmospheric 11 year solar cycle signal, *J. Geophys. Res. Atmos.*, 118(10), 4435-4447, doi:10.1002/jgrd.50424.

Matsuno, T. (1971), A dynamical model of the stratospheric sudden warming. *J. Atmos. Sci.*, *28*, 1479-1494.

McDonald, A. J., and M. Smith (2013), A technique to identify vortex air using carbon monoxide observations, *J. Geophys. Res. Atmos.*, *118*, 12,719–12,733, doi:10.1002/2012JD019257.

McElroy, M. B., and J. C. McConnell (1971), Nitrous oxide: A natural source of stratospheric NO, *Journal of Atmospheric Sciences*, *28*(6), 1095-1098.

McElroy, M. B., S. C. Wofsy, J. E. Penner, and J. C. McConnell (1974), Atmospheric ozone: Possible impact of stratospheric aviation, *Journal of the Atmospheric Sciences*, *31*, 287-303.

McElroy, M. B., J. W. Elkins, S. C. Wofsy, and Y. L. Yung (1976), Sources and sinks for atmospheric N_2O, *Reviews of Geophysics and Space Physics*, *14*(2), 143-150.

McLandress, C., and T. G. Shepherd (2009), Impact of Climate Change on Stratospheric Sudden Warmings as Simulated by the Canadian Middle Atmosphere Model. *J. Clim.*, *22*, 5449–5463, doi:10.1175/2009JCLI3069.1.

Merkel, A. W., J. W. Harder, D. R. Marsh, A. K. Smith, J. M. Fontenla, and T. N. Woods (2011), The impact of solar spectral irradiance variability on middle atmospheric ozone, *Geophys. Res. Lett.*, 38, L13802, doi:10.1029/2011GL047561.

Mertens, C. J., M. G. Mlynczak, R. R. Garcia, and R. W. Portmann (1999), A detailed evaluation of the stratospheric heat budget, 1. Radiation transfer, *J. Geophys. Res.*, *104*(D6), 6021-6038.

Millan, R. M., K. B. Yando, J. C. Green, and A. Y. Ukhorskiy (2010), Spatial distribution of relativistic electron precipitation during a radiation belt depletion event, *Geophys. Res. Lett.*, *37*, L20103, doi:10.1029/2010GL044919.

Minschwaner, K., and D. E. Siskind (1993), A new calculation of nitric oxide photolysis in the

stratosphere, mesosphere, and lower thermosphere, *J. Geophys. Res.*, 98, D11, 20401-20412.

Miyoshi, Y., K. Sakaguchi, K. Shiokawa, D. Evans, J. Albert, M. Connors, and V. Jordanova (2008), Precipitation of radiation belt electrons by EMIC waves, observed from ground and space, *Geophys. Res. Lett.*, *35*, L23101, doi:10.1029/2008GL035727.

Mlynczak, M. G., C. J. Mertens, R. R. Garcia, and R. W. Portman (1999), A detailed evaluation of the stratospheric heat budget, 2. Global radiation balance and diabatic circulations, *J. Geophys. Res.*, *104*, 6039-6066.

Nicolet, M. (1971), Aeronomic reactions of hydrogen and ozone, in *Mesospheric Models and Related Experiments*, vol. 25, edited by G. Fiocco, pp. 1-51, Springer, Netherlands.

Nicolet, M. (1972), Aeronomic chemistry of the stratosphere, *Planetary and Space Science*, *20*, 1671-1702.

Nicolet, M. (1975), Stratospheric ozone: An Introduction to its study, *Reviews of Geophysics and Space Physics*, *13*(5), 593-636.

O'Brien, T. P., and S. K. Morley (2011), Documentation of C Inversion Library, from the *IRBEM* library, <irbem.sourceforge.net>.

Orsolini, Y., M. L. Santee, G. L. Manney, and C. E. Randall (2005), An upper stratospheric layer of enhanced HNO3 following exceptional solar storms, *Geophys. Res. Lett.*, *32*(12), L12S01, doi:10.1029/2004/GL021588.

Peck, E. D., C. E. Randall, V. L. Harvey, and D. R. Marsh (2014a), Simulated solar cycle effects on the middle atmosphere: WACCM3 vs. WACCM4, *J. Adv. Model. Earth Syst.*, submitted.

Peck, E. D., C. E. Randall, J. Green, J. Rodriguez, and C. J. Rodger (2014b), POES MEPED differential flux retrievals and electron channel contamination correction, *J. Geophys. Res. Space Physics*, submitted.

Pierce, J. R., and P. J. Adams (2009), Can cosmic rays affect cloud condensation nuclei by altering new particle formation rates?, *Geophys. Res. Lett.*, *36*, L09820, doi:10.1029/2009GL037946.

Pinto, O., Jr., and W. D. Gonzalez, Energetic electron precipitation at the South Atlantic Magnetic Anomaly: a review (1989), J. Atmos. Terr. Phys., 51, 351-365.

Punge, H. J., and M. A. Giorgetta (2008), Net effect of the QBO in a chemistry climate model, Atmos. Chem. Phys., 8, 6505–6525.

Porter, H. S., C. H. Jackman, and A. E. S. Green (1976), Efficiencies for production of atomic nitrogen and oxygen by relativistic proton impact in air, *J. Chem. Phys.*, *65*, 154-167.

Randall, C. E., D. W. Rusch, R. M. Bevilacqua, K. W. Hoppel, and J. D. Lumpe (1998), Polar Ozone and Aerosol Measurement (POAM) II stratospheric NO_2, 1993– 1996, *J. Geophys. Res*., 103, 28,361–28,371.

Randall, C. E., D. E. Siskind, and R. M. Bevilacqua (2001), Stratospheric NO_x enhancements in the southern hemisphere vortex in winter/spring of 2000, *Geophys. Res. Lett*., 28(12), 2385-2388.

Randall, C. E., et al. (2002), Validation of POAM III NO2 measurements, *J. Geophys. Res.*, *197*(D20), 4432, doi:10.1029/2001JD001520.

Randall, C. E., V. L. Harvey, G. L. Manney, Y. Orsolini, M. Codrescu, C. Sioris, S. Brohede, C. S., Haley, L. L. Gordley, J. M. Zawodny, and J. M. Russell (2005), Stratospheric effects of energetic particle precipitation in 2003-2004, *Geophys. Res. Lett.*, *32*(5), L05802, doi:10.1029/2004GL022003.

Randall, C. E., V. L. Harvey, C. S. Singleton, P. F. Bernath, C. D. Boone, and J. U. Kozyra (2006), Enhanced NO_x in 2006 linked to strong upper stratospheric Arctic vortex, *Geophys. Res. Lett*., 33, L18811, doi:10.1029/2006GL027160.

Randall, C. E., V. L. Harvey, C. S. Singleton, S. M. Bailey, P. F. Bernath, M. Codrescu, H. Nakajima, and J. M. Russell III (2007), Energetic particle precipitation effects on the Southern Hemisphere stratosphere in 1992–2005, *J. Geophys. Res*., 112, D08308, doi:10.1029/2006JD007696.

Randall, C. E., V. L. Harvey, D. E. Siskind, J. France, P. F. Bernath, C. D. Boone, and K. A. Walker (2009), NOx descent in the Arctic middle atmosphere in early 2009, *Geophys. Res. Lett.*, *36*(18), L18811, doi:10.1029/2009GL039706.

Randall, C. E., V. L. Harvey, L. A. Holt, D. R. Marsh, D. Kinnison, B. Funke (2014), Simulation of energetic particle precipitation effects during the 2003-2004 Arctic winter, *J. Geophys. Res. Atmos.*, submitted.

Randel, W. J., and F. Wu (2007), A stratospheric ozone profile data set for 1979–2005: Variability, trends, and comparisons with column ozone data, *J. Geophys. Res*., 112, D06313, doi:10.1029/2006JD007339.

Rault, D. F. (2004), Ozone, NO2 and aerosol retrieval from SAGE III limb scatter measurements, in Proc. SPIE 5571, *Remote Sensing of Clouds and the Atmosphere IX*, 205, doi:10.1117/12.564899.

Remsberg, E. E., P. P. Bhatt, and L. E. Deaver (2001), Ozone changes in the lower stratosphere from the Halogen Occultation Experiment for 1991 through 1999, *J. Geophys. Res.*

Atmos., 106(D2), 1639-1653, doi: 10.1029/2000JD900596

Richards, P. G. (2004), On the increases in nitric oxide density at midlatitudes during ionospheric storms, *Journal of Geophysical Research*, *109*, doi:10.1029/2003JA010110.

Rienecker, M. M., M. J. Suarez, R. Gelaro, R. Todling, J. Bacmeister,E. Liu, M. G. Bosilovich, S. D. Schubert, L. Takacs, G.-K. Kim, S. Bloom, J. Chen, D. Collins, A. Conaty, A. da Silva, W. Gu, J. Joiner, R. D. Koster, R. Lucchesi, A. Molod, T. Owens, S. Pawson, P. Pegion, C. R. Redder, R. Reichle, F. R. Robertson, A. G. Ruddick, M. Sienkiewicz, and J. Woollen (2011), MERRA: NASA's Modern-Era Retrospective Analysis for Research and Applications. *J. Climate*, *24*, 3624–3648, doi:10.1175/JCLI-D-11-00015.1.Richter, J. H., F. Sassi, and R. R. Garcia (2010), Toward a Physically Based Gravity Wave Source Parameterization in a General Circulation Model, *J. Atmos. Sci., 67*(1), 136-156, doi:10.1175/2009JAS3112.1.

Rinsland, C. P., C. Boone, R. Nassar, K. Walker, P. Bernath, J. C. McConnell, and L. Chiou (2005), Atmospheric Chemistry Experiment (ACE) Arctic stratospheric measurements of NOx during February and March 2004: Impact of intense solar flares, *Geophys. Res. Lett.*, *32*, L16S05, doi:10.1029/2005GL022425.

Roble, R., and M. Rees (1977), Time-Dependent Studies of aurora – Effects of particle precipitation on dynamic morphology of ionospheric and atmospheric properties, *Planet. Space Sci., 25*(11), 991-1010, doi:10.1016/0032-0633(77)90146-5.

Roble, R. G., and E. C. Ridley (1987), An auroral model for the NCAR thermospheric general circulation model (TGCM), Ann. Geophys., 5A, 369.

Rodger, C. J., M. A. Clilverd, J. C. Green, and M. M. Lam (2010a), Use of POES SEM-2 observations to examine radiation belt dynamics and energetic electron precipitation into the atmosphere, *J. Geophys. Res.*, *115*, A04202, doi:10.1029/2008JA014023.

Rodger, C. J., B. R. Carson, S. A. Cummer, R. J. Gamble, M. A. Clilverd, J.-A. Sauvaud, M. Parrot, J. C. Green, and J.-J. Berthelier (2010b), Contrasting the efficiency of radiation belt losses caused by ducted and non-ducted whistler mode waves from ground-based transmitters, *J. Geophys. Res.*, *115*, A12208, doi:10.1029/2010JA015880.

Rozanov, E., L. Callis, M. Schlesinger, F. Yang, N. Andronova, and V. Zubov (2005), Atmospheric response to NOy source due to energetic electron precipitation, *Geophys. Res. Lett., 32*, L14811, doi:10.1029/ 2005GL023041.

Rusch, D., J. Gerard, S. Solomon, P. Crutzen, and G. Reid (1981), The effect of particle precipitation events on the neutral and ion chemistry of the middle atmosphere -I. Odd nitrogen, *Planet. Space Sci., 29*(7), 767-774, doi:10.1016/0032-0633(81)90048-9.

Russell, J. M. III, L. L. Gordley, J. H. Park, S. R. Drayson, W. D. Hesketh, R. J. Cicerone, A. F. Tuck, J. E. Frederick, J. E. Harries, and P. J. Crutzen (1993), The Halogen Occultation

Experiment, *J. Geophys. Res.*, *98*, 10,777-10,797.

Sandanger, M., F. Søraas, M. Sørbø, K. Aarsnes, K. Oksavik, and D. Evans (2009), Relativistic electron losses related to EMIC waves during CIR and CME storms, *J. Atmos. Sol. Terr. Phys.*, *71*, 1126–1144, doi:10.1016/j.jastp.2008.07.006.

Sandanger, M., L.-K. G. Ødegaard, H. N. Tyssøy, J. Stadsnes, F. Søraas, and K. Oksavik (2014), A new method of recalibrating NOAA MEPED proton measurements, *EGU General Assembly*, Vienna, Austria, April.

Sander, S. P., et al. (2003), Chemical kinetics and photochemical data for use in atmospheric studies, evaluation 14, JPL Publ. 02-25, NASA Jet Propul. Lab., Pasadena, Calif.

Sander, S. P., et al. (2006), Chemical kinetics and photochemical data for use in atmospheric studies, evaluation 15, JPL Publ. 06-2, NASA Jet Propul. Lab., Pasadena, Calif.

Sauvaud, J.-A., T. Moreau, R. Maggiolo, J. Treilhou, C. Jacquey, A. Cros, J. Coutelier, J. Rouzard, E. Penou, and M. Gangloff (2006), High-energy electron detection onboard DEMETER: The IDP spectrometer, description and first results on the inner belt., *PSS*, *54*(5), doi:10.1016/j.pss.2005.10.019.

Sauvaud, J.-A., M. Walt, D. Delcourt, C. Benoist, E. Penou, Y. Chen, and C. T. Russell (2013), Inner radiation belt particle acceleration and energy structuring by drift resonance with ULF waves during geomagnetic storms, J. Geophys. Res. Space Physics, 118, 1723–1736, doi:10.1002/jgra.50125.

Scherhag, R. (1952), Die esplosionsartigen stratosphärenerwärmungen des spätwinters 1951/52, *Berichte des Deutschen Wetterdienstes in der US-Zone*, *6*(38), 51-63.

Schoeberl, M. R., and D. F. Strobel (1978), The zonally averaged circulation of the middle atmosphere, *J. Atmos. Sci.*, *35*, 577-591.

Selesnick, R. S., and J. B. Blake (2000), On the source location of radiation belt relativistic electrons, *J. Geophys. Res.*, *105*(A2), 2,607-2,624.

Semeniuk, K., V. I. Fomichev, J. C. McConnell, C. Fu, S. M. L. Melo, and I. G. Usoskin (2011), Middle atmosphere response to the solar cycle in irradiance and ionizing particle precipitation, *Atmos. Chem. Phys.*, 11, 5045-5077, doi:10.5194/acp-11-5045-2011.

Seppälä, A., P. T. Verronen, E. Kyrölä, S. Hassinen, L. Backman, A. Hauchecorne, J. L. Bertaux, and D. Fussen (2004), Solar proton events of October-November 2003: Ozone depletion in the Northern Hemisphere polar winter as seen by GOMOS/Envisat, *Geophys. Res. Lett.*, *31*, L19107, doi:10.1029/2004GL021042.

Seppälä, A., P. T. Verronen, M. A. Clilverd, C. E. Randall, J. Tamminen, V. Sofieva, L. Backman, and E. Kyrölä (2007), Arctic and Antarctic polar winter NO_x and energetic

particle precipitation in 2002–2006, *Geophys. Res. Lett.*, 34, L12810, doi:10.1029/2007GL029733.

Seppälä, A., C. E. Randall, M. A. Clilverd, E. Rozanov, and C. J. Rodger (2009), Geomagnetic activity and polar surface air temperature variability, *J. Geophys. Res.*, *114*, A10312, doi:10.1029/2008JA014029.

Shepherd, T. G. (2000), The middle atmosphere, *J. Atmos. Sol-Terr. Phys.*, *62*, 1587-1601.

Shine, K. (1987), The middle atmosphere in the absence of dynamic heat fluxes, *Quart. J. Roy., 113*(476), 603-633 , doi:10.1256/smsqj.47609.

Sinnhuber, M., H. Nieder, and N. Wieters (2012), Energetic particle precipitation and the chemistry of the mesosphere/lower thermosphere, *Surv. Geophys.*, 33, 1281-1334, doi:10.1007/s10712-012-9201-3.

Siskind, D. E., C. A. Barth, D. S. Evans, and R. G. Roble (1989), The response of thermospheric nitric oxide to an auroral storm 2. Auroral latitudes, *Journal of Geophysical Research*, *94*(A12), 899-911.

Siskind, D. E. (1994), On the radiative coupling between mesospheric and thermospheric nitric oxide, *Journal of Geophysical Research*, *99*(D11), 22,757-22,766.

Siskind, D. E., and J. M. Russell, III (1996), Coupling between middle and upper atmospheric NO: Constraints from HALOE observations, *23*(2), 137-140.

Siskind, D. E., J. T. Bacmeister, M. E. Summers, and J. M. Russell, III (1997), Two dimensional model calculations of nitric oxide transport in the middle atmosphere and comparison with Halogen Occultation Experiment data, *J. Geophys. Res.*, 102 (D3), 3527-3545.

Siskind, D. E., S. D. Eckermann, L. Coy, J. P. McCormack, and C. E. Randall (2007), On recent interannual variability of the Arctic winter mesosphere: Implications for tracer descent, *Geophys. Res. Lett., 34*, L09806, doi:10.1029/2007GL029293.

Smith, A. K., R. R. Garcia, D. R. Marsh, and J. H. Richter (2011), WACCM simulations of the mean circulation and trace species transport in the winter mesosphere, *J. Geophys. Res.*, 116, D20115, doi:10.1029/2011JD016083.

Smith, A. K. (2012), Global dynamics of the MLT, *Surv. Geophys.*, 33, 1177–1230, doi:10.1007/s10712-012-9196-9.

Solomon, S.. D.W. Rusch, J.-C. Gérard, G.C. Reid, and P.J. Crutzen (1981), The effect of particle precipitation events on the neutral and ion chemistry of the middle atmosphere: II. Odd Hydrogen, *Planet. Space Sci.*, 29, 8, 885-592.

Solomon, S., P. J. Crutzen, and R. G. Roble (1982), Photochemical coupling between the thermosphere and the lower atmosphere 1. Odd nitrogen from 50 to 120 km, *Journal of Geophysical Research*, *87*(C9), 7206-7220.

Solomon, S., G. C. Reid, D. W. Rusch, and R. J. Thomas (1983), Mesospheric ozone depletions during the solar proton event of July 13, 1982, II, Comparison between theory and measurements, *Geophys. Res. Lett.*, *10*, 257-260.

Solomon, S. C., and L. Qian (2005), Solar extreme ultraviolet irradiance for general circulation models, *J. Geophys. Res.*, 110, A10306, doi:10.1029/2005JA011160.

Soukharev, B. E., and L. L. Hood (2006), Solar cycle variation of stratospheric ozone: Multiple regression analysis of long-term satellite data sets and comparisons with models, *J. Geophys. Res.*, 111(D20), D20314, doi:10.1029/2006JD007107.

Swinbank, R., and D. A. Ortland (2003), Compilation of wind data for the Upper Atmosphere Research Satellite (UARS) Reference Atmosphere Project, *J. Geophys. Res*., 108, doi:10.1029/2002JD003135.

Thorne, R. M. (1977), Energetic radiation belt electron precipitation : A natural depletion mechanism for stratospheric ozone, *Science*, *21*, 287.

Thorne, R. M. (1980), The importance of energetic particle precipitation on the chemical composition of the middle atmosphere, *Pure Appl. Geophys., 118*, 129-151.

Tinsley, B. A., R. P. Rohrbaugh, M. Hei, and K. V. Beard (2000), Effects of image charges on the scavenging of aerosol particles by cloud droplets and on droplet charging and possible ice nucleation processes, *J. Atmos. Sci.*, *57*, 2118–2134, doi:10.1175/1520-0469(2000)057<2118:EOICOT>2.0.CO;2.

Trepte, C. R., and M. H. Hitchman (1992), Tropical stratospheric circulation deduced from satellite aerosol data, *Nature*, 335, 626-628, doi:10.1038/355626a0.

Tsurutani, B. T., and G. S. Lakhina (1997), Some basic concepts of wave-particle interactions in collisionless plasmas, *Rev. Geophys.*, *35*(4), 491-501, doi:10.1029/97RG02200.

Usoskin, I. G., G. A. Kovaltsov, and I. A. Mironova (2010), Cosmic ray induced ionization model CRAC:CRII: An extension to the upper atmosphere, *J. Geophys. Res., 115*, D10302, doi:10.1029/2009JD013142.

Vampola, A. L. (1998), Outer zone energetic electron environment update, in Conference on the High Energy Radiation Background in Space, 128–136, IEEE Press, Piscataway, N. J.

Verronen, P. T., C. J. Rodger, M. A. Clilverd, and S. Wang (2011), First evidence of mesospheric hydroxyl response to electron precipitation from the radiation belts, *J. Geophys. Res. Atmos.*, *116*, D07307, doi:10.1029/2010JD014965

Vitt, F. M., and C. H. Jackman (1996), A comparison of sources of odd nitrogen production from 1974 through 1993 in the Earth's middle atmosphere as calculated using a two-dimensional model, *J. Geophys. Res., 101*(D3), 6729-6739.

von Clarmann, T., et al. (2009), Retrieval of temperature, H_2O, O_3, HNO_3, CH_4, N_2O, $ClONO_2$ and ClO from MIPAS reduced resolution nominal mode limb emission measurements, *Atmospheric Measurement Techniques*, 2(1), 159-175, doi:10.5194/amt-2-159-2009.

Walt, M. (1994), Introduction to geomagnetically trapped radiation, *Cambridge University Press*, Cambridge.

Watson, R. T., M. A. Geller, R. S. Stolarski, and R. F. Hampson (1986), Present State of Knowledge of the Upper Atmosphere: An Assessment Report; processes that control ozone and other climatically important trace gases, *NASA Reference Publication 1162*, p.20.

Whittaker, I. C., R. J. Gamble, C. J. Rodger, M. A. Clilverd, and J.-A. Sauvaud (2013), Determining the spectra of radiation bel electron losses: Fitting DEMETER IDP observations for typical and storm-times, *J. Geophys. Res.*, doi:10.1002/2013JA019228

Whittaker, I. C., C. J. Rodger, M. A. Clilverd, and J.-A. Sauvaud (2014), The effects and correction of the geometric factor for the POES/MEPED electron flux instrument using a multi-satellite comparison, *J. Geophys. Res. Space Physics*, submitted.

Wissing, J. M., and M.-B. Kallenrode (2009), Atmospheric Ionization Module Osnabruck (AIMOS): A 3-D model to determine atmospheric ionization by energetic charged particles from different populations, *J. Geophys. Res.*, *114*, A06104, doi:10.1029/2008JA013884.

Wofsy, S. C., and M. B. McElroy (1974), HO_x, NO_x, and ClO_x: Their role in atmospheric photochemistry, *Canadian Journal of Chemistry*, *52*, 1582-1591.

Woods, T., and G. Rottman (2002), Solar ultraviolet variability over time periods of aeronomic interest, in Atmospheres in the Solar System: Comparative Aeronomy, *Geophys. Monogr. Ser.*, 130, edited by M. Mendillo, A. Nagy, and J. H. Waite Jr., pp. 221 – 234, AGU, Washington, D. C.

Wüest, M., D. S. Evans, and R. von Steiger (2007), Calibration of particle instruments in space physics, *Rep. SR-007*, Int. Space Sci. Inst., Bern, Switzerland.

Yando, K., R. M. Millan, J. C. Green, and D. S. Evans (2011), A Monte Carlo simulation of the NOAA POES Medium Energy Proton and Electron Detector instrument, *J. Geophys. Res.*, *116*, A10231, doi:10.1029/2011JA016671.

Appendix A

POES MEPED Inversion Method

What follows here is the mathematical inversion method described in *O'Brien* [2011] and modified for use with the POES MEPED data. The goal of the method is to solve Equation 3.1:

$$\vec{y} \approx \vec{\lambda} = \delta t \int_0^\infty \vec{G}(E)\vec{f}(E)dE \tag{3.1}$$

Equation 1 can be discretized towards a numerical solution using the following equations:

$$\vec{y} \approx \vec{\lambda} = \underline{H}\,\vec{f} \tag{A1}$$

$$H_{ij} \approx \delta t G_i(E_j)\Delta E_j \tag{A2}$$

$$f_j = f(E_j) \tag{A3}$$

where $\underline{H}$ is the inversion weighting function with dimensions $N_y \times N_E$ and units of cm^2 sr sec keV, N_E is the number of energy bins, and f_j is the discretized form of $f(E)$ from Equation 1 with units of counts/cm^2/sr/sec/keV. Equation A1 is a classic undertermined, uncontrained, inversion equation. There are N_E unknown variables in $\vec{f}$ and N_y equations, where N_y is less than N_E. The inversion technique that follows adds constraints to Equation A3 by taking a weighted average of possible spectral distributions to minimize the difference between $\vec{y}$ and $\vec{\lambda}$ in Equation A1.

The energy bins used in this inversion method are linearly separated in log space. The calculation of ΔE_j in Equation A2 comes from a trapezoidal integral as follows:

$$\Delta E_j = \begin{cases} (E_{j+1} - E_j)/2 & j = 1 \\ (E_j - E_{j-1})/2 & j = N_E \\ (E_{j+1} - E_{j-1})/2 & \text{otherwise} \end{cases} \tag{A4}$$

A "penalty" function is defined to measure the likelihood of seeing the observed counts, $\vec{y}$,

given the calculated expected counts, $\vec{\lambda}$. In other words, the penalty function is a calculation of how far apart $\vec{y}$ and $\vec{\lambda}$ are from each other including possible measurement errors. Observations and expected counts can differ due to various possible measurement error processes. We use Poisson and calibration errors as the only two possible measurement error processes in this correction method. The probability distribution for Poisson errors and calibration errors (given by a Gaussian distribution), are defined as:

$$p^{(P)}(y|\lambda) = \frac{\lambda^y e^{-\lambda}}{y!} \tag{A5}$$

$$p^{(C)}(y|\lambda) = \frac{\exp[-((\ln y - \ln \lambda)/\delta y)^2/2]}{\sqrt{2\pi}\, y \delta y} \tag{A6}$$

where $p^{(P)}$ is the Poisson probability distribution of y given λ and $p^{(C)}$ is the Calibration probability distribution of y given λ.

The penalty function is defined as the negative natural log of the probability distribution. Terms that are not dependent on λ are grouped together as a general constant. The penalty functions for Equations A5 and A6 are defined as:

$$\ell^{(P)}(\lambda) = -\ln p^{(P)} = \lambda - y\ln(\lambda) + \text{constants} \tag{A7}$$

$$\ell^{(C)}(\lambda) = -\ln p^{(C)} = ((\ln y - \ln \lambda)/\delta y)^2/2 + \text{constants} \tag{A8}$$

where $\ell^{(P)}$ is the Poisson probability distribution penalty function, $\ell^{(C)}$ is the calibration probability distribution penalty function, and δy is the Gaussian relative error, calculated to be 0.4 from bowtie analysis [*Selesnick and Blake*, 2000] for POES MEPED.

The derivatives and second derivatives of equations 8 and 9 with respect to λ will be needed later and are as follows:

$$\frac{d\ell^{(P)}}{d\lambda} = 1 - y/\lambda \tag{A9}$$

$$\frac{d^2\ell^{(P)}}{d\lambda^2} = y/\lambda^2 \tag{A10}$$

$$\frac{d\ell^{(C)}}{d\lambda} = (\ln\lambda - \ln y)/(\delta y)^2/\lambda \tag{A11}$$

$$\frac{d^2\ell^{(P)}}{d\lambda^2} = (1 + \ln y - \ln\lambda)/(\lambda\delta y)^2 \tag{A12}$$

Only one penalty function is used in this work for a given value of y. Therefore we select the larger source of error from either the Poisson counting error, $1/\sqrt{y}$, or the calibration Gaussian relative error, δy:

$$\ell_i = \begin{cases} \ell^{(P)} & y < (\delta y)^{-2} \\ \ell^{(C)} & \text{otherwise} \end{cases} \tag{A13}$$

The summation of the selected penalty function from Equation A13 is a measure of how likely a spectral distribution, $\vec{f}$, is appropriately describing the original channel measurements, $\vec{y}$. Therefore, the goal of this inversion method is to minimize the following equation:

$$\ell(\vec{\lambda}) = \sum_i \ell_i(\lambda_i) \tag{A14}$$

Converting the MEPED measurements into spectral flux is inherently an unconstrained problem. As such this inversion method assumes a set of possible spectra, and then weights them based on their ability to minimize Equation A14. Each spectral distribution are defined by a free parameters, q, and the total number of free parameters in each distribution is defined as N_q, where N_q is less than N_E. This effectively reduces the number of unknowns in the inversion of Equation A1. We use four spectral distributions to constrain our solution: power law (PL), exponential (EE), single relativistic Maxwellian (RM), and double relativistic Maxwellian (DM).

The PL spectrum, $f^{(\text{PL})}$, requires two free parameters to fit (e.g., $N_q = 2$). We will need each spectral distribution along with its derivatives and second derivatives with respect to each free parameter. These equations are described as follows:

$$f^{(\text{PL})}(E) = \exp(q_1 - q_2 \ln E) \tag{A15}$$

$$\frac{\partial f^{(\text{PL})}}{\partial q_1} = f^{(\text{PL})} \tag{A16}$$

$$\frac{\partial f^{(\text{PL})}}{\partial q_2} = -\ln(E)f(E) \tag{A17}$$

$$\frac{\partial^2 f^{(\text{PL})}}{\partial q_1^2} = f^{(\text{PL})} \tag{A18}$$

$$\frac{\partial^2 f^{(\text{PL})}}{\partial q_1 q_2} = -\ln E\, f^{(\text{PL})} = \frac{\partial^2 f^{(\text{PL})}}{\partial q_2 q_1} \tag{A19}$$

$$\frac{\partial^2 f^{(\text{PL})}}{\partial q_2^2} = (\ln E)^2\, f^{(\text{PL})} \tag{A20}$$

EE spectrum is described by the following equations with two free parameters:

$$f^{(\text{EE})}(E) = \exp(q_1 + q_2 E) \tag{A21}$$

$$\frac{\partial f^{(\text{EE})}}{\partial q_1} = f^{(\text{EE})} \tag{A22}$$

$$\frac{\partial f^{(\text{EE})}}{\partial q_2} = E f^{(\text{EE})} \tag{A23}$$

$$\frac{\partial^2 f^{(\text{EE})}}{\partial q_1^2} = f^{(\text{EE})} \tag{A24}$$

$$\frac{\partial^2 f^{(\text{EE})}}{\partial q_1 q_2} = E f^{(\text{EE})} = \frac{\partial^2 f^{(\text{EE})}}{\partial q_2 q_1} \tag{A25}$$

$$\frac{\partial^2 f^{(\text{EE})}}{\partial q_1^2} = E^2 f^{(\text{EE})} \tag{A26}$$

RM spectrum has two free parameters and is described by the following equation, while it has derivatives as described by equations A22-A26 if $f^{(\text{EE})}$ is replaced by $f^{(\text{RM})}$:

$$f^{(\text{RM})}(E) = E(1 + E/E_0/2)\exp(q_1 + q_2 E) \tag{A27}$$

The DM spectrum has four free parameters as described below and has the same derivatives as the RM spectrum along with a straightforward extension of equations A22-A26 for the two additional free parameters:

$$f^{(\text{DM})}(E) = E(1 + E/E_0/2)[\exp(q_1 + q_2 E) + \exp(q_3 + q_4 E)] \tag{A28}$$

In the RM and DM spectra, the constant E_0 is used to represent the particle rest energy, which is equal to 511 keV in electrons and 938 MeV in protons.

The final step is to calculate the fit errors and combine the individual spectra to create a best multiple spectral fit. For a given spectrum, $f^{(k)}(E)$, the best fit is the minimization of $\ell^{(k)}(\vec{\lambda})$ with respect to $\vec{q}^{(k)}$, yielding best fit free parameters, $\hat{q}^{(k)}$. For this case, k can be PL, EE, RM, or DM. The minimization routines require derivatives of $\ell^{(k)}$ with respect to $\vec{q}^{(k)}$, given by:

$$\frac{\partial \ell}{\partial q_m} = \sum_i \frac{\partial \ell_i}{\partial \lambda_i} \sum_j \frac{\partial \lambda_i}{\partial f_j} \frac{\partial f_j}{\partial q_m} = \sum_i \frac{\partial \ell_i}{\partial \lambda_i} \sum_j H_{ij} \frac{\partial f_j}{\partial q_m} \tag{A29}$$

To compute the error bars for a given spectral fit, the second derivative of the penalty function with respect to each free parameter is necessary. This can be represented by a Hessian using each combination of free parameters in the following form:

$$\frac{\partial^2 \ell}{\partial q_m \partial q_{m'}} = \sum_i \frac{\partial^2 \ell_i}{\partial \lambda_i^2} \sum_j H_{ij} \frac{\partial f_j}{\partial q_m} \sum_{j'} H_{ij'} \frac{\partial f_{j'}}{\partial q_{m'}} + \sum_i \frac{\partial \ell_i}{\partial \lambda_i} \sum_j H_{ij} \frac{\partial^2 f_j}{\partial q_m q_{m'}} \tag{A30}$$

We treat the error of the resulting flux as having a log-normal distribution with a standard deviation given by the following expression:

$$\sigma_{\ln f^{(k)}(E)} = \sqrt{\sum_m \sum_{m'} \frac{\partial \ln f^{(k)}}{\partial q_m^{(k)}} \text{cov}(q_m^{(k)}, q_{m'}^{(k)}) \frac{\partial \ln f^{(k)}}{\partial q_{m'}^{(k)}}}$$

$$= \sqrt{\sum_m \sum_{m'} \frac{1}{f^{(k)}} \frac{\partial f^{(k)}}{\partial q_m^{(k)}} \text{cov}(q_m^{(k)}, q_{m'}^{(k)}) \frac{1}{f^{(k)}} \frac{\partial f^{(k)}}{\partial q_{m'}^{(k)}}} \tag{A31}$$

$$\text{cov}\left(q_m^{(k)}, q_{m'}^{(k)}\right) = \left(\cdots \quad \begin{matrix} \vdots \\ \frac{\partial^2 \ell^{(k)}}{\partial q_m \partial q_{m'}} \\ \vdots \end{matrix} \quad \cdots \right)^{-1} \tag{A32}$$

To combine the multiple spectra into a single best fit spectrum we calculate a weighting, w, for each spectrum based on the penalty function, $\ell^{(k)}$, and number of free parameters, N_q:

$$w_k = \frac{\exp(-\ell^{(k)} - N_q^{(k)})}{\sum_k \exp(-\ell^{(k)} - N_q^{(k)})} \tag{A33}$$

Finally, the weighted spectra are summed together to yield the following best-fit combined spectrum, $\hat{f}(E)$, with normalized error, $\delta \ln \hat{f}(E)$:

$$\ln \hat{f}(E) = \langle \ln f^{(\text{combined})}(E) \rangle = \sum_k w_k \ln f^{(k)}(E) \tag{A34}$$

$$\delta \ln \hat{f}(E) = \sqrt{\text{var} \ln f^{(\text{combined})}(E)}$$

$$= \sqrt{\sum_k w_k \left(\sigma_{\ln f^{(k)}(E)}^2 + \ln^2 f^{(k)}(E) \right) - \langle \ln f^{(\text{combined})}(E) \rangle^2} \tag{A35}$$

To convert this into normal space flux and error on that flux the following is applied:

$$\hat{f}(E) = \exp\left(\ln \hat{f}(E) \right) \tag{A36}$$

$$\hat{\sigma}(E) = \hat{f}(E) \cdot \delta \ln \hat{f}(E) \tag{A37}$$

Appendix B

Variable Descriptions

Variable	Units	Description
$\vec{y}$	Counts (#)	Vector of measured counts from POES MEPED with length N_y.
N_y	Channels	Number of energy channels from POES MEPED used in inversion.
$\vec{\lambda}$	Counts (#)	Vector of expected counts calculated by inversion method.
E	keV	Energy
$\vec{G}(E)$	cm^2 sr	Vector of response functions for POES MEPED energy channels at particle energy, E, from Y11 appendix B.
$f(E)$	$\#/cm^2/sr/sec/keV$	Differential particle flux at energy, E.
δt	sec	Integration time of instrument data in use. 16 seconds for this work.
$\underline{\underline{H}}$	cm^2 sr sec keV	Weighting function of inversion with dimensions $N_y \times N_E$
N_E	Bins	Number of energy bins used in discretization.
f_j	$\#/cm^2/sr/sec/keV$	Discretized form of $f(E)$ from equation 1.
$p^{(P)}$	Unitless	Poisson probability distribution of y given λ.
$\ell^{(P)}$	Unitless	Poisson probability distribution penalty function.
$p^{(C)}$	Unitless	Calibration probability distribution of y given λ.
$\ell^{(C)}$	Unitless	Calibration probability distribution penalty function.

δy	Unitless	Gaussian relative error
$\vec{q}$	Unitless	Vector of free parameters for each spectrum of length N_q.
N_q	parameters	Number of free parameters for a given spectrum. This equals 2 for PL, EE, and RM or 4 for DM.
E_0	keV	Particle rest energy: 511 for electrons and 9.38×10^5 for protons.
$\sigma_{\ln f^{(k)}(E)}$	$\ln(\#/cm^2/s/sr/keV)$	Standard error on flux of log-normal distribution spectrum.
w_k	Unitless	Weighting on a given spectrum contribution towards the total combined spectrum.
$\hat{f}(E)$	$\#/cm^2/s/sr/keV$	Combined differential particle count flux.
$\hat{\sigma}(E)$	$\#/cm^2/s/sr/keV$	Standard error on combined differential particle count flux.
$J_D(\alpha)$	$\#/cm^2/s/sr/keV$	Differential Particle Count Flux per pitch angle.
J_F	$\#/cm^2/s/keV$	Differential Particle Count Flux over entire BLC.
L	Unitless	L-Shell value
Λ	Radians	Magnetic Latitude

Appendix C

List of Acronyms

ACE-FTS	Atmospheric Chemistry Experiment Fourier Transform Spectrometer
Ap	Geomagnetic Index
BLC	Bounce Loss Cone
CAM	Community Atmosphere Model
CESM	Community Earth System Model
CO	Carbon Monoxide
CO_2	Carbon Dioxide
DEMETER	Detection of Electro-Magnetic Emissions Transmitted from Earthquake Regions
DLC	Drift Loss Cone
DM	Double Relativistic Maxwellian Function
e^*	Secondary electron from EPP
EE	Exponential Function
ENSO	El Niño Southern Oscillation
EPP	Energetic Particle Precipitation
EPP-DE	EPP Direct Effect
EPP-HO_x	EPP produced odd hydrogen
EPP-IE	EPP Indirect Effect
EPP-NO_x	EPP produced odd nitrogen
ES	Elevated Stratopause
GCR	Galactic Cosmic Ray
H	Atomic Hydrogen
HALOE	Halogen Occultation Experiment
H_2O	Water molecule
H_3O^+	Hydronium ion
HO_x	Odd hyrdogen
IDP	Instrument for Detecting Particles
IGRF	International Geomagnetic Reference Field
IPCC	International Panel on Climate Change
ISAMS	Improved Stratospheric and Mesospheric Sounder
Kp	Geomagnetic Index
LIMS	Limb Infrared Monitor of the Stratosphere
MEE	Medium Energy Electron
MEPED	Medium Energy Proton/Electron Detector

MERRA	Modern-Era Retrospective Analysis for Research and Applications
MIPAS	Michelson Interferometer for Passive Atmospheric Sounding
MLS	Microwave Limb Sounder
MLT	Magnetic Local Time
MOZART	Model for Ozone and Related chemical Tracers
N	Atomic Nitrogen
N_2	Nitrogen Molecule
NAM	Northern Annular Mode
NCAR	National Center for Atmospheric Research
NH	Northern Hemisphere
NO_x	Odd Nitrogen
NO_y	Odd Nitrogen and Reservoir Species
NO	Nitric Oxide
NO_2	Nitrogen Dioxide
O	Atomic Oxygen
O_2	Oxygen Molecule
O_3	Ozone
OH	Hydroxyl radical
PL	Power Law Function
POAM	Polar Ozone and Aerosol Measurment
POES	Polar-orbiting Operational Environmental Satellite
QBO	Quasi-Biennial Oscillation
REP	Relativistic Electron Precipitation
RM	Single Relativistic Maxwellian Function
SAA	South Atlantic Anomaly
SAGE	Stratospheric Aerosol and Gas Experiment
SBUV	Solar Backscatter Ultraviolet
SD-WACCM	Specified Dynamics version of WACCM
SEM	Space Environment Monitor
SH	Southern Hemisphere
SOLACE	SOLar Atmospheric Coupling by Electrons
SPE	Solar Proton Event
SSI	Solar Spectral Irradiance
SSW	Sudden Stratospheric Warming
TED	Total Energy Detector
TMS	Turbulent Mountain Stress
TIME-GCM	Thermosphere-Ionosphere-Mesosphere-Electrodynamic General Circulation Model
WACCM	Whole Atmosphere Community Climate Model